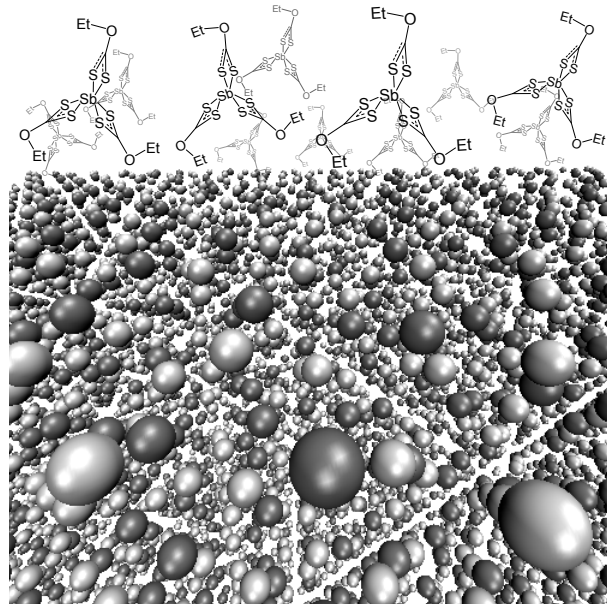


# Electron Transport in Solution Processed Antimony Sulphide Thin Films made from a Xanthate Precursor

Jason Alexander Röhr

September 6, 2014



MRes thesis

Plastic Electronics Doctoral Training Centre  
Department of Physics, Imperial College London

Word count (w/o ref. and front): 33845 (30970) Pages: 83 (74)

# Contents

1	Abstract	4
2	Acknowledgements	5
3	Motivation	6
4	Introduction	8
4.1	Solar cells . . . . .	8
4.2	Solution processed solar cells . . . . .	10
4.2.1	Organic Solar Cells . . . . .	10
4.2.2	Organic/inorganic hybrid solar cells . . . . .	12
4.3	Theory of semiconductors . . . . .	14
4.3.1	Intrinsic semiconductors . . . . .	16
4.3.2	Density of states . . . . .	16
4.3.3	Intrinsic carrier concentrations . . . . .	17
4.3.4	Doped semiconductors . . . . .	18
4.3.5	Ionization of impurities . . . . .	19
4.3.6	Doping dependence on Fermi-levels . . . . .	20
4.4	Metal-semiconductor interfaces . . . . .	21
4.4.1	Metal-intrinsic semiconductor interfaces . . . . .	22
4.4.2	Metal-doped semiconductor interfaces . . . . .	23
4.5	Charge transport in Semiconductors . . . . .	24
4.5.1	Model equations . . . . .	25
4.5.2	Extended and localized states . . . . .	26
4.5.3	Space-charge-limited currents . . . . .	27
5	Experimental procedure	31
5.1	Choice of contact materials . . . . .	31
5.1.1	Tin doped indiumoxide . . . . .	31
5.1.2	Titanium dioxide . . . . .	31
5.1.3	Molybdenum trioxide . . . . .	31
5.1.4	Calcium, Aluminium and Silver . . . . .	32
5.2	Device and sample fabrication . . . . .	32
5.3	Performed measurements . . . . .	36
5.3.1	UV-Vis . . . . .	36
5.3.2	XRD . . . . .	37
5.3.3	SEM . . . . .	38
5.3.4	Space-charge-limited current measurements . . . . .	39
5.3.5	Solar simulation . . . . .	40

6	Results and discussion	41
6.1	Sb <sub>2</sub> S <sub>3</sub> films	41
6.1.1	Crystallinity	41
6.1.2	Material surface coverage	44
6.1.3	Nano- and microstructures of thick films	45
6.2	SCLC modelling results	47
6.2.1	Intrinsic semiconductor	50
6.2.2	Built-in potentials	52
6.2.3	Deep Gaussian traps	55
6.2.4	Shallow exponential traps	57
6.2.5	Doping	58
6.2.6	Thickness dependence	59
6.3	SCLC experimental results	61
6.3.1	Measurements on Sb <sub>2</sub> S <sub>3</sub>	61
6.3.2	Contact choice	62
6.3.3	Numerical fitting	64
6.3.4	Annealing dependence on mobility and doping	66
7	Conclusion	73
8	Outlook and future work	74
	References	75

# 1 Abstract

Space-charge-limited current (SCLC) measurements were realised on thin films of solution processed Antimony sulphide which was deposited from a xanthate precursor decomposed at low temperatures. The electron mobility was determined to be  $4.05 \cdot 10^{-4} \text{ cm}^2/\text{Vs}$ , indicating that this easy processing route yielded poly-crystalline thin films with high mobilities. It is shown that ITO/TiO<sub>2</sub>/CdS and Ca/Al will act as good Ohmic contacts to Antimony sulphide processed by this route. By performing drift-diffusion simulations it is shown that the effect of adding donor type doping to an electron only device has a tendency to increase the current density, making the device act increasingly like a conductor. It was shown that the inclusion of traps had the opposite effect, adding diffusion barriers to oppose charge flow. From this analysis, it is shown by using a numerical solver, that information about the doping concentration can be obtained. The novel approach was used to determine the nature and concentrations of ionized dopants, showing that the solution-processed Antimony sulphide thin film is highly n-type, with a donor concentration of  $2.47 \cdot 10^{17} \text{ cm}^{-3}$ . A novel fitting approach, using the slope of the current density-voltage profile on a log-log scale was used for fitting when the donor concentration was allowed to vary. The charge carrier mobility was allowed to vary to fit to the current density-voltage curves. Hybrid solar cells of P3HT/Sb<sub>2</sub>S<sub>3</sub> is compared to SCLC data obtained for Sb<sub>2</sub>S<sub>3</sub> electron only devices where the annealing time of the inorganic phase was varied from 2 to 10 min in both cases. An increase in the donor concentration was observed from the SCLC measurements of the single carrier devices along with a decrease in the open-circuit voltage in the solar cells, allowing for a way to tune the Fermi level in the semiconductor by simply varying the annealing time.

## 2 Acknowledgements

I would like to thank the following people who have either contributed directly to the project, discussed results with me, discussed theory with me, mentored me, enjoyed my company, talked to me, ignored me, put up with me, and supervised me.

I would like to thank Professor Jenny Nelson for taking me under her wings, for her guidance, and her endless knowledge. I am forever in your debt for everything you have done for me. I am still baffled about being where I am today.

I would like to thank Dr. Saif Haque for his supervision, kindness, discussions and his enthusiasm. Also for never being late for a meeting and for never doubting me. I hope that you will some day realise that my absence from the lab is not due to me skipping work, but merely due to me trying to juggle too many apples.

I would like to thank Professor Thomas Kirchartz for many things, but foremost for his supervision, for his patience, and for everything you have taught me. We are all your students.

I would like to thank my colleagues in the Jenny Nelson group and in the Saif Haque, but specifically Dr. Sachetan Tuladhar who mentored me during my clean room training, Mr. Davide Moia for fruitful discussions and his friendship, Dr Irene Sanchez-Molina for supplying me with precursors, Dr. Thomas Rath for performing the X-ray diffraction measurements, Dr. Michael Brown for his lab expertise and hugs, Miss. Valerie Vaissier for supplying me with the unit cell, and Mr. Andrew MacLachlan for being helpful and a chemist. I would also like to thank Dr. Cecile Charbonneau at Specific for her help with the SEM images.

I would like to thank my DTC cohort, the people who lectured me during the course, and I would like to thank my fellow office students along with the people who used to be here, but moved on to greener fields.

I would finally like to thank my sister, my mom, my dad, my stepmom, my stepdad, my grandmother, my late grandfather, my aunt and uncle, my cousins, our dog, our cats, LeBron James for returning to Cleveland, and my friends here, back home and abroad.

I er min familie. Tak for jeres kærlighed.

### 3 Motivation

With the limited supply of fossil fuels, sky high prices set by the oil countries and the raising concern about global warming, the call for renewable energy sources has never been higher. Solar energy is a promising candidate to alleviate the World's energy budget by using the vast amount of energy coming from the Sun and hitting Earth's surface in the form of light. By using suitable materials, this light can be harvested to generate electricity. Other renewable energy sources exist such as wind, tides and geothermal heat and the application of these technologies where optimal is important in order to mitigate carbon dioxide emissions, to allow countries to be self-sufficient, and to supply power to vast numbers of people currently living off the electrical grid.

The energy from the sun can be harvested in a number of different ways. Many modern houses are built in order to maximize the amount of heat collected from the sun, to minimize the need to burn fossil fuels and to minimize the need for grid electricity. Solar thermal energy can be harvested to drive a turbine in order to generate electricity, and the light particles from the sun can be harvested by solar cells for direct generation of electricity.

A new generation of solar cells is based on the vision of utilizing new cheap materials which are easily processed into solar cells, by either roll to roll processed or other fast, low cost, low temperature and vacuum free manufacturing techniques. A great deal of scientific effort has been put into developing new solution processed organic and inorganic materials in order for this envision to come true. Dye-cells, quantum dot solar cells, all-organic solution processed solar cells and organic/inorganic hybrid cells have all shown promise as a candidate for third generation solar cells, but the benchmarks for commercial realisation are still far from reached, namely high efficiencies and long life times. Recent work from others and within our group has focused on developing solution processed all-inorganic solar cells of materials like Antimony Sulphide and hybrid solar cells from an inorganic semiconductor and a polymer.

When developing new semiconducting materials, which are essential for solar cells, it is important to understand the limiting factors of such materials, so that they can be improved. Expensive processes to manufacture highly crystalline silicon and other semiconductor materials, have proven useful for solar cell manufacturing, yielding high efficiencies. Solution processed materials, even though they are cheap and easy to process, are highly disordered, and carrier mobilities several orders of magnitudes below that observed for perfectly crystalline materials are observed. Furthermore, the imperfectness of the semiconductors also means that a large number of impurities are present in such materials, which can be detrimental for solar harvesting and other semiconducting applications such as transistors and light-emitting diodes. Impurities can trap charges and act as recombination centres, which, if present in large quantities, will be detrimental for solar cell power output. Large charge carrier mobilities are important in electronic components made from semiconducting materials. The extraction yield of generated charges in solar cells is dependent on the mobility of such charges, where a low mobility will result in a higher probability of radiative (as light) or non-radiative recombination (as heat).

In order to correctly diagnose the electrical response of the device, measuring charge transport is important. Many techniques exist to determine charge transport in semiconductors. Solution-processed solar cells are often manufactured by adding consecutive layers of material, giving rise to a sandwich type structure. Mobility measurements techniques such as Hall bars and the mobility measured in Field Effect Transistors measure surface charge carrier mobilities, owing to the nature of the devices used during such measurements. Since the volume mobility is the important parameter in a sandwich type structure, such techniques are not ideal. Furthermore, the processing of the materials might lead to anisotropy of the charge transport, which could influence the measured parameters. For this reason it is important to utilize a technique which is directly comparable with the solar cells.

Space-charge-limited current measurements have for a long time been used to measure charge carrier mobilities in undoped intrinsic semiconductors. It was quickly envisioned that the density and nature of impurities would have a large impact on the outcome of the measurement, and so, it has been proposed that the technique can be used to probe not only the charge transport but the limitation to the charge transport through such impurities. It is however not conventionally used to determine charge transport characteristics in doped semiconductors. Furthermore, space-charge-limited current measurements are most commonly interpreted using simple analytical models which does not include the effect of charge traps nor the effect of doping.

This study will focus on evaluating the electrical transport properties of one of the most promising solution processed inorganic semiconductors for solar cell application, namely Antimony Sulphide. Space-charge-limited current mobility measurements is chosen since the used device structure in such measurements is most easily compared to device structures as those used in solar cells. Structural and optical measurements of the solution processed thin films are presented as the film is prepared in different ways. A theoretical study on how different device features, such as metal-semiconductor injection barriers, dopants and trap states will influence the experimental data, is carried out. Electrical results from space-charge-limited current measurements is presented, and numerical fitting to obtain knowledge on the parameters influencing charge transport is performed. Finally, solar cell device performance is correlated to the experimental findings, and SCLC is critically evaluated as a method for the studied materials.

## 4 Introduction

### 4.1 Solar cells

Solar cells utilize the unique feature of semiconductors which allows for the absorption of light particles coming from the sun in order to generate electricity. Even though many types of solar cells, using a large variety of materials, have been presented in the literature, the operating principle is similar; the energy from light is harvested in order to promote an electron from a filled state to an empty state within the material, which forms a quasi-particle called an exciton. This exciton, which is consisting of a bound pair of an electron in the before empty band and the hole left behind in the before filled band, can then be split into free charge carriers and be transported to their respective electrodes to generate a current. Many different means of exciton dissociation have been proposed from spontaneous dissociation in semiconductors with high dielectric constants, charge separation though interfaces with metals, charge separation through interfaces with another semiconductor with different energy levels, to separation in interfaces of the same material but with different doping profiles.

The photovoltaic effect, which is the generation of a current or voltage in a material when exposed to light, was discovered by Alexandre-Edmond Becquerel in 1839 [1, 2]. However, Willoughby Smith was the first to publicly describe the effect, when he discovered the semi-conducting properties of Selenium [3]. However, it was not until 1954 that the modern solar cell would be invented in Bell Laboratories by Daryl Chapin, Calvin Souther Fuller and Gerald Pearson, which was a silicon p-n junction with an efficiency of roughly 6% [4, 5]. The p-n junction is an interface where intentional doping creates a side which is electron-rich in contact with a hole-rich side. Upon excitation, the exciton is split at the p-n junction and the free charge carriers are transported to their respective contacts by diffusion-assisted transport. All solar cells are, in principle, based on the idea of the first silicon solar cell. Upon absorption of a photon, an exciton is generated by the promotion of an electron from the valence band to the conduction band. The exciton is a bound quasi-particle formed by the promoted electron and the resulting hole which are held together by Coulombic interaction, the magnitude of which is governed by the relative permittivity of the material ( $\epsilon_r$ ). In order for the exciton to be split into free charge carriers, the bound state must be subjected to a driving force strong enough to dissociate the two charge carriers. The electric field arising in the p-n junction interface, is an example of such a driving force. Even though silicon is the most studied material for solar cells it is not the best suited, due to its relatively low band gap (which is also indirect). It is however highly abundant in the Earth's crust, cheap to produce and very well-known due to the massive silicon industry. A material such as Gallium Arsenide has a much better suited band gap than silicon, but the means of processing is expensive, resulting in such solar cells only being used in situations where cost is not an issue, as with satellites. Later technologies for solar cells, such as the organic based solar cells, employs either a donor-acceptor strategy for charge separation, such as the bulk hetero-junction solar cell, or by sensitization of a mesoporous inorganic trans-

port layer by an organic dye absorber [6, 7, 8]. Such solar cells can be processed from solution which offer cheap roll-to-roll fabrication and since the cells are made from organic compounds, the design possibilities of the active compounds are endless. Hybrid solar cells using either a polymer or a small organic molecule in combination with an inorganic acceptor material have shown promise for efficient electricity generation.

When a solar cell is illuminated with an applied voltage, a photocurrent is observed called the short-circuit current ( $I_{sc}$ ). As the bias is swept under illumination, the photocurrent will decrease as the internal field arising from the difference in work functions is opposed by the field arising from the applied bias, until the photocurrent is zero. The applied voltage where the photocurrent is zero is called the open-circuit voltage ( $V_{oc}$ ). These two situations correspond to the cases of a zero load and an infinite load. Since the power provided by a cell is given as the product of the current and the voltage, the power will be zero in both the short-circuit and the open-circuit. In order to increase the power, the voltage must be increased beyond the short-circuit situation until a maximum power point is reached, ( $P_{max}$ ), which will be defined by the maximum voltage,  $V_m$ , and maximum current,  $I_m$ . It is quite clear that in order to achieve a high maximum power output the short-circuit current and the open-circuit voltage must be maximised, and so, these two parameters are often stated in order to define the performance characteristics of a solar cell. Another important parameter is the squareness of the  $I$ - $V$  curve when the voltage is swept under illumination. The squareness defines the response of the current when the voltage is changed, and the maximum power will be highest if the  $I$ - $V$  curve is a perfect square (in which case  $V_m = V_{oc}$  and  $J_m = J_{sc}$ ). That is however not achievable, so in order to define the maximum power output from the two solar cell parameters a quantity called the fill factor (FF) is introduced. The fill factor will be governed by the limiting parameters in the cells such as series resistance and shunts. The most important device parameter of a solar cell is the power conversion efficiency (PCE), which is given by the ratio of the maximum outgoing power ( $P_{max}$ ) produced by the cell and the incoming power from the light source which, in the case of solar cells, is the Sun ( $P_{sun}$ ). The maximum power can be expressed as the product of the maximum voltage ( $V_{max}$ ) and the maximum current ( $I_{max}$ ). As was mentioned above, the maximum current and voltage can be defined from the short-circuit current and the open-circuit voltage through the fill factor (FF), so that the PCE is given as

$$\text{PCE} = \frac{P_{max}}{P_{sun}} = \frac{I_{sc}V_{oc}\text{FF}}{P_{sun}}. \quad (1)$$

From the above equation it is clear that in order to achieve a high power conversion efficiency it is important to have a large current, a high voltage and a good fill factor.

Since charge carriers are generated through absorption of a photon, the current is governed by the band gap of the material. For this reason, the optimal solar cell must be made from a material where the band gap fits nicely with the solar spectrum in order to absorb as many photons as possible. It is important to note that the energy of the photon, once the band gap is surpassed, does not play an important role as the excited electron will quickly relax to the

lowest level in the conduction band through thermal dissipation. So the key is the number of photons (intensity of light) and not the energy of these photons. The maximum obtainable voltage is defined from the driving force coming from the difference in electron affinities of the two electrodes. Since the difference in electron affinities cannot exceed the magnitude of the band gap, the maximum obtainable voltage will be governed by  $V_{oc} = E_g/q$  (given that the semiconductor is not excited to degeneracy). It is very important to point out that in order to absorb a large amount of photons coming from the visible part of the solar spectrum, a low band gap must be used, but since that reduces the highest obtainable voltage, a compromise must be made. The third parameter, the fill factor, is governed by the electrical characteristics of the cell. A high fill factor is obtained if the series resistance is low and the shunt resistance is high, meaning that the material should exhibit a high charge carrier mobility and no leakage currents.

## 4.2 Solution processed solar cells

As was briefly mentioned, the cost of solar cells must be greatly reduced if the technology is to be used on a global scale. Silicon solar cells are relatively expensive due to difficulty of processing. Solution processed semiconductors offer a cheap way to manufacture solar cells on a large scale through roll-to-roll processes.

### 4.2.1 Organic Solar Cells

A large variety of solution processed semiconductors have been developed, but none has achieved the amount of attention in the past three decades as organic semiconductors in the form of small molecules or long chains of conjugated polymers. The discovery of conducting and semiconducting polymers opened up a new field of research combining chemistry and solid state physics, for which Heeger, Shirakawa and MacDiarmid were awarded the Nobel prize in 2000 [9, 10, 11]. Almost endless possibilities of combination of chemical constituents for fine tuning of organic semiconductors to match application, ease of process and solubility exists.

One of the earliest articles reporting photo-physical effects and band like structures in organic systems was published in 1946 by Szent-Györgyi, where coloured protein films showed increased conductivity upon illumination [12]. Following this work it was shown that phthalocyanine and Cu-phthalocyanine were semiconductors, and it was proposed that  $\pi$ -stacking between individual molecules would form a crystal which would give rise to band-like electronic behaviour [13]. The semi-conducting nature of anthracene was later observed [14, 15]. Results for polymers showing n- and p-type behaviour in electrical measurements were subsequently published, where the conjugation length was reported to be paramount for good conduction [16]. It was however not until the famous 1979 paper published by Heeger, MacDiarmid and Shirakawa showing that polymers could be doped to such an extent as to span from being semiconductors

to conductors, that the research field of plastic electronics accelerated.

Semiconducting polymers all have one thing in common; they comprise of alternating single and double bonds, so called conjugation, which will result in overlapping p<sub>z</sub>-orbitals, giving rise to their conductive properties. The overlap between the p<sub>z</sub>-orbitals will give rise to a lower lying orbital, the highest occupied molecular orbital (HOMO) and a higher lying orbital, the lowest unoccupied molecular orbital (LUMO). The difference between the HOMO and the LUMO in conjugated molecules is called the optical gap, or band gap (from inorganic terminology), and at  $T = 0$  and zero illumination all states up to the HOMO level will be occupied with electrons and all states above will be empty. When a film or a solid crystal is formed, the HOMO and LUMO levels can be considered as being similar to valence and conduction bands.

In order to achieve a high efficiency in donor-acceptor type solar cells it is important to have efficient exciton dissociation, which can be achieved by having a large and good interface for charge separation between the two materials, where the material containing the exciton (the donor) has a more shallow LUMO level than the material used as an acceptor. Such an interface (type-II) is called a donor-acceptor heterojunction. The simplest solar cell design when using a donor-acceptor heterojunction is the bilayer design [17], where a flat heterojunction between the donor and acceptor can be achieved, and upon charge dissociation at the interface, the charge carriers can travel to their respective contacts. Such a bilayer structure is however limited by the small exciton diffusion lengths in polymers (approx 10 nm) [18] and so, in order to achieve good charge separation, the thickness of the device must be small, which in turn lowers the absorption (leading to a lower efficiency). An alternative device structure was achieved by blending the donor and acceptor molecules in the same solution, and upon film processing, a bulk heterojunction (BHJ) was obtained with the donor and acceptor molecules forming an inter-penetrating network, allowing for more efficient devices.

Sariciftci et al reported that charge transfer from a polymer to a buckminsterfullerene (C<sub>60</sub>) upon excitation of a photon in the polymer was possible [19, 20], and upon the discovery of a synthetic route to PCBM (solution processable C<sub>60</sub> derivative) [21] the polymer:PCBM BHJ solar cell was reported in 1995 [22]. However polymer:polymer BHJ solar cells were reported earlier the same year [23, 24].

Up until around 2006, most work on organic solar cells was put into optimization of the morphology of P3HT:PCBM blend devices to increase the efficiency [25, 26, 27, 28, 29]. However, a lot of the work in the research field at recent times have also been on developing new materials [30, 31, 32], developing better interlayers and optimizing device architecture [33], and making tandem devices to increase the efficiency [34, 35]. Developing donor and acceptor materials with optimal band gaps, optimal energy levels for charge separation, and proper processing abilities is paramount for the commercial success of organic photovoltaics. High (and balanced) electron and hole mobilities and large exciton diffusion lengths are also important to obtain to ensure that thick devices can be made while still retaining power conversion efficiency, since thin devices which are usually presented in the research community are not compatible with

large scale fabrication.

Heliatek GmbH currently holds the efficiency record for organic small molecule cells with a power conversion efficiency of 10.7% [36]. Mitsubishi currently holds the efficiency record for polymer:fullerene solar cells with a power conversion efficiency of 11.0% [37]. P3HT based solar cells (usually in combination with PCBM) are usually used as model systems since this combination of materials are well known and good efficiencies have been achieved. However, this combination of materials does not yield the most efficient organic solar cell devices seen to date.

#### 4.2.2 Organic/inorganic hybrid solar cells

Even though the majority of research on solution processed semiconductors has gone towards organics, inorganic materials could potentially offer higher mobilities along with more stable device performance. A large number of high efficiency devices have recently been reported by using the perovskite crystal structure [38, 39, 40]. This section on solution processed organic /inorganics hybrid solar cells will however focus on metal chalcogenides, as charge transport in Antimony sulphide is the topic of this study. For that reason, perovskites will not be discussed in this thesis. Many routes for thin film formation of chalcogenides have been reported in the literature. However, thermal evaporation and sputtering require high vacuum conditions and high temperatures, which is not ideal for flexible substrates which will be needed for high throughput fabrication [41], so emphasis will be put on solution processable films of metal chalcogenides. In order to fabricate polymer:inorganic bulk heterojunction solar cells, it is important that both the donor and the acceptor material can be processed from the same solution, that the acceptor is energetically compatible with the donor, and that their respective sizes are small enough in order for a good interpenetrating network to arise. The use of small nanoparticles, or quantum dots, is a promising approach for obtaining good phase separation between an organic donor and an inorganic acceptor, and has been extensively studied [42, 43, 44, 45].

The strengths of employing an inorganic quantum dot acceptor into a donor:acceptor bulk heterojunction lies partly in the high absorption of crystalline inorganic semiconductors. Fullerene derivatives, such as PCBM, absorbs primarily in the blue end of the visible light spectrum due to their large optical gaps. The number of photons available from the Sun at such high energies are limited, and so, it would be more beneficial to use an acceptor with higher absorption in the visible or infrared part of the spectrum. By varying the size of these nanoparticles, the optical gap can be tuned, where a widening of the gap is expected as the particle becomes smaller. Quantum dots have also been proposed as a way to increase the efficiency of solar cells by means of extracting hot carriers or by sensitising a mesoporous semiconductor scaffold [44]. Quantum dots were first discovered in 1981 by Alexey Ekimov [46], where an absorption onset shift due to quantum confinement was reported for CuCl crystals as the dot sizes were decreased. The quantum confinement of colloids were subsequently reported by Rossetti et al [47] and a quantum mechanical model for zero-dimensional quantum confinement in nanoparticles

was published the following year [48]. In general, there are two ways to fabricate a quantum dot, namely the bottom-up technique where nanostructures are formed through self-assembly, and the top-down technique where the structures are defined or cut-out from an already present structure. The fabrication of quantum dots through this bottom-up self-assembly route is of high interest for use in solar cells, as it allows for a blend between an organic semiconductor, such as a small molecule or a polymer, and quantum dots of suitable sizes [49, 50, 51, 52, 53], or all inorganic solar cells [54, 55].

Forming inorganic semiconductors from precursors have been widely reported. Mitzi *et al* reported high mobility thin films of metal chalcogenide films using a hydrazinium precursor solutions [56, 57, 58, 59]. Hydrazine has also been used to fabricate CIGS films from solution [60], leading to highly efficient all-inorganic solar cells. Hydrazine is however a highly toxic compound, and so, using a less toxic solvent is important when fabrication on large scale. Peng and Peng showed in 2001 that CdTe, CdSe and CdS nanoparticles could be synthesised using a one-pot approach, yielding non-toxic sideproducts, by using a CdO precursor in combination with either Te, Se or S powders [61]. However, using the route by Peng and Peng requires high temperatures of 250°C, which is not suitable for the organic phase in organic:inorganic films. A large amount of papers on the topic of in situ grown inorganic films can be found in the literature, but it was not until 2010 that Leventis *et al* reported an *in situ* approach for the formation of nanoparticles within a formed polymer film by using a xanthate precursor giving off non-toxic side products [62]. The approach by Leventis was inspired by the initial studies of forming nanoparticles from xanthates by Nair [63], and Pradhan [64, 65]. The paper by Leventis does however act as a foundation for a low-cost and low-temperature method for forming organic:inorganic films from xanthate precursors.

Organic/inorganic hybrid solar cells have been reported with varied device architectures, structures and consequently efficiencies. Most reports with devices yielding good efficiencies have however employed a bulk heterojunction type device where an intimate mix between the donor and the acceptor material has been used to facilitate charge separation [42, 66, 67, 68].

Xanthates are salts which may form a complex with a metal atom by forming bonds to two Sulphur atoms. Xanthates usually have the formula ROCS<sub>2</sub>M, where R is an organic side-chain (the length and form of which may be chosen for solubility) and M is a metal atom (Cd, Sb, Pb, Bi, etc.). Xanthates are charged complexes allowing them to be dissolved in water and other polar solvents. When forming nano particles, xanthates can play two important roles; they can be used as capping agents to stabilize the nanoparticles or they can be used as precursors to form the particles. Changing the temperature or concentration of the metal xanthate complex solution, the shape and size of the nanoparticles can be changed [63], and in some cases rods (wires) or faceted particles can be formed [69]. The xanthate precursor can be used to process a number of different devices, including bulk heterojunctions, sensitized scaffolds and bi-layers. The formation of hybrid organic:inorganic films can be made through an ethylxanthate precursor in a polymer solution, giving rise to a bulk heterojunction. This can be done through an

*in situ* thermal decomposition of the xanthate to form the inorganic phase within the already formed polymer film. The decomposition will happen at relatively low heating of the substrate, and since all the side products are volatile, the resulting thin film contains both the polymer donor and the inorganic acceptor without any residual solvents and side products [70, 71, 72, 73]. Recent studies on solar cells based on the V-VI compound semiconductor Antimony sulphide ( $\text{Sb}_2\text{S}_3$ ) used either as a sensitiser on a mesoporous scaffold of metal oxides, in blends with organic semiconductors or in a flat bi-layer junction with an organic semiconductor. Polycrystalline  $\text{Sb}_2\text{S}_3$  has a band gap of around 1.7 eV, which is good for solar light absorption [74], making it an interesting material for solution precessable solar cells. Furthermore,  $\text{Sb}_2\text{S}_3$  is less toxic than many of the other semiconductors in the metal chalcogenide family such as Cadmium, Lead and Tin based materials.

$\text{Sb}_2\text{S}_3$  has in several studies been reported as being an n-type semiconductor [75, 76].  $\text{Sb}_2\text{S}_3$  thin films have however been shown to give rise to p-type conductivity when doped with carbon [77]. If the doping profiles can be controlled, the possibility of making p-n junctions of the same material is present. Since  $\text{Sb}_2\text{S}_3$  is a naturally n-type material (due to it's fabrication process), it is also important to be able to control the doping concentration in these materials as well as the p-type materials obtained from intentional doping. The reason for the doping naturally arising in  $\text{Sb}_2\text{S}_3$  and similar classes of materials is also important to understand, but at the time of writing this is not known to the author.

### 4.3 Theory of semiconductors

When developing new processing routes to semiconducting thin films, it is important to understand the limits of such materials. The charge transport properties of the semiconductors used in solar cells are important factors to control, and for that reason, measuring mobilities and impurity states is of high interest. In order to model charge transport in  $\text{Sb}_2\text{S}_3$ , some basic semiconductor theory must be discussed, especially with respect to contact interfaces, impurity levels and drift-diffusion current densities. The reason for this will be apparent in the following sections. In the following sections, basic theory of intrinsic and doped semiconductors is presented, with special focus on equations to be used during the treatment of the data. More rigorous analysis of semiconductor theory can be found elsewhere [5, 78, 79].

From a quantum mechanical perspective, charges in atoms can be considered to exist in discrete energy levels, so-called atomic orbitals. As atoms are combined into molecules, the energy levels split, forming molecular orbitals. Considering two similar atoms combining, as in the case of a hydrogen molecule ( $\text{H}_2$ ), the molecular orbital will have two energy levels, a level which is slightly higher in energy and an energy level which is slight lower. These are called the anti-bonding and bonding orbitals respectively. Several atoms can be combined to form molecules of higher complexity, and so, the number of energy levels formed can reach a very high number. Due to electrons being Fermions, it is only possible for two electrons of opposite spin to occupy

an energy level, and for that reason (and at  $T = 0$  K), half of the energy levels are filled up until the highest occupied molecular orbital (HOMO). The rest of the energy levels are empty, starting from the lowest unoccupied molecular orbital (LUMO). The difference between the HOMO and the LUMO is then referred to as the optical gap.

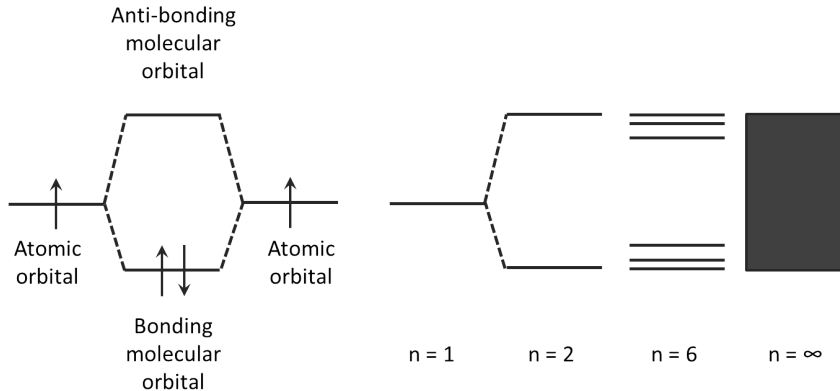


Figure 1: Left: Schematic of energy level splitting when combining atomic orbitals into molecular orbitals. Right: Energy levels going from discrete states to a continuous band in the limit of infinite crystals.

This picture of molecular orbitals can be extended into an infinite crystal of ordered atoms, where the discrete energy levels are no longer distinguishable. One then talk about energy bands [80]. In the case of a semiconductor, there is a gap between the energy bands, much like the optical gap in molecules. This is referred to as the band gap of the material. At zero Kelvin, the lowest energy band is completely filled with electrons, and this band is called the valence band. On the other side of the band gap, the band is completely empty, and this band is called the conduction band. Metals, or conductors, are materials with an overlapping band gap, so that the energy bands are not completely empty or completely full, and charges are then free to move within the material. It is therefore the band gap that gives the semiconductor its properties. Electrons are Fermions because they follow Fermi-Dirac statistics, and at room temperature, some charges are thermally excited across the band gap, giving rise to low electrical conductivity. This thermally excited charge is referred to as the intrinsic charge. Materials with large band gaps will therefore have a lower concentration of intrinsic charge, and they are normally referred to as insulators. Materials with band gaps larger than 2 eV are normally referred to as insulators where materials with band gaps lower than 2 eV are referred to as semiconductors. This is a somewhat arbitrary definition, but is utilized by many in the research community.

Semiconductors are also unique in that they have a band gap where no states are present when the material is intrinsic. It is possible to introduce impurities into the semiconductor to alter its electrical abilities, and in this case such impurities are called doping. Similarly, during the growth process of semiconductors, impurities might be present due to the lack of control. Such unintentional impurities are sometimes not beneficial for the application, as they can act as

charge traps. One can normally distinguish between the two by the fact that doping impurities are purposely so low in ionization energy, that charges being trapped there are quickly released, because the position of the trap level is only  $k_B T$  away from the carrier band. Deeper impurity levels will on the other hand act as traps. In the case of polycrystalline solids, or solids composed of nano- or micro-particles, the imperfect crystallinity will give rise to dangling bonds, which may either act as doping or as trap charges. The band gap is also the parameter giving rise to absorption of photons of visible light. If a photon with an energy equal to or above the band gap energy is incident on the semiconductor, the photon will be absorbed, promoting an electron from the valence band into the conduction band. Such excited charges may then be utilized for photo conduction.

#### 4.3.1 Intrinsic semiconductors

By an intrinsic semiconductor is understood a semiconductor which does not contain any impurities, i.e., a perfect semiconducting crystal. The electron and hole charge carrier concentrations,  $n_i$  and  $p_i$  respectively, are purely governed by the density of states, the temperature, and the band gap of the system. In an intrinsic semiconductor, the electron and hole carrier concentrations will be equal, giving rise to a zero net charge density, or charge neutrality.

#### 4.3.2 Density of states

The number of states per unit energy is called the density of states (DOS). The density of states is an important quantity in semiconductor physics as it yields information about transport properties and optical properties. A large density of states means that a large number of states can be occupied (if empty) or excited (if occupied). For an intrinsic semiconductor, the density of states will be zero in the forbidden gap. For a three-dimensional solid (which are the kinds we will consider in this study), the density of states,  $N$ , will be proportional to the square root of the energy,  $N \propto \sqrt{E}$  (figure 2). At room temperature it is however sufficient to consider the effective density of states,  $N_{C/V}$ , which is a number rather than a distribution.

For a perfect three-dimensional crystal, the effective density of states for electron and holes is given by

$$N_{C/V} = 2 \left( \frac{2\pi m_{e/h}^* k_B T}{h^2} \right)^{\frac{3}{2}} \quad (2)$$

where  $m_e^*$  and  $m_h^*$  is the effective mass of electrons and holes respectively,  $k_B T$  is the thermal energy and  $h$  is Planck's constant. The effective masses is given by the curvature of the band structures. For the purpose of this study, where the nature of the semiconducting films are not exactly known, the effective masses are not known directly either, and it is impossible to

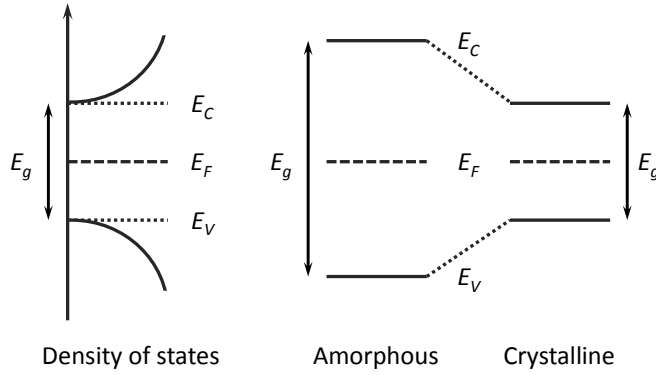


Figure 2: Left: density of states for a three-dimensional semiconductor. Right: Schematic showing band gap reduction from an amorphous to a crystalline material of the same compound.

calculate the exact value for the electrons and holes effective density of states.

For the purpose of this study, and since the effective masses for  $\text{Sb}_2\text{S}_3$  is not directly known, the effective density of states for both electrons and holes will be set to

$$N_C = N_V = 10^{19} \text{ cm}^{-3} \quad (3)$$

which is in the right order of magnitude for most semiconducting materials. In figure 2 the density of states of an intrinsic semiconductor is shown, where  $E_C$  and  $E_V$  denotes the conduction and valence band edges,  $E_g$  is the band gap and  $E_F$  is the Fermi level in the semiconductor, which is a quantity determined by the balance of charges in the bands.

#### 4.3.3 Intrinsic carrier concentrations

Labelling the Fermi level of the intrinsic semiconductor as  $E_i$  we may express the intrinsic carrier concentrations through either the conduction band or valence band as

$$n_i = N_C \exp \left( \frac{E_i - E_C}{k_B T} \right) = N_V \exp \left( \frac{E_V - E_i}{k_B T} \right) \quad (4)$$

where  $N_C$  and  $N_V$  are the effective density of states in the conduction and valence band respectively, and  $k_B T$  is the thermal energy. The square root of the product of the above two equations then yield

$$n_i = p_i = \sqrt{N_C N_V} \exp \left( -\frac{E_g}{2k_B T} \right) \quad (5)$$

where  $E_g$  is the band gap of the material ( $E_C - E_V$ ). By equalling the two expressions for the intrinsic carrier concentrations, an expression for the intrinsic Fermi energy can be derived as

$$E_i = E_V + \frac{1}{2}E_g + \frac{1}{2}k_B T \ln \left( \frac{N_V}{N_C} \right) \quad (6)$$

Given typical values for the effective density of states of both carrier types as  $10^{19} \text{ cm}^{-3}$ , a band gap of 1.7 eV and the thermal energy at room temperature, 0.026 eV, the intrinsic carrier concentration in  $\text{Sb}_2\text{S}_3$  is approximately

$$n_i = p_i = 5.26 \cdot 10^4 \text{ cm}^{-3} \quad (7)$$

with the intrinsic Fermi energy in the middle of the band gap. For the purpose of this study, the exact position of the intrinsic Fermi level is not as important as the approximate position of the Fermi level once dopants are introduced. The exact values for the effective masses for electrons and holes can not be readily obtained, as the band structures will depend on the nature of the film. Band structures of an infinite crystal for most inorganic materials can be found, but since the  $\text{Sb}_2\text{S}_3$  thin films investigated in this study is expected to be composed of regions of nano- or microparticles, the picture of an infinite extended crystal will not most likely suffice. For this reason, the value obtained for the intrinsic carrier concentration calculated above, will be assumed to be sufficient. As a comparison, Silicon and Gallium Arsenide are often cited to have an intrinsic carrier concentration of  $1.5 \cdot 10^{10} \text{ cm}^{-3}$  (1.1 eV) and  $5.0 \cdot 10^7 \text{ cm}^{-3}$  (1.43 eV) respectively. It is seen that the intrinsic carrier concentration drops as the band gap increases.

#### 4.3.4 Doped semiconductors

As was mentioned earlier, if impurities are introduced into an otherwise intrinsic semiconductor, either through intentional incorporation during the growth process or through unintentional incorporation due to lack of control during the growth process, charge carriers in the form of free electrons and/or holes can be introduced if the impurity level is shallow compared to the thermal energy.

Most semiconductors can not be grown as single crystals with high purity levels, and even Gallium Arsenide, in its purest commercially available form, will have carrier concentrations different by more than nine orders of magnitudes from what would be expected from an intrinsic material with a band gap of 1.43 eV [79].

In the case where electrons are given off the impurity site, the doping is called donor type, since electrons are donated from the impurity to the conduction band. In the case where holes are given off, the doping is called acceptor type, since electrons are accepted from the valence band

to the impurity, leaving a vacant hole behind. In the case of shallow impurities (on an energy scale), where the thermal energy is sufficient to ionize the impurity state, the semiconductor will contain free charge carriers, i.e., the semiconductor will be doped. In the case of deep impurities, only a fraction of the states will be ionized, and in the case of an impurity level being many times the magnitude of the thermal energy, the impurity sites can act as traps. Ionized donor states then provide electrons to the conduction band, and the resulting semiconductor is called n-type. Likewise, ionized acceptor states provide holes to the valence band, and the resulting semiconductor is called p-type.

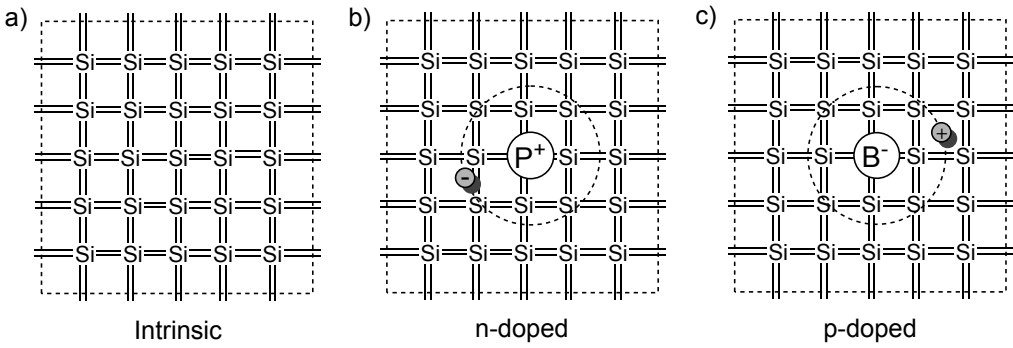


Figure 3: Example of doping in Silicon. a) intrinsic Silicon giving rise to intrinsic carrier concentrations, b) n-doped Silicon, giving rise to large electron carrier concentration, and c) p-doped Silicon, giving rise to large hole carrier concentration.

In figure 3, examples of doping in Silicon are shown (Silicon was chosen as an example since it is a simple system). figure 3a is showing an intrinsic semiconductor crystal, where all four valence electrons for all atoms are fulfilling the octet rule (the crystal shown is highly simplified, and an actual Silicon crystal will form a diamond cubic structure). If a Phosphor atom is introduced into the crystal (figure 3b), the fifth valence electron will not be required for bonding and is therefore free to move around in the crystal. For each incorporated Phosphor atom will then yield a free electron, if ionized, and the semiconductor is now called n-type. Similarly, if a Boron atom is introduced, an additional electron is required for bonding, leaving behind a hole. For each incorporated Boron atom will then add a hole, and the semiconductor is now called p-type (figure 3c).

#### 4.3.5 Ionization of impurities

As was mentioned in the previous section, whether or not the impurities are ionized depends on the thermal energy,  $k_B T$ , and the position of the impurity energy level within the band gap,  $E_g$ . In figure 3, the excess charges are pictured as being bound to the incorporated atom, which is due to Coloumbic forces. These charges can be made free for conduction if the impurity is

ionized, which can be achieved at room temperature. Given that the impurity levels are shallow, it can be assumed that all impurity states will be ionized at room temperature

$$N_d^+ \cong N_d \quad \text{and} \quad N_a^- \cong N_a \quad (8)$$

where  $N_d^+$  and  $N_a^-$  are the concentrations of ionized donors and acceptors respectively, and  $N_d$  and  $N_a$  are the impurity concentrations of donors and acceptors respectively.

In the case of the semiconductor containing both donor and acceptor type dopants, the semiconductor is called compensated. The charge carrier concentrations of electrons and holes will depend on the doping concentrations and the intrinsic carrier concentrations through

$$n = \frac{N_d^+ - N_a^-}{2} + \sqrt{\left(\frac{N_d^+ - N_a^-}{2}\right)^2 + n_i^2} \quad (9)$$

$$p = \frac{N_a^- - N_d^+}{2} + \sqrt{\left(\frac{N_a^- - N_d^+}{2}\right)^2 + n_i^2} \quad (10)$$

If  $N_d^+ = N_a^-$  the net charge carrier concentration will be zero since the carriers resulting from the ionization will compensate each other. However, if the the ionization concentrations are imbalanced, the electron and hole carrier concentrations will be given by

$$n \cong N_d^+ - N_a^- \quad \text{if} \quad N_d^+ - N_a^- \gg n_i \quad (11)$$

$$p \cong N_a^- - N_d^+ \quad \text{if} \quad N_a^- - N_d^+ \gg n_i \quad (12)$$

if the net ionized doping concentration is much larger than the intrinsic carrier concentration. The intrinsic carrier concentration for Sb<sub>2</sub>S<sub>3</sub> was calculated in a previous section to be approximately  $5.26 \cdot 10^4 \text{ cm}^{-3}$ , so given the net doping concentration of shallow dopants is orders of magnitudes higher, the carrier concentrations will be governed by doping.

#### 4.3.6 Doping dependence on Fermi-levels

It was shown in a previous section that the Fermi energy for an intrinsic semiconductor is positioned in the middle of the band gap given that the density of states for electrons and holes are equal. As the charge carrier concentration is shifted away from the value for an intrinsic semiconductor, which is the case for doped semiconductors, which was shown above, the Fermi energy will shift accordingly as

$$E_F = E_i + k_B T \ln \left( \frac{n}{n_i} \right) \quad \text{or} \quad E_F = E_i - k_B T \ln \left( \frac{p}{n_i} \right). \quad (13)$$

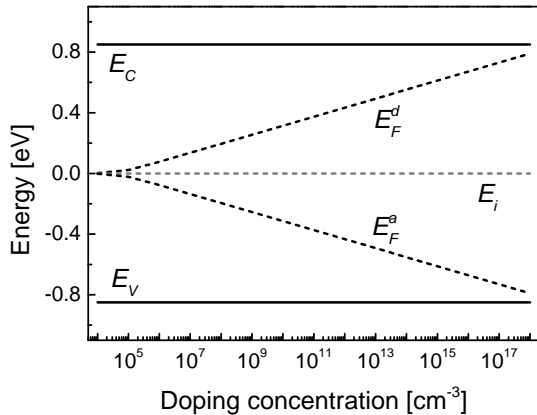


Figure 4: Calculated Fermi energies away from the intrinsic Fermi energy as the net doping concentration of donors and acceptors increase respectively. The Fermi energies were calculated assuming a band gap of 1.7 eV, effective density of states for both electrons and holes of  $10^{19} \text{ cm}^{-3}$  and a temperature of 300 K.

In figure 4 the effect of doping on the Fermi level is seen. As the Fermi level becomes close to the conduction band edge, the semiconductor is said to be n-type, and when the Fermi level is close to the valence band edge, the semiconductor is said to be p-type. This calculation was done for the case of the intrinsic carrier concentration of calculated previously.

#### 4.4 Metal-semiconductor interfaces

When a metal is brought into a contact with a semiconductor, due to the large amount of charge carriers in the metal, charges will be exchanged between the metal and the semiconductor, in order for the system to equilibrate (constant Fermi level).

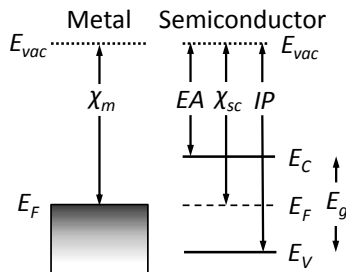


Figure 5: Metal-semiconductor interface prior to equilibrium (before contact). Left: the work function of a metal is defined as the difference between the Fermi level and the vacuum level, right: the semiconductor is defined from the electron affinity (EA), the work function, the ionization potential (IP) and the band gap.

The amount of energy needed to release an electron from a metal to vacuum is called the work function,  $\chi_m$ . It is defined as the energy difference between the Fermi level,  $E_F$ , and the vacuum level,  $E_{vac}$ . The work function is a material dependent parameter which can vary widely. Low work function materials include calcium (-2.9 eV) and cesium (-2.1 eV) and high work function materials include gold (-5.1 eV) and silver (-4.7 eV). Since the work function is a measure of how easy it is to extract an electron from the metal, it is also a measure of how easily the metal will react. Calcium and cesium are both very reactive metals, silver is less reactive but will oxidize, where gold on the other hand is inert. As a rule of thumb, the larger the work function, the less reactive the metal.

Where the metal is defined by its work function, the semiconductor is defined by the electron affinity (EA), the ionization potential (IP), the band gap,  $E_g$ , and the work function,  $\chi_{sc}$ . The amount of energy needed ionize the semiconductor by extracting an electron is governed by the difference between the valence band and the vacuum level, called the ionization potential. For a metal, the energy with the highest energy is positioned at the Fermi level, but for a semiconductor at 0 K, the electrons will fully occupy the valence band, where the electrons must be extracted from. If charges are added to the semiconductor, charges can be added to the conduction band, so the energy gained from adding an electron, would be the difference between the vacuum level and the conduction band, called the electron affinity. The work function of a semiconductor is the difference between the Fermi level and the vacuum level. Similarly to the case of a metal, the parameters explained above will be material dependent, governed by the crystal structure and the weight of the atoms of the lattice through spin-orbit coupling. As has previously been explained, the Fermi level in a semiconductor is highly dependent on the impurity levels in the material, with n-type materials having the Fermi level close to the conduction band and p-type materials having a Fermi level close to the valence band.

Depending on the position of the semiconductor energy levels relative to the metal work function several types of interfaces can be formed. When the metal comes into contact with the semiconductor, the bands in the semiconductor will bend to accompany the charge. This amount of band bending will be governed by the position of the Fermi level in the semiconductor compared to the Fermi level in the metal.

#### 4.4.1 Metal-intrinsic semiconductor interfaces

In the case that the Fermi level of the metal has the same value as the Fermi level in the semiconductor, the bands will not bend because no charge is moved from the metal to the semiconductor upon contact (which would be the case if the energy levels were aligned as in figure 5). However, if the Fermi levels are shifted relative to each other, bending will occur. Figure 6 is showing four types of metal-semiconductor interfaces giving rise to different types of charge injection. If the Fermi level of the metal is larger than the Fermi level of the semiconductor but is aligned with the valence band, an ohmic contact to the valence band will allow for good hole injection into the semiconductor from the metal (figure 6a). In the case that the valence

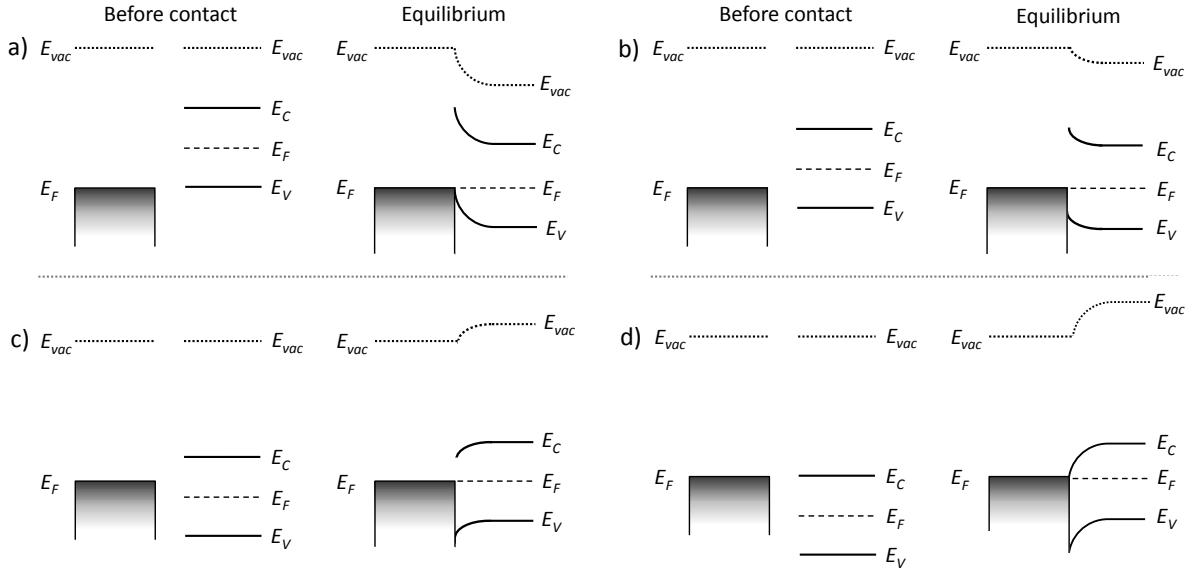


Figure 6: Different metal-semiconductor interfaces for an intrinsic semiconductor, showing a) ohmic contact to the valence band and b) injection barrier to the valence band; c) injection barrier to the conduction band and d) ohmic contact to the conduction band. In a) and b) electron injection is highly limited but hole injection is possible, and in c) and d) hole transport is highly limited but electron transport is possible.

band is slightly deeper than the Fermi level of the metal, an injection barrier for holes will form with a magnitude equal to the difference between the valence band edge and the Fermi level of the metal (figure 6b). If the Fermi level of the metal is smaller than the Fermi level of the semiconductor but not positioned at the conduction band edge, an injection barrier for electrons to the conduction band will form (figure 6c). Finally, if the Fermi level of the metal is aligned with the conduction band edge, ohmic contacts to the semiconductor is present, and electrons can be readily injected into the semiconductor. In the case that the Fermi level of the metal is either deeper than the valence band or shallower than the conduction band, charges will spill into metal until the Fermi level of the metal is aligned with either of the energy bands of the semiconductor, forming ohmic contact to the respective band.

#### 4.4.2 Metal-doped semiconductor interfaces

Since the introduction of doping will shift the position of the Fermi level of the semiconductor, metal semiconductor contacts can form more exotic interfaces. Since this study focuses on electron transport, the metal-semiconductor interface in the case of doping will focus on the electron injection properties.

The Fermi level in an n-type semiconductor will be close to the conduction band. In the case of the intrinsic semiconductor it was shown that by varying the work function of the

metal between the conduction band and the Fermi level of the semiconductor, contacts ranging from ohmic to injection limited could be achieved. Since the energy difference between the conduction band and the Fermi level in an n-type semiconductor is so small, varying the metal work function will have larger consequences. If the metal Fermi level is placed below the Fermi level of the semiconductor (figure 7a), the band bending will cause a rectifying contact to form (Schottky barrier). A forward bias voltage, which would increase the chemical potential of the semiconductor, will allow for electrons to access the metal readily. However, at reverse bias, the barrier height would limit electron injection, causing rectifying behaviour. If the metal work function is placed at the same energy as the conduction band edge or between the conduction band edge and the Fermi level, an ohmic or injection limited contact will be formed.

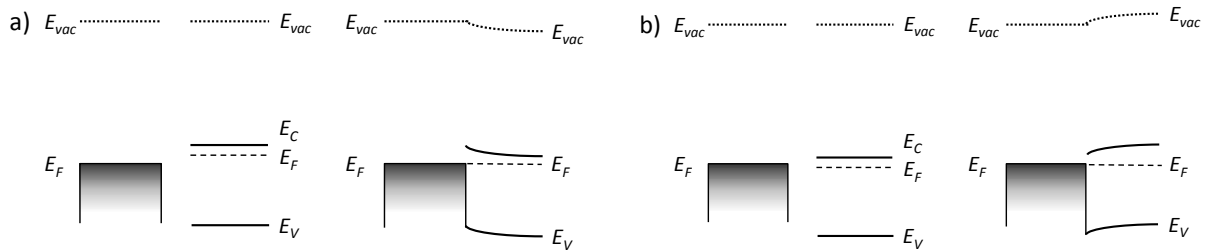


Figure 7: Different metal-semiconductor interfaces for an n-type semiconductor. a) The Fermi level of the metal is larger than the electron affinity and the Fermi level of the semiconductor, resulting in a Schottky barrier. b) The Fermi level of the metal is between the conduction band edge and the Fermi level of the semiconductor, resulting in a injection limited contact. The Schottky barrier will give rise to rectifying behaviour.

From the above discussion it is clear, that in order to achieve a good ohmic contact to a doped semiconductor, it is important to try and match the metal work functions as close to the conduction band as possible, since a small deviation could lead to a Schottky barrier to form. For an intrinsic semiconductor, a small deviation of the metal work function from the conduction band would lead to injection limitation, but not rectification.

#### 4.5 Charge transport in Semiconductors

With the Fermi level, intrinsic charge carrier concentration, doping concentrations and the interface between the semiconductor and the contact described, charge transport in a semiconductor can be described. Firstly, the model equations used for the numerical simulations are presented, secondly, a discussion on modelling of disordered solids is presented, and lastly charge transport in single carrier semiconductor devices is presented.

### 4.5.1 Model equations

When a charge carrier is exerted by an electric field,  $F$ , the charge carrier will accelerate according to ( $\mathcal{F} = qF$ ). Due to scattering within a medium, the charge carrier will obtain a drift velocity, which will be governed by the quantity  $\mu$ , which is called the charge carrier mobility

$$v_{drift} = \mu F. \quad (14)$$

The movement of charge carriers within a medium due to an applied electric field is then called the drift current. The charge carrier diffusion is also governed by the charge carrier mobility through the Einstein diffusion coefficient,  $D$ , and the thermal energy as

$$\mu = \frac{qD}{k_B T}. \quad (15)$$

In order to model charge transport in a semiconducting device, in one spatial direction ( $x$ ), three coupled differential equations must be solved. The first of these equations is concerned with the charge within the device, namely the Poisson equation

$$\frac{d}{dx} \left( \epsilon_0 \epsilon_r \frac{d\varphi}{dx} \right) = -\rho \quad (16)$$

where  $\epsilon_0 \epsilon_r$  is the permittivity,  $\varphi$  is the electric potential and  $\rho$  is the total amount of charge in the device given by the sum of free and localized charge carriers

$$\rho = q(-n + p - n_{loc} + p_{loc}). \quad (17)$$

The two other equations that must be solved are the drift-diffusion equations for electrons and holes (negative and positive charge) respectively. Drift-diffusion currents in one dimension, with a constant diffusion coefficient, constant temperature, constant electric field, constant mobility, and no generation or recombination of charges is generally described by

$$J_n = qD_n \frac{dn}{dx} + n\mu_n \left( -q \frac{d\varphi}{dx} - \frac{d\chi}{dx} - \frac{k_B T}{N_C} \frac{dN_C}{dx} \right) \quad (18)$$

$$J_p = -qD_p \frac{dp}{dx} + p\mu_p \left( -q \frac{d\varphi}{dx} - \frac{d\chi}{dx} - \frac{dE_g}{dx} + \frac{k_B T}{N_V} \frac{dN_V}{dx} \right) \quad (19)$$

for electron and holes respectively. The first term is current due to diffusion and the second term is current due to drift. The charge carrier mobility is present in both terms, with the diffusion term depending on the mobility through  $D$ .

The boundary conditions are set by the contacts of the one dimensional device. The Fermi level of the semiconductor at the device boundaries to the contacts (and hence all the other energy levels) will be governed by the injection and extraction barrier heights,  $\phi_{in/ext}$ . The concentration of charge carriers at the interface to the device is then given by

$$n_{eq} = N_C \exp\left(-\frac{q\phi}{k_B T}\right) \quad \text{and} \quad p_{eq} = n_i^2 / n_{eq}. \quad (20)$$

It is seen that for Ohmic contacts, the charge carrier concentration at the interface will be equal to the effective density of states since  $\phi = 0$ . Furthermore, as the barrier height is increased the concentration of charge carriers at the interface is decreased. The current density over the barrier into the device is then governed by thermionic emission

$$J = AT^2 \exp\left(-\frac{q\phi}{k_B T}\right) \left[ \exp\left(\frac{qV}{k_B T}\right) - 1 \right] \quad (21)$$

where  $A$  is the Richardson constant, and  $V$  is the applied voltage. As the barrier height is increased, the current injection is seen to decrease. At zero bias voltage the term in the hard brackets will be zero, and the current injection will likewise be zero [81].

The barrier heights does not have to be equal at both contacts. If different values for the barriers are used, the asymmetry in charge carriers at the interface will give rise to an electric field across the device, giving rise to a potential difference called the built-in potential,  $qV_{bi}$ .

#### 4.5.2 Extended and localized states

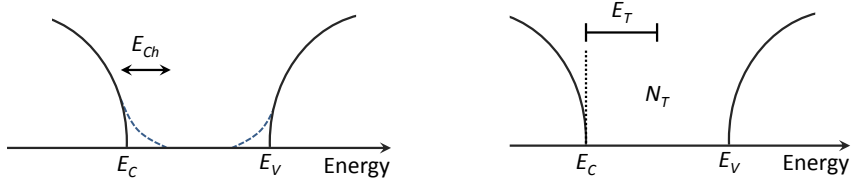


Figure 8: Schematic of density of states for the non-ideal semiconductor. Left: exponential tails reaching into the band gap, where the mobility edges are where the tails coincide with the bands. The depth of the tails is governed by a characteristic energy,  $E_{ch}$ . Right: deep Gaussian traps due to dangling bonds. The position and density of the traps is given by  $E_T$  and  $N_T$  respectively.

For a crystalline material, the transport will take place in the extended states above the band edges due to long range order in the atomic structure. For amorphous materials however, the band gap is increased and exponential tails of localized states reach into the band gap, which is due to the spatial disorder of the material (figure 8 left). For this reason, one can no longer

speak of a well defined conduction and valence band edge, but we then speak of a mobility edge, where all charge carriers above that edge will contribute to charge transport (extended states)[82, 83, 84]. Since charge carriers will get trapped in the localized states, transport will be hindered. Hopping transport and multiple trapping transport between localized states will then dominate transport, greatly lowering the mobility. In multiple trapping transport, the charge carrier will get stuck in a trap until it is re-emitted back into the extended states, from where it can get trapped again. For hopping transport, tunnelling from one localized state to another will happen, but it is assumed that hopping transport is negligible at room temperature, so when including localized states in the device model, the transport will be hindered by multiple trapping mechanisms only [85]. The thermal emission from the localized states to the extended states is governed by single-level Shockley-Read-Hall statistics (A more detailed discussion can be found in the *ASA* manual)[86, 87].

Dangling bonds arising from structural disorder within the lattice, which can give rise to trap states lying deep within the band gap, is described by a Gaussian distribution (figure 8 right) [88]. This distribution can be added act as either acceptor or donor like trap sites, or as amphoteric states by adding a combination of both. For the purpose of this study, only acceptor and donor like traps are considered.

It will be shown in later sections that when a layer of  $Sb_2S_3$  is formed from a xanthate precursor, depending on the processing conditions, amorphous or crystalline material embedded in an amorphous matrix can be formed. For this reason, it is expected that the mobility will be low due to amorphous barriers, where the charge carrier will show good transport properties in the crystalline regions, but will be opposed when trying to overcome an amorphous barrier.

#### 4.5.3 Space-charge-limited currents

Basic theory for intrinsic and doped semiconductors was introduced in the previous sections, where the model equations used calculate charge transport in semiconductors was discussed. For single carrier devices, meaning devices which can only conduct one carrier type either through contact to the conduction and valence band only, the current must be space-charge-limited.

In 1940, Mott and Gurney made the observation, based on the energy-band viewpoint put forward by Bloch, that electrons could be injected into the conduction band of an insulator from a suitable contact, in a manner similar to the thermionic injection of charges from a vacuum tube into vacuum [80, 89, 90]. If a metal is heated to an extent that the thermal energy is greater than the work function of the metal, charges can flow in vacuum (figure 9 a)). This is the fundamental principle behind vacuum tubes. At a metal/semiconductor junction, if the difference between the metal work function and the conduction band is small (compared to  $k_B T$ ), charges ready for conduction will be present at the contact (figure 9 b)). As was already discussed in the previous section, such a contact is called an Ohmic contact. In the case where the injection barrier is large, the interface is said to be injection limited.

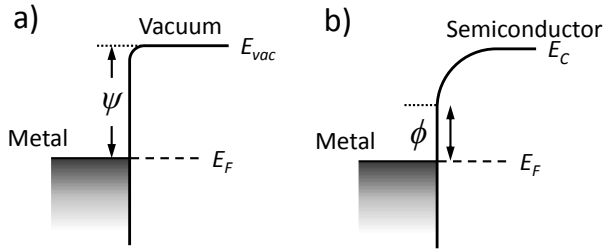


Figure 9: a) metal/vacuum interface where the difference between the Fermi level and the vacuum level is called the work function, and b) metal/semiconductor interface where the difference between the Fermi level and the conduction band edge at the interface is called the injection barrier.

Charge emitted from a metal into either vacuum or a semiconductor is called space-charge. The current in a conductor follows Ohm's law, since charges are neutralized, but in a vacuum or a semiconductor, the current will follow a higher power law dependence depending on the bulk properties of the material. In 1911, Child proposed that the space-charge-limited current (SCLC) density in a parallel-plate vacuum diode varies with voltage according to

$$J = \frac{4\epsilon_r\epsilon_0}{9} \sqrt{2e/m_e} \frac{V^{3/2}}{L^2} \quad (22)$$

which is known as Child's law [91]. Mott and Gurney (1940) proposed a similar law for current densities of a certain carrier type in semiconductors. Assuming that the current is governed by drift-currents only and only carriers of one type are present, that the carrier mobility and the dielectric constant of the semiconductor are constant, that perfect Ohmic contacts, i.e., the injection barrier is negligible, and that the electric field is zero at the point of injection, the current density in semiconductors can be described by

$$J = \frac{9}{8} \mu \epsilon_r \epsilon_0 \frac{V^2}{L^3} \quad (23)$$

which is called the Mott-Gurney law [89, 92, 93]. From the Mott-Gurney law it is seen that the theory offers an easy way to calculate the charge carrier mobility directly from the current density-voltage curves of single carrier devices [94, 95]. Following the work of Mott and Gurney, Rose (1955) and Lampert (1956) extended the theory for intrinsic semiconductors to the case of a single trap level, where both the shape and the magnitude of the current density was shown to be heavily influenced [96, 97]. For this reason, SCLC was proposed as a tool to probe mid gap trap states, and the theory was later extended to include the effect of exponential tail states in the forbidden region [98, 99] and the Poole-Frenkel effect [100, 101]. It is important to note here, and will also be mentioned in later sections, that the analytical equations found in the early literature on charge injection are highly simplified, and give information about the

overall trends of the current densities, but should not be used, directly, as a fitting tool without caution.

The measurements are performed by sandwiching a semiconducting material to be probed between two Ohmic contacts. The contacts do not have to be metals, but merely a source of charge carriers in excess which can be easily injected. Such a contact could be heavily doped semiconductor or a conductive oxide. By matching the Ohmic contacts to either the valence or conduction band, the hole and electron contact can be measured individually. The measurement works by injection of charge carriers into the carrier bands and then measure the current density of the device as a bias voltage is applied.

SCLC measurements have some advantages and disadvantages compared to other mobility measurements techniques. The advantage of using SCLC is that the device being measured is very similar to solar cells devices (sandwich layered architecture), which makes it a powerful tool to measure mobilities while retaining film quality and thicknesses. Considering a very common organic photovoltaic device of ITO/PEDOT:PSS/P3HT:PCBM/Ca/Al, by switching the Ca/Al contact with a contact with a large work function such as gold, a single-carrier hole only device can be fabricated and the hole mobility of the P3HT in the blend can be measured. In this study, the electron mobility of  $\text{Sb}_2\text{S}_3$  will then be measured by carefully choosing electron selective contacts. Other useful mobility measurement techniques exists. One of such is Time of Flight (ToF), which is a transient technique, where a laser is used to excite charge carriers in within a thick slab of semiconducting material. A large positive or negative voltage is applied depending on which charge carrier mobility is being measured, and the time taken for the carriers to escape the semiconductor is measured. However, for ToF, very thick samples on the order of microns are required (depending on the charge carrier mobilities). As the film quality might change as the thickness is increased from nanometres to microns, the measured mobility will most likely differ from what is measured in a thin device. Furthermore, the number of charge carriers in the device during ToF measurements are much less than in the case of SCLC, so the mobility measured will differ due to the different charge carrier regimes. Mobilities can be estimated from Field Effect Transistor (FET) devices. FET mobilities differ from SCLC mobilities in the sense that where SCLC is a volume mobility the FET is a surface mobility. The measurements are analogous in the way that they both rely on Ohmic contacts to either the valence and conduction band, and the current density is measured as a function of applied voltage. Similar problems arise for both SCLC and FET, such as injection limitation which will decrease the current and hence mimic a reduction in mobility. It is problematic to obtain good injection into shallow conduction bands ( $< -3$  eV) due to metals with low work function being very reactive with the ambient atmosphere. Low work function metals such as Ca and Ba are notoriously reactive, with Ca reacting rapidly with water and Ba being very reactive with oxygen. Injection is however not a problem in ToF measurements, as the carriers are injected by means of exciton separation, and since it is easy to extract charges compared to injection. Carefully choosing injection materials and by careful analysis of the SCLC data, information

about the charge carrier mobility, trap states in the band gap and doping can be obtained, as will be discussed in later sections.

## 5 Experimental procedure

The following section will discuss the contact materials used for devices used for the SCLC measurements, the device fabrication procedure, and the measurement techniques employed in this study. The contact materials are presented in context of process-ability and application within the device.

### 5.1 Choice of contact materials

Doped metal oxides are commonly used in organic solar cells due to their high transparencies and their good conductivities. The following section lists the materials chosen for the single carrier devices and solar cells presented in this study, which includes both conductive oxides for front contacts and charge carrier selective interlayers and metals for back contacts.

#### 5.1.1 Tin doped indiumoxide

Tin doped indiumoxide (ITO) is a transparent conductive oxide commonly used in photovoltaics. The high transparency along with the low sheet resistance makes ITO a very good front contact. ITO only absorbs limited light in the UV and infra-red range of the spectrum and will give rise to a small amount of reflection in the infra-red part of the spectrum. ITO is a heavily n-type semiconductor with a band gap around 4 eV. The work function of ITO is usually reported to be around -4.7 ev. Since ITO is so heavily n-type, it is usually considered as a metal, and for that reason, the Fermi level is reported at the same value as the conduction band the valence band of the material is rarely reported.

#### 5.1.2 Titanium dioxide

Titanium dioxide ( $\text{TiO}_2$ ) has a long history of employment in dye-cells and organic solar cells as an electron selective scaffold and as a hole blocking layer in inverted device structures [6, 7, 102]. Similar to ITO,  $\text{TiO}_2$  is highly transparent to visible light, but will absorb some light in the ultraviolet range.  $\text{TiO}_2$  is an n-type semiconductor which can be easily deposited through a precursor, which will be explained to detail in the following sections [28]. The conduction band edge of  $\text{TiO}_2$  is usually reported to be around -4.2 eV, with the Fermi level close to that value due to the material being n-type. With the valence band edge around -7.4 eV, the resulting band gap is estimated to be 3.2 eV.

#### 5.1.3 Molybdenum trioxide

Molybdenum trioxide ( $\text{MoO}_3$ ) is a commonly used interlayer material for organic and hybrid devices with inverted device structure. The exact value for the electron affinity, Fermi level and

ionization potential of  $\text{MoO}_3$  is unclear. Several studies put the work function of  $\text{MoO}_3$  at -5.4 eV [103, 104], however, Kröger *et al* have shown that the conduction band edge lies around -6.7 eV (valence band edge at -9.68 eV) and that the material is highly n-type [105]. For the purpose of this study, it is not highly important exactly where the position of the Fermi level for  $\text{MoO}_3$  is, as long as it is deep enough to act as a good hole collector/injector. Improved hole injection from ITO into  $\alpha$ -NDP (which is a commonly used hole injecting layer in light emitting diodes) has been shown by using  $\text{MoO}_3$  as an interlayer, giving rise to space-charge-limited currents [106, 107]. Good injection into light emitting diodes [103] and transistors [104] has also been reported. For the purpose of this study, the work function of  $\text{MoO}_3$  will be assumed to be at -5.4 eV.

#### 5.1.4 Calcium, Aluminium and Silver

Calcium, aluminium and silver are all metals commonly used in organic and hybrid solar cells. Calcium is a low work function metal with a work function of around -2.9 eV. In order to achieve a high open-circuit voltage, it is important to try and match the work function with the energy levels with the carrier bands, so Calcium being a low work function metal, has time and again been shown to be a good electron contact. However, since calcium is known for its reactivity, it is almost always capped with a thick layer of aluminium to ensure that the calcium does not oxidise. Aluminium has a larger work function than calcium (around -4.1 eV), so the metal is less reactive with ambient gasses.

Silver is a large work function material with very high conductivity. The work function of silver is usually reported to be around -4.7 eV (similar to that of ITO), which makes it a very good hole conductor for most semiconducting materials. Silver is also known to be quite inert, meaning that it wont oxidise easily, making it a very stable contact. This is one of the reasons that inverted device structures, placing the hole contact as the back electrode, have shown higher stabilities to ambient atmosphere.

In the context of this work, Ca/Al contacts will be used as electron injecting contacts into single-carrier devices of  $\text{Sb}_2\text{S}_3$ , and Silver will be used to cap  $\text{MoO}_3$  as a hole extracting and electron blocking contact for the  $\text{Sb}_2\text{S}_3/\text{P}3\text{HT}$  solar cells.

## 5.2 Device and sample fabrication

All films in the following sections (except of the sputtered ITO) were deposited by either spin casting, drop casting or thermal evaporation. All thin films of either interlayers or active materials were deposited by spin casting. Thicker films for XRD were drop cast in order to obtain a good signal. Back contacts, whether they were  $\text{MoO}_3/\text{Ag}$ , Al or Ca/Al were deposited by thermal evaporation under high vacuum inside a glove-box containing an inert atmosphere ( $\text{N}_2$ ).

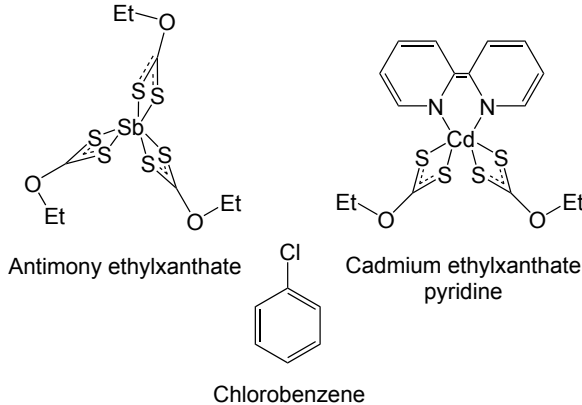


Figure 10: Line-angle formulas for Antimony ethylxanthate ( $\text{Sb}(\text{EX})_3$ ), Cadmium ethylxanthate pyridine ( $\text{Cd}(\text{EX})_2(\text{Pyr})$ ) and Chlorobenzene (CB).

The following section explaining the device fabrication process will outlined as follows: Firstly the pre-fabrication cleaning process of the glass substrates and glass substrates covered in ITO is explained; secondly the preparation of the precursor used to deposit the  $\text{TiO}_2$  layer, the casting method and the decomposition process is explained; thirdly the preparation of the Cd-xanthate ( $\text{Cd}(\text{EX})_2(\text{Pyr})$ ) precursor to form a dense layer of  $\text{CdS}$ , casting method and the decomposition method along with some arguments for the importance for such a layer; fourthly the likewise preparation, casting and decomposition method for the Sb-xanthate ( $\text{Sb}(\text{EX})_3$ ) to form the  $\text{Sb}_2\text{S}_3$  layer; and finally the back contact which is deposited by thermal evaporation under high vacuum. The chemical formulas for the xanthate precursors are shown in figure 10. In the case where devices (or samples) were fabricated differently it will be mentioned specifically.

All samples were made on glass slides containing a predefined ITO strip or on similar glass slides without ITO. The glass slides containing ITO are ordered with the ITO already present on the slide, leaving the thickness of the ITO slide as one of the few parameters which can not be controlled during the fabrication process. All ITO samples were thoroughly cleaned, first by ultrasonication in acetone for 15 min and subsequently by ultrasonication in IPA for 15 min. Before any layers were cast on top of the ITO, the samples were thoroughly dried with gaseous nitrogen. Bare glass slides were cleaned in a similar way, even though the cleaning step was not expected to be as critical due to the lack of ITO. The bare glass slides were used for the XRD measurements where the presence of ITO was not critical for film formation and detrimental for the XRD signal of the probed layer. All solutions were prepared under a fume hood and all film formation were likewise done under a fume hood.

$\text{TiO}_2$  was applied to the ITO through an Titanium isopropoxide precursor (70  $\mu\text{L}$ ) in solution with 55  $\mu\text{L}$  ethanolamine and 1 mL 2-methoxyethanol (figure 11). The solution was spin cast onto the sample at 6000 rpm for 30 s (acc: 2000). The presence of the solution can be seen directly with the eye by the colour change of the ITO strip from a faint purple to a faint green colour. In order to make electrical contact directly onto the ITO on the resulting device, the

precursor was scratched off at one end of the sample using a clean scalpel, and the loosened precursor was wiped off with a cotton tip soaked in acetone. The ITO slide with the precursor was then sintered in a preheated oven at 450°C for 60 min in ambient atmosphere. The resulting TiO<sub>2</sub> film thickness was previously measured to yield approximately 20 nm using this recipe. The band gap of the resulting film is estimated to be around 3.2 eV, with the conduction and valence band edges to be around -4.2 eV and -7.4 eV respectively. With the Fermi level expected to be around the conduction band edge due to the material being highly n-type, the TiO<sub>2</sub> film will act as a good electron injection and extraction contact, with the valence band being so deep that hole injection and collection should be hindered. The UV-vis spectrum of the substrate is seen in figure 11 where the dashed line is showing the absorption of the glass/ITO slide as estimated by the reflectance and the transmittance of the sample. The dotted line is showing the absorption of the glass/ITO/TiO<sub>2</sub> film showing the absorption onset to be around 400 nm which corresponds to a band gap of roughly 3.2 eV.

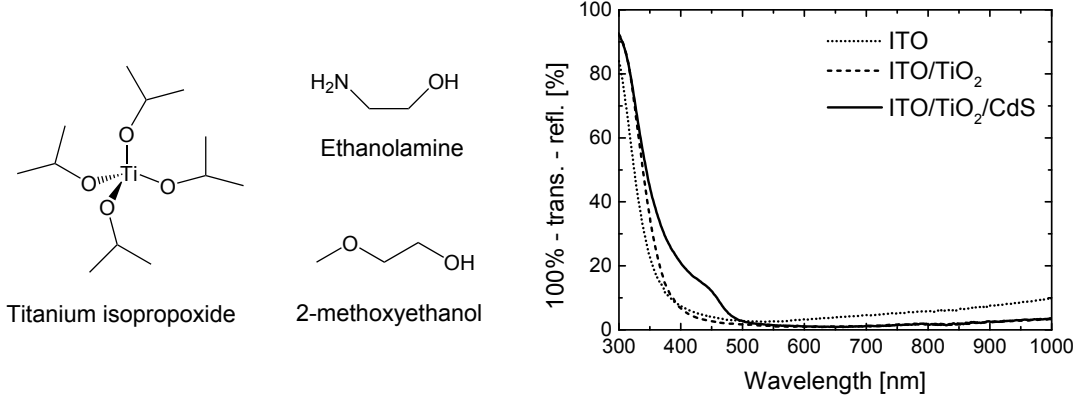


Figure 11: Left: Line-angle formulas for Titanium isopropoxide, Ethanolamine and 2-methoxyethanol which were used to make the TiO<sub>2</sub> precursor solution. Right: UV-vis absorption profile of the substrate containing the electron selective interlayers. The dotted line is showing the absorption of a glass/ITO sample, the dashed line a glass/ITO/TiO<sub>2</sub> and solid line a glass/ITO/TiO<sub>2</sub>/CdS sample.

A dense and thin CdS interlayer was applied between the TiO<sub>2</sub> and the active layer for two reasons, on the one hand it was seen that the wetting of the Sb-xanthate precursor was increased, resulting in more a homogeneous film formation, yielding more efficient devices, and on the other hand, the interlayer was proposed to enhance the crystallinity of the Sb<sub>2</sub>S<sub>3</sub> layer by acting as a seeding layer. Since the CdS layer was included in the solar cell devices previously reported, the layer is likewise included in the current study. The layer was spin cast from a Cd-xanthate precursor (100 mg/mL in CB) at 6000 rpm for 30 s (acc: 2000). The resulting thin film of precursor could clearly been seen with the eye. The precursor films were decomposed on a hotplate inside a glovebox containing an inert atmosphere (N<sub>2</sub>) at 160°C for 30 min. Figure

11 is showing the UV-vis absorption of the resulting glass/ITO/TiO<sub>2</sub>/CdS film, showing the absorption edge to be around 500 nm which corresponds to a band gap of approximately 2.5 eV. The conduction and valence band edges are expected to be around -3.71 eV and -6.13 eV respectively, and since the material is assumed to be n-type, the Fermi energy is expected to be around the value of the conduction band.

With the electron selective front contact, the next step is to deposit the Sb<sub>2</sub>S<sub>3</sub> layer, which was achieved from an Antimony diethylxanthate precursor (Sb(S<sub>2</sub>COEt)<sub>3</sub>) which we will simply refer to as Sb(EX)<sub>3</sub>. A 400 mg/mL solution of Sb(EX)<sub>3</sub> in CB was spin cast onto the glass/ITO/TiO<sub>2</sub>/CdS substrates at 2000 rpm for 30 s (acc: 2000). The precursor film was clearly visible. The precursor films were decomposed at 150°C, 200°C, 250°C and 300°C at either 2, 5 or 10 min on a hotplate in a glovebox containing N<sub>2</sub>. When the xanthate precursor decomposes, a solid film of Sb<sub>2</sub>S<sub>3</sub> will be formed and the ethylxanthate will decompose into volatile gasses of carbonyl sulphide, ethene and hydrogen sulphide (figure 12).

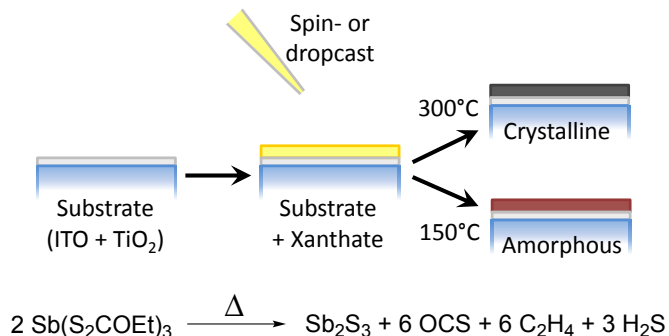


Figure 12: Decomposition of the Antimony ethylxanthate precursor into solid Antimony sulphide, carbonyl sulphide gas, ethene gas and hydrogen sulphide gas as the precursor is heated. The resulting film will be crystalline or amorphous depending on decomposition temperature.

The films were completely amorphous when decomposed at 150°C and the order of crystallinity increased going through 200°C and 250°C to 300°C as will be shown later using XRD and UV-vis. The film formation caused by the xanthate decomposition happened within a few seconds after being placed on the hotplate, and leaving the samples on the hotplate for a total of 2, 5 and 10 minutes is investigated in this study.

After the deposition of the Sb<sub>2</sub>S<sub>3</sub> the samples were transferred to an evaporation chamber where either Ca/Al (or just Al) electron selective contacts or MoO<sub>3</sub>/Ag hole selective contacts were evaporated under high vacuum. For the electron selective contact the evaporation rate of Ca was set to 0.2 Å/s in order to obtain a very smooth film. The Al was evaporated at a much faster rate of 1 Å/s. The resulting thicknesses were 30 nm of Ca and 100 nm of Al. For the hole selective contact the evaporation rate of the MoO<sub>3</sub> was set to 0.1 Å/s. The evaporation rate of Ag was set to 1 Å/s. The resulting thicknesses were 30 nm of MoO<sub>3</sub> and 100 nm of Ag.

Examples of the resulting thin spin cast films and the thick drop cast films are seen in figure

13, where the top row of slides are the thin drop cast films decomposed at various temperatures in the range: 150°C, 200°C, 250°C and 300°C, and the bottom row are thick drop cast films decomposed at temperatures in the range: 150°C, 200°C, 250°C and 300°C. The photographs of the thick films were taken from the glass side due to the surface of the films being rough. The photographs of the thin films were taken from the Sb<sub>2</sub>S<sub>3</sub> side.

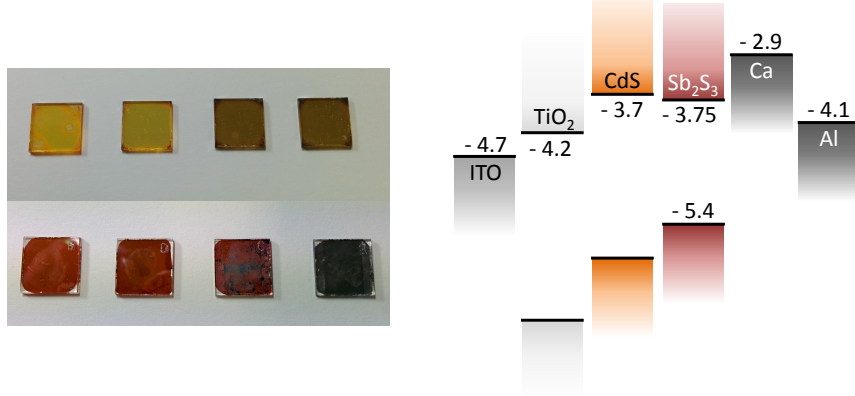


Figure 13: Photographs of samples used for UV-vis and XRD, and schematic for the resulting structure of the electron-only devices, showing the work function values for the contacts, and the conduction and valence band edge energy values for the semiconductors in the device. Top row (left to right): thin spin cast samples of Sb<sub>2</sub>S<sub>3</sub>; decomposition at 150°C, 200°C, 250°C and 300°C for 10 min. Bottom (left to right): thick drop cast samples of Sb<sub>2</sub>S<sub>3</sub>; decomposition at 150°C, 200°C, 250°C and 300°C for 10 min.

The solar cells which we were fabricated and measured to compare with the single carrier devices used the same front contact of ITO/TiO<sub>2</sub>/CdS but a back contact of MoO<sub>3</sub>/Ag. The solar cells were made as bi-layer devices with the Sb<sub>2</sub>S<sub>3</sub> layer deposited as described above and the P3HT layer was deposited from a 20 mg/mL solution of the polymer in CB. The polymer was applied by spin casting the solution at 2000 rpm for 30 s. The sample containing the inorganic layers were firstly rinsed in IPA and blown with nitrogen. The samples were then transferred to a glove box for back electrode evaporation (MoO<sub>3</sub>/Ag).

### 5.3 Performed measurements

#### 5.3.1 UV-Vis

The band gap of a material will be governed by the crystallinity. An amorphous film will have a larger band gap than a crystalline film of the same material. The absorption onset is governed by the band gap, so measuring the absorption of a film as a function of the wavelength of probed light, will yield information about whether the material is crystalline or amorphous.

The absorption profiles were obtained from measuring the reflectance and the transmittance of

the samples using an integrating sphere UV-vis. Given that the samples are thin enough, some light will be transmitted, some light will be absorbed and some light will be reflected depending on the refractive index and extinction coefficient of the material. It is then assumed that the sum of the reflectance, transmittance and absorption is 100%. The absorption profiles were measured on thin spin cast samples described in the device and sample fabrication section.

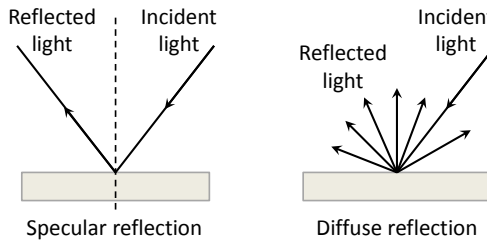


Figure 14: Two different kinds of reflection; left: specular reflection, which is light reflected symmetrically with respect to the normal line (dashed line), and right: diffuse reflection which is reflection caused by scattering within a polycrystalline solid.

In figure 14, two types of reflections are shown, namely specular and diffuse. Where the specular reflection is mirror like, the diffuse reflection is reflected at all angles due to scattering within a polycrystalline solid. Rough surfaces also scatter light, but diffuse light does not require rough surfaces to be present. Specular reflection typically occurs from metallic surfaces (such as mirrors) and diffuse reflection typically occurs from rough surfaces or samples of polycrystalline particles such as white paint ( $\text{TiO}_2$ ).

Since the samples to be measured contain  $\text{TiO}_2$ , and the thin films of  $\text{Sb}_2\text{S}_3$  are most likely consisting of nano- or micro-particles of crystalline material embedded in an amorphous material, one needs to consider the diffuse reflection. This is achieved by using an integrating sphere containing a perfect scattering material such that all the scattered light from the sample reaches the detector.

### 5.3.2 XRD

X-ray diffraction (XRD) is a tool to probe the crystallinity of a material. XRD measurements is used in this study to understand how the film of antimony sulphide forms as a function of decomposition temperature of the precursor and how the film changes with annealing time. The XRD data is compared to the absorption profile of the film as the decomposition temperature and annealing time is varied.

When X-rays (electromagnetic waves of high energy) are incident on an atom, the electromagnetic wave causes the electron cloud around to atom to vibrate. This vibration causes the atom to re-radiate electromagnetic radiation at the same frequency. Crystals are consisting of atoms

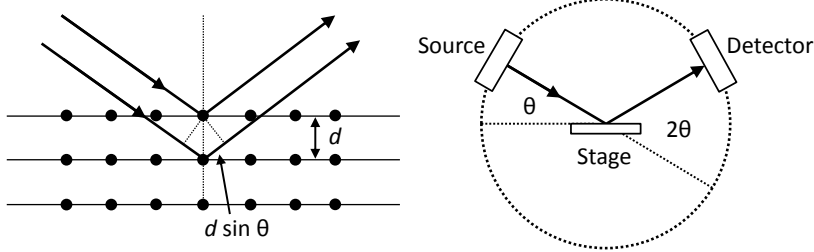


Figure 15: Left: Condition for Bragg diffraction. Right: XRD setup, showing the reason for the sweep of  $2\Theta$  for the output data.

arranged in perfect ordered patterns (lattice). When X-rays are incident on crystalline material at certain angles, constructive interference between the re-radiated X-rays from the ordered atoms give rise to intense peaks (Bragg diffraction). The condition for constructive interference is expressed by Bragg's law (as shown in figure 15)

$$n\lambda = 2d \sin \Theta \quad (24)$$

where  $n$  is an integer,  $\lambda$  is the wavelength of probed electromagnetic radiation,  $d$  is the spacing between the crystal planes in the atomic lattice, and  $\Theta$  is the angle between the incident ray of electromagnetic radiation and the scattering plane. Depending on the crystallinity and the type of crystal being measured, the intensity of the peaks and the position of the peaks as a function of  $2\Theta$ , will vary. Calculated patterns for the different materials used in this study are found in the section on device and sample fabrication.

All X-ray diffraction (XRD) measurements were performed by Dr. Thomas Rath at the Department of Chemistry, Imperial College London, UK.

### 5.3.3 SEM

A scanning electron microscope (SEM) is an electron microscope which obtains an image by scanning of a focused beam of accelerated electrons from a cathode filament. The accelerated electrons will then interact with the sample, generating Auger, secondary or backscattered electrons and X-rays. The various generated signals will then yield information about surface topography and/or material composition. An SEM typically operates under ultra high vacuum, and depending on the probed sample and the chosen voltage, a very high resolution can be achieved (1 nm) [108, 109, 110].

In a typical SEM, the electron beam is generated through thermionic emission from the cathode, which is commonly a tungsten filament. The applied acceleration voltage of the electrons is typically in the order of keV, with the exact value depending on the sample being probed. A higher applied voltage will typically render an image of higher resolution, however, unstable samples or samples of organic materials might be damaged if a too high voltage is applied.

The electron beam is focused onto the samples by the apertures and the condenser and objective lenses (magnetic). The beam is deflected onto the sample by the scan coils to allow for scanning, where the secondary electrons are detected, generating the image (figure 16 left). The size of the interaction volume will depend on the magnitude of the applied voltage, where the volume will increase with an increased voltage, and will be smaller when the atomic number is increased. Larger atoms will more easily stop the electrons from penetrating (figure 16 right). Secondary electrons are typically the electrons being used to generate an three-dimensional like image, which are generated within the first few nanometres of the sample, where the backscattered electrons will give information about chemical composition since the electrons are coming from much deeper within the sample and the signal strength will depend more highly on atomic number. X-rays can also be detected through *in situ* energy-dispersive x-ray spectroscopy (EDX), which will also yield information about the exact chemical composition at a given point on the sample onto where the beam is focused. Information given by secondary electrons and x-rays will be used in this study.

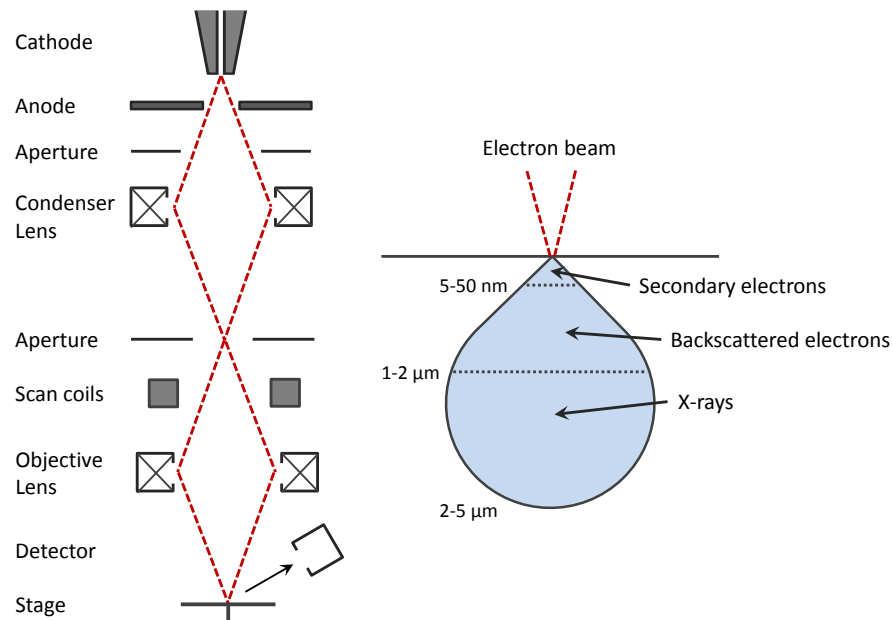


Figure 16: Left: Schematic of a scanning electron microscope. Right: Interaction volume, showing the depth of penetration of the electron beam.

### 5.3.4 Space-charge-limited current measurements

Space-charge-limited current (SCLC) measurements were performed in the dark using a sample holder which encapsulate the single carrier devices in inert atmosphere ( $N_2$ ). Oxygen and water might react with the materials in the devices, which is especially the case of Calcium. Aluminium and Silver are also known to oxidise to some extent (with Silver being more inert). Oxidization of metals will change their respective work functions, which could be detriment-

tal for charge injection into the devices. The current density-voltage curves were obtained by sweeping from negative to positive bias voltage (-5 V to 5 V) in steps of 0.05 V. The voltage sweep was set to a slow speed to ensure that transient effects were minute so that the device was measured under steady-state conditions. All devices within the same batch were measured on the same day following evaporation of the back contact. The devices were only taken out of the glove box containing nitrogen for area and thickness measurements where after the devices were stored in a glove box. No post fabrication annealing of the devices were performed. The SCLC measurements were performed on the same setup as the solar cells.

Different methods have been used to estimate the mobility in single-carrier devices, from fitting with different analytical equations to numerical fitting using a drift-diffusion solver. The analytical tools, trying to incorporate the effects of traps, diffusion and built-in potentials, are vast. The validity of these equations and the regimes in which they can be used can be discussed (like the assumption made in order to obtain the Mott-Gurney law), so for the sake of avoiding the issue of applicability and to increase the accuracy for the determination of the device parameters, a numerical model will be used.

### 5.3.5 Solar simulation

The measured solar cells were placed in a sample holder containing nitrogen similar to when single carrier devices were measured. The current density-voltage characteristics were obtained both in the dark and under AM1.5 simulated solar light. The curves were usually recorded from -1.5 V to 1.5 V. The open circuit voltage, short-circuit current density, fill factor and ultimately the power conversion efficiency was then recorded. All devices were assumed an active area of 0.045 cm<sup>2</sup>. The solar simulator was calibrated using a commercial inorganic photo diode. Both the space-charge-limited current measurements and the solar cells were measured using the same setup to ensure that the devices could be compared directly.

## 6 Results and discussion

The following results section are divided into several subsections, with the first being about fabrication of crystalline antimony sulphide films from the Sb-xanthate precursor, the second being on modelling results and, the third being on SCLC results. The modelling results are paramount for the understanding of the experimental results, so for the benefit of the reader, these will be introduced first.

### 6.1 $\text{Sb}_2\text{S}_3$ films

#### 6.1.1 Crystallinity

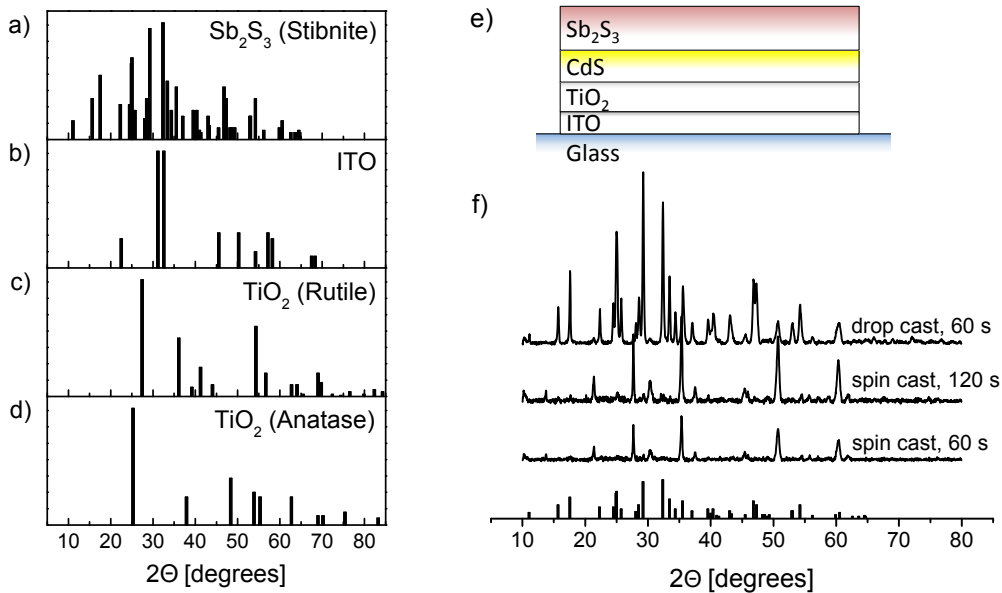


Figure 17: Calculated XRD reference patterns for a)  $\text{Sb}_2\text{S}_3$  in Stibnite crystal structure, b) tin-doped indium oxide, and two forms of  $\text{TiO}_2$ , namely c) Rutile and d) Anatase. e) Schematic of the substrate, the interlayers and  $\text{Sb}_2\text{S}_3$ . f) XRD traces of glass/ITO/TiO<sub>2</sub>/CdS/ $\text{Sb}_2\text{S}_3$  films, which were formed from decomposition of either drop or spin cast  $\text{Sb}(\text{EX})_3$  at 300°. For the spin cast films, the collating time was set to either 60 or 120 s.

In order to quantify the crystallinity of the  $\text{Sb}_2\text{S}_3$  films, XRD and UV-vis absorption spectra of spin cast thin films and thick drop cast films were measured. In order to ensure that the film morphology and crystallinity was comparable to the films in the reported solar cells, glass substrates containing ITO/TiO<sub>2</sub>/CdS were used. Amorphous materials have higher band gaps than crystalline materials so a red shift of the absorption onset is expected of crystalline  $\text{Sb}_2\text{S}_3$  films compared to amorphous films. Furthermore, the absorption above the energy of the

absorption onset is likewise expected to be lower for crystalline materials than for amorphous materials due to crystalline materials reflecting more light. UV-vis measurements are then expected to show high absorption at shorter wavelengths for amorphous Sb<sub>2</sub>S<sub>3</sub> and slightly lower absorption at longer wavelengths for crystalline Sb<sub>2</sub>S<sub>3</sub>. Due to the poor fabrication control and very quick decomposition of the xanthate precursor when the films are formed, a fully crystalline material can not be expected. It is for that reason highly likely that a mixture of amorphous and crystalline material is found in the resulting film.

In figure 17a)-d), the reference patterns for XRD is seen for Sb<sub>2</sub>S<sub>3</sub> (Stibnite), ITO and two polymorphs of TiO<sub>2</sub>, namely Rutile and Anatese. It is apparent that the XRD pattern for Stibnite contains more features at a wide range of angles of incidence. However, it is also seen that ITO and TiO<sub>2</sub> in its different crystal structures will have their most intense peaks at the positions of the most intense peaks of the Stibnite. This is especially the case for ITO and Rutile.

Figure 17f) is showing the XRD traces of spin cast and drop cast Sb<sub>2</sub>S<sub>3</sub> films, which were formed by decomposition of Sb(EX)<sub>3</sub> at 300°C, on glass/ITO/TiO<sub>2</sub>/CdS substrates (figure 17e). The figure is also showing the calculated Sb<sub>2</sub>S<sub>3</sub> (Stibnite) reference pattern, which is showing very profound peaks especially around 25, 28 and 33 degrees. For the thin spin cast films it is quite noticeable that none of the profound peaks expected to be seen are present, which is due to the signal being washed out by a very strong Rutile signal. Increasing the collating time from 60 to 120 s did not improve the trace substantially, giving only rise to minor peaks at the expected angles of incidence. The drop cast film is giving rise to a very strong trace, showing profound peaks which correspond very well to the reference pattern of Stibnite. The peaks from the TiO<sub>2</sub> are still present however less intense.

Due to the thin samples giving rise to a very poor signal, all XRD measurements were performed using thick drop cast films. The XRD traces from drop cast films of Sb<sub>2</sub>S<sub>3</sub> decomposed at different temperatures of 150°C, 200°C, 250°C and 300°C is seen in figure 18a). It is seen that at low decomposition temperatures (150 °C), the resulting film is completely amorphous with no visible peaks at any of the calculated angles of incidence. The somewhat wiggly line observed is due to the software used not being able to subtract the background noise properly. It is also quite apparent that the signal from the TiO<sub>2</sub> is not present due to the thickness of the device. At 200°C some peaks are barely visible, pointing to the fact that some degree of crystallinity is present within the amorphous film. At 250°C the XRD pattern suggest that the decomposed film is quite crystalline, with profound peaks present. Finally, at 300°C, the film is found to be very crystalline, giving rise to very intense peaks where expected.

To further improve the XRD signal, the Sb<sub>2</sub>S<sub>3</sub> was deposited onto glass/TiO<sub>2</sub> slides, omitting the ITO. When trying to drop cast Sb(EX)<sub>3</sub> onto bare glass slides, the solution was found to wet very poorly. Upon evaporation of the solvent and decomposition of the viscous film of Sb(EX)<sub>3</sub> precursor, due to the poor wetting, the Sb(EX)<sub>3</sub> film will form a droplet, due to the volatile side products, in the middle of the glass slide. As this bubble bursts, the material is flung off the

substrate leaving only a minor amount of material on the sample. For this reason, it was found that the  $\text{TiO}_2$  increased the wetting of the  $\text{Sb}(\text{EX})_3$  solution profoundly, giving rise to uniform and thick drop cast films.

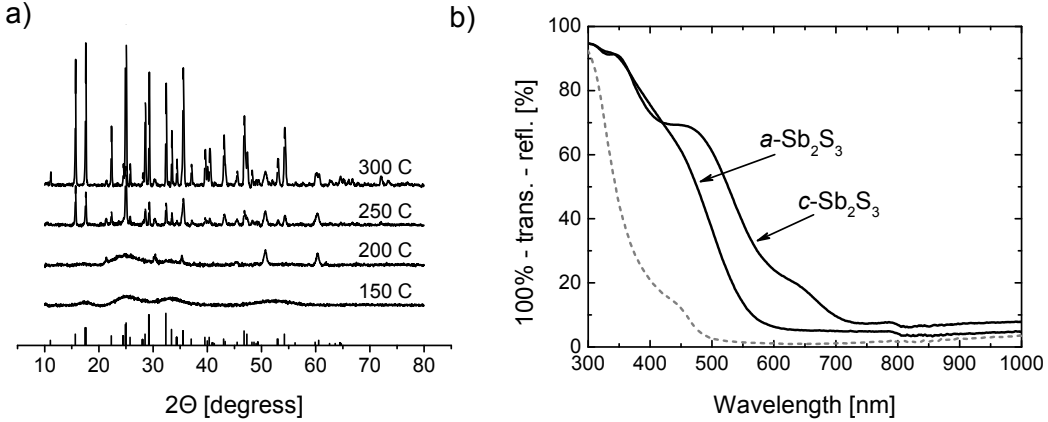


Figure 18: a) XRD traces of glass/ $\text{TiO}_2$ /Sb<sub>2</sub>S<sub>3</sub> films, which were formed from decomposition of drop cast Sb(EX)<sub>3</sub> at either 150°, 200°, 250° or 300°. The calculated Sb<sub>2</sub>S<sub>3</sub> (Stibnite) is seen in the bottom of the graph. b) UV-vis absorption profile of the substrate containing the electron selective interlayers (grey dashed line) a substrate with decomposed Sb(EX)<sub>3</sub> at 150 °C (*a*-Sb<sub>2</sub>S<sub>3</sub>) and a substrate with decomposed Sb(EX)<sub>3</sub> at 300 °C (*c*-Sb<sub>2</sub>S<sub>3</sub>). *a*- and *c*-Sb<sub>2</sub>S<sub>3</sub> denotes amorphous and crystalline antimony sulphide respectively.

UV-vis absorption measurements were performed of thin films of Sb<sub>2</sub>S<sub>3</sub> on glass/ITO/TiO<sub>2</sub>/CdS substrates decomposed at two different temperatures of 150°C and 300°C (figure 18). It is seen that the Sb<sub>2</sub>S<sub>3</sub> film decomposed at 150°C has its absorption onset at lower wavelengths, more specifically at around 550 nm, which is roughly equivalent to a band gap of 2.25 eV. Comparing the UV-vis absorption profiles to the XRD traces in figure 18 it is apparent that films decomposed at 150°C are amorphous. In figure 18b) it is seen that films decomposed at 300°C has an absorption onset around 730 nm which is roughly equivalent to a band gap of 1.7 eV. Comparing this absorption profile to the XRD traces at 300°C it is apparent that the films decomposed at 300°C are crystalline in nature. However, from the absorption profile it is seen that the crystalline film joins the amorphous absorption around 400 nm, indicating that the resulting film is a combination of amorphous and crystalline Sb<sub>2</sub>S<sub>3</sub> when decomposed at 300°C. It is most likely that the film composes of crystalline regimes separated by amorphous regions. For this reason, the charge transport characteristics are not expected to behave as for a perfect crystalline material, but rather as a disordered solid.

The crystallinity of the Sb<sub>2</sub>S<sub>3</sub> films were investigated as a function of the decomposition time. Since the decomposition of the films only take a few seconds after being put on the hot plate, the decomposition time is more precisely a combination of the short decomposition time and an annealing time of the films. Figure 19 is showing XRD data and UV-vis data of thick

and thin films of  $\text{Sb}_2\text{S}_3$  respectively as the decomposition time is increased from 2 to 10 min. The films were decomposed on a dense layer of  $\text{TiO}_2$  to ensure good wetting of the precursor solution which is important for uniform film formation. The XRD spectra are showing profound peaks where expected which does not change significantly with increased annealing time. The UV-vis spectra are similarly showing no significant improvement of the films with annealing times. The small differences shown in figure 19b) could be due to minor thickness variations or small differences in how the samples were placed during the UV-vis measurements. Since the decomposition of the  $\text{Sb}_2\text{S}_3$  was done at 300°C for the solar cells presented in recent studies, the charge transport for similar thin films will be investigated in this study.

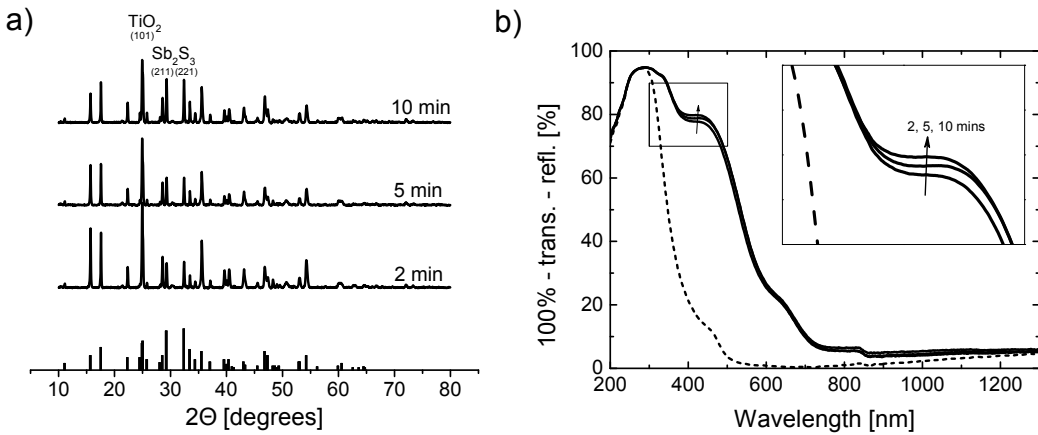


Figure 19: a) XRD spectra of  $\text{Sb}_2\text{S}_3$  thick films decomposed from  $\text{Sb}(\text{EX})_3$  at 300° at different times. b) UV-vis spectra of  $\text{Sb}_2\text{S}_3$  thin films.

### 6.1.2 Material surface coverage

The surface coverage of the devices of ITO/ $\text{TiO}_2$ /CdS/ $\text{Sb}_2\text{S}_3$ /Ca/Al were investigated using SEM. The samples were the same as those in which SCLC was measured. To avoid charging of the sample, in order to achieve images of high resolution, a thin layer (approximately 20 nm) of Pd/Au was sputtered onto the samples. The samples were measured in ultra high vacuum using an acceleration voltage of 12 kV and a working distance of 13.9 mm.

Figure 20 is showing the SEM images of the surface of a typical sample. a) and b) are images of the surface where the layers were deposited on ITO and on glass respectively. Large crystallites of what is believed to be  $\text{Sb}_2\text{S}_3$  which was assessed from EDX measurements performed *in situ* is seen in both a) and b). The small bright crystals surrounding the larger crystallites in b) are believed to be amorphous  $\text{Sb}_2\text{S}_3$ , which is more profound in b) than in a). This could be attributed to a better wetting of the precursor on the ITO covered part of the film, which would result in a more uniform film formation, yielding less amorphous material. Moreover, the surface is seen to be more uniformly covered in a). c) and d) is showing the sample sample but in a region where the sample is covered by a Ca/Al contact. The contact is seen cover the film

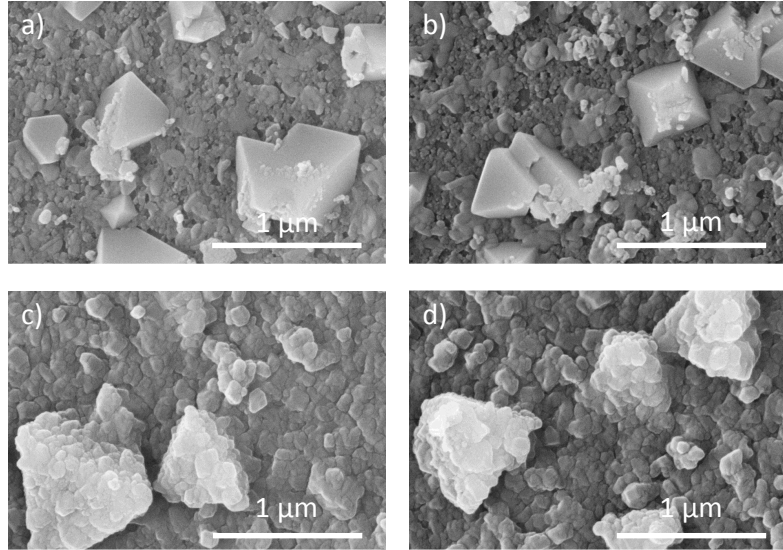


Figure 20: Scanning electron micrographs of the surface of a typical electron only sample. a)  $\text{Sb}_2\text{S}_3$  deposited on ITO/TiO<sub>2</sub>/CdS, no back contact, b)  $\text{Sb}_2\text{S}_3$  on TiO<sub>2</sub>/CdS, no back contact, c)  $\text{Sb}_2\text{S}_3$  on ITO/TiO<sub>2</sub>/CdS with Ca/Al back contact, and d)  $\text{Sb}_2\text{S}_3$  on TiO<sub>2</sub>/CdS with Ca/Al back contact. The sample was covered in 20 nm Pd/Au to avoid charging effects.

nicely in both cases. For this reason it is assumed that good contact to the probed material is realised.

It should be emphasized that cross section SEM images was not successfully performed at the time of writing due to charging of the glass substrate was interfering with the image. However, the samples were still investigated using a fast scan speed of the cross section. From the analysis it is determined that the surface coverage of  $\text{Sb}_2\text{S}_3$  is uniform and that no evidence of pin holes is present for the thin films used for SCLC measurements. The film thicknesses could also not be determined precisely since cross section SEM could not be realised. For that reason, it will assumed that the thicknesses are similar to what have been reported in previous studies using the same recipes and the same processing conditions.

### 6.1.3 Nano- and microstructures of thick films

The micro structure of the thick drop cast samples were investigated by cross section SEM. A typical sample of a crystalline film decomposed at 300°C was cleaved by cutting a grove down the glass slide on the backside of the sample and then broken in half. The sample was cut on the backside to ensure that the sample would have a clean cut on the side containing the semiconductor. The sample was placed horizontally in the SEM, and a piece of carbon tape was placed so that the  $\text{Sb}_2\text{S}_3$  was conductively connected to the sample holder.

Figure 21 a) is showing a micrograph obtained with 1000 times magnification. The film is seen

to be roughly 100 microns thick as a result of the drop casting of the precursor. The film is seen to be highly porous. The porosity is most likely due to the quick decomposition rate of the precursor, where the volatile side products and the remaining solvent (which might be present) in the precursor film escapes the film during formation. The glass substrate can be seen in the bottom of the micrograph as a bright white band. This brightness of the glass is due to charging which disturbs the signal. A very thin bright line can be seen between the  $\text{Sb}_2\text{S}_3$  and the glass substrate which is attributed to  $\text{TiO}_2$ .

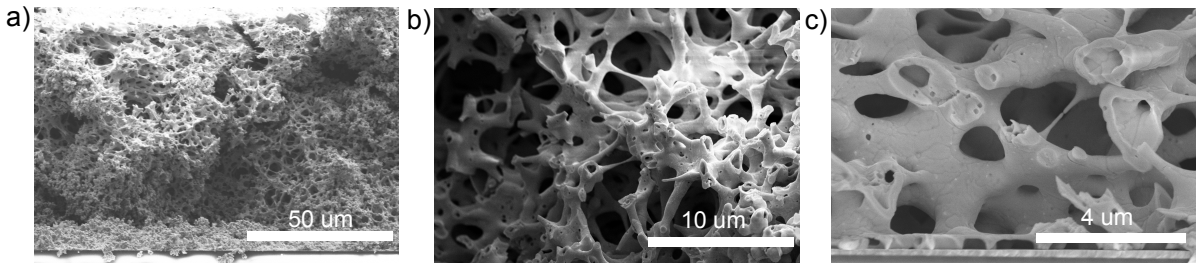


Figure 21: Scanning electron micrograph of cross section of thick drop cast film of  $\text{Sb}_2\text{S}_3$  on  $\text{TiO}_2$ . The acceleration voltage was set to 5 kV to avoid charging, the working distance was set to 7 mm. a) 1000 times magnification, b) 5000 times magnification and c) 13000 times magnification. The glass substrate is seen in the bottom of the micrograph as a white region in a), which is due to charging. A very thin layer of  $\text{TiO}_2$  can be seen between the glass and the  $\text{Sb}_2\text{S}_3$ .

Figure 21 b) is showing a micrograph of a higher magnification (5000 times) of the porous network shown in figure 21 a). The porosity of the film is more clearly visible in this image, and it can also be seen that the pipework of material is hollow. The pipe structures are seen to be between nanometres and microns thick. Figure 21 c) is showing a micrograph with an even higher magnification (13000 times) of the thick film close to the substrate. The thin layer of  $\text{TiO}_2$  is clearly visible between the glass and the  $\text{Sb}_2\text{S}_3$ . In this image, it is more clearly seen that the pipes are hollow, and that the film does not cover the  $\text{TiO}_2$  layer uniformly, which is probably due to a combination of the quick decomposition and poor wetting of the precursor on the substrate. The thick samples were primarily fabricated in order to obtain a good XRD signal, such that the crystallinity of the  $\text{Sb}_2\text{S}_3$  samples could be assessed as a function of decomposition temperature. However, measurements such as Time of Flight mobility measurements require thick and uniform films, and if future measurements are to be made of such devices, a lot of work has to be done in controlling the decomposition step for these films. The very fast decomposition is clearly a problem for the film formation, so it is proposed by the author, that the thick drop cast films are decomposed at a very slow level, starting from room temperature and slowly increasing the temperature to 300°C. From preliminary studies (not shown here), it is proposed that crystalline films can be formed from already formed amorphous films simply by increasing the temperature from 150°C to 300°C. The slow decomposition step could be a

route to fabricate thick uniform films. Alternatively, the porous film could itself be filled with a precursor solution of the xanthate precursor to form a thick uniform film.

## 6.2 SCLC modelling results

In order to understand the outcome of the space-charge-limited current measurements on the Antimony sulphide thin films, preliminary drift-diffusion modelling was performed investigating the effect of a number of factors that could affect the experimental measurements, namely effects of injection barriers and electrode asymmetry, trap states and intentional doping.

The following results were obtained by modelling of a semiconductor in a sandwich structure with two metals using Advanced Semiconductor Analysis (*ASA*)[111]. The majority of the presented results will be in the form of current density-voltage curves (*J-V*), and in the form of slope-voltage curves (*n-V*). The slope function,  $n$ , is defined as the slope of the *J-V* curve on a log-log scale

$$n = \frac{d \log J}{d \log V}. \quad (25)$$

The slope-voltage curves are important as the position of the slope maximum on the voltage axis and the magnitude of the slope will yield important information about the nature of the device as will be seen in the following sections [112]. Generally, when fitting to SCLC data, it is important to fit to the *J-V* curves as well as the *n-V* curves. It can be argued that all the important information of the underlying physics of a single carrier device can be found in the slope function where the current density will merely yield information about the magnitude of the charge carrier mobilities. It is important to note here, that  $n$  does not denote the electron charge carrier density.

Since  $n$  gives the slope of the *J-V* curve on a log-log scale, that is equivalent as saying that  $n$  is the power law dependency of the current density on the applied voltage

$$J \propto V^n. \quad (26)$$

From this definition we can attribute different values of  $n$  to different types of electrical characteristics. For a conductor or a resistor, Ohm's law,  $J = \sigma V/L$ , where  $\sigma$  is the conductivity, states that the current density will follow the voltage linearly, and so  $n = 1$ . It was shown in a previous section that for an intrinsic semiconductor, with perfect Ohmic contacts, diffusion free currents and injection point at the boundary of the semiconductor, that the current density follows the voltage by  $J = (9/8)\mu\epsilon_r\epsilon_0(V^2/L^3)$ , so in the case for an ideal semiconductor,  $n = 2$ . It is possible to attribute higher values of  $n$  to cases where diffusion current dominate, which is especially apparent when built-in potential are present due to contact asymmetry and when traps are present [113]. Such cases will be shown in the following sections, and has been calculated analytically in the past by Mark and Helfrich, who showed that exponential tail states

extending from the conduction and/or valence bands in semiconductors will give rise to diffusion barriers causing higher orders of  $n$  to arise according to  $J \propto V^{l+1}$ , where  $l$  is dependent on the depth of the tails through  $l = E_{ch}/k_B T$ , where  $E_{ch}$  is a characteristic energy [99]. It was however pointed out by Lambert and Mark himself that such analytical equations should only be used to understand the underlying trends of such trap behaviour and should by no means be used as a fitting tool (a statement which the author and others have recently confirmed) [90, 114, 115].

Results similar to some of the following modelling results have previously been presented in another Master's thesis (thickness dependence on  $J-V$  curves when traps are present, and determination of built-in potentials from forward and reverse bias)[114]. However, the results were presented in the context of understanding trap states in organic single carrier devices It should however be noted that the focus of this work is neither to determine trap states or estimating built-in potentials, and the work is simply presented to rule out these phenomena. All model parameters are presented in table 1

Table 1: Drift-diffusion simulation parameters

Parameter	Symbol	Preliminary	Fitting	Units
Electron mobility	$\mu_e$	variable	variable	$\text{cm}^2/\text{Vs}$
Hole mobility	$\mu_h$	$10^{-4}$	$10^{-4}$	$\text{cm}^2/\text{Vs}$
Band gap	$E_g$	1.7	1.7	eV
Thickness	$L$	variable	variable	nm
Effective density of states	$N_C$	$10^{19}$	$10^{19}$	$\text{cm}^{-3}$
-	$N_V$	$10^{19}$	$10^{19}$	$\text{cm}^{-3}$
Relative permittivity	$\epsilon_r$	9.6	9.6	-
Injection barrier	$\phi_{in}$	variable	variable	eV
Extraction barrier	$\phi_{ext}$	variable	variable	eV
Density of Gaussian states	$N_T$	variable	0	$\text{cm}^{-3}$
Gaussian trap level	$E_T$	variable	-	eV
Standard deviation	$\sigma_T$	0.1	-	eV
Density of tail states	$N_t$	variable	0	$\text{cm}^{-3}\text{eV}^{-1}$
Characteristic tail slope	$E_{ch}$	variable	-	eV
Donors	$N_d$	variable	variable	$\text{cm}^{-3}$
Acceptors	$N_a$	variable	0	$\text{cm}^{-3}$
Capture coefficients	$\beta_n^+$	$10^{-12}$	$10^{-12}$	$\text{cm}^3/\text{s}$
-	$\beta_p^0$	$10^{-10}$	$10^{-10}$	$\text{cm}^3/\text{s}$
-	$\beta_p^-$	$10^{-12}$	$10^{-12}$	$\text{cm}^3/\text{s}$
-	$\beta_n^0$	$10^{-10}$	$10^{-10}$	$\text{cm}^3/\text{s}$
Surface recombination velocity	$S$	$10^5$	$10^5$	$\text{cm}/\text{s}$
Series resistance	$R_s$	$10^{-9}$	$10^{-9}$	$\Omega$
Shunt resistance	$R_{sh}$	$10^9$	$10^9$	$\Omega$
Temperature	$T$	300	300	K

### 6.2.1 Intrinsic semiconductor

The underlying physics of intrinsic semiconductors has already been discussed in a previous section. The following section will be focused on drift-diffusion modelling of an intrinsic semiconductor with Ohmic and injection limited contacts.  $J$ - $V$  curves and  $n$ - $V$  curves will be presented to show the physical behaviour of such systems. The results will be compared to the Mott-Gurney law and a resistor.

The band gap of the material is set to 1.7 eV, the effective density of states of both electrons and holes is set to  $10^{19} \text{ cm}^{-3}$ , the electron and hole mobilities are set to  $10^{-4} \text{ cm}^2/\text{Vs}$  and the injection barriers are set to be either Ohmic ( $\phi_{in/ext} = 0.0 \text{ eV}$ ) or with a small injection barrier for both extraction and injection of  $\phi_{in/ext} = 0.1 \text{ eV}$ . The thickness of all modelled devices were set to 100 nm unless in the section on thickness dependence.

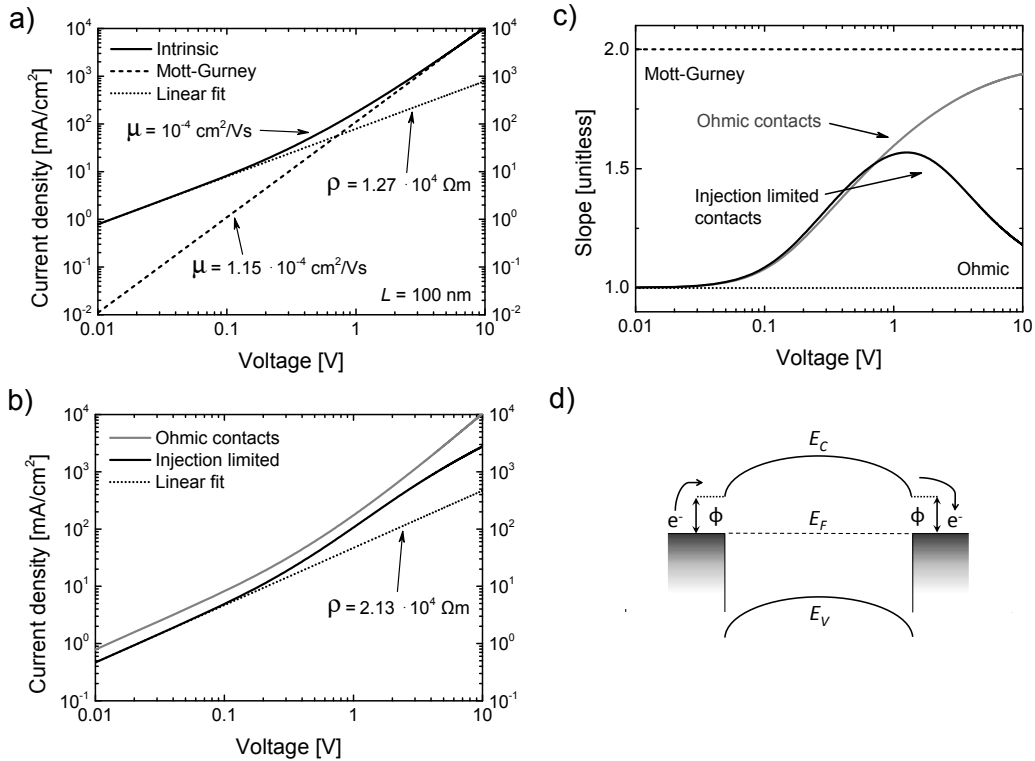


Figure 22: Drift-diffusion simulations: a) Comparison of current density-voltage curves for an intrinsic semiconductor (solid line) with the Mott-Gurney law (dashed line) and Ohm's law (dotted line). b) Drift-diffusion simulation of a device with injection limitation. c) Calculated slopes,  $n$ , of the  $J$ - $V$  curves, where Ohmic current is seen to follow  $n = 1$ , the Mott-Gurney law is seen to follow  $n = 2$ , and the intrinsic semiconductor is seen to go through a transition from  $n = 1$  to  $n > 1$  at low voltages. d) Schematic of energy diagrams of an electron only device, where the Fermi level is shifted away from the conduction band edge due to injection limitation.

In figure 22 the result of a drift-diffusion simulation of a 100 nm intrinsic semiconductor is shown. In a) the solid line represents the intrinsic semiconductor with input parameters given above. The dashed line is the Mott-Gurney law, which was fitted to higher slope region of the intrinsic semiconductor. The dotted line is a fit of Ohm's law to the low voltage region of the current of the intrinsic semiconductor. It is seen that the current density at low voltages follow a linear (Ohmic) dependence. By fitting of Ohm's law to the linear part of the slope, the semiconductor can be considered being a resistor with a resistivity of  $\rho = 1.27 \cdot 10^4 \Omega\text{m}$  (similar to the resistivity of damp wood). It should here be noted that the semiconductor does not explicitly follow Ohm's law in that the linear dependence on thickness of the sample is not fulfilled. The linear region at low voltages is still, however, called Ohmic due to the linear dependence and due to the term being used in the literature.

In figure 22b) an intrinsic semiconductor is modelled in the case of either Ohmic contacts or injection limiting contacts, which has been previously shown to occur in the case where the conduction band of the semiconductor does not coincide with the Fermi level of contact metal. By fitting of Ohm's law to the low voltage regimes of the modelled device with injection limitation, the effect is seen as an increase in the resistivity of the device. From this we can understand injection limitation as adding to the overall resistance of the device, even though the mobility of the semiconductor is not altered. Considering the higher voltage regime, namely around 10 V, it is seen that the shape of the  $J$ - $V$  curve deviates from the case with Ohmic contacts.

In figure 22c) the slopes of the  $J$ - $V$  curves for both the case with Ohmic contacts and injection limiting contacts is shown. The slope of the  $J$ - $V$  curve for the intrinsic semiconductor is represented by the solid lines (with the grey line being for Ohmic contacts and the black line being for injection limiting contacts), the Mott-Gurney law is represented by the dashed line and Ohm's law is represented by the dotted line. It is seen that the intrinsic semiconductor with Ohmic contacts follows a linear relation at low voltages,  $n = 1$ , as was also seen from the fit of Ohm's law to the  $J$ - $V$  curves. As the voltage is increased, the current tends to a higher power law dependence on voltage until almost reaching  $n = 2$  which is the limit for intrinsic semiconductors (Mott-Gurney limit). It is rather remarkable that the estimated value for the electron mobility from the Mott-Gurney law is so close to the electron mobility used as an input parameter for the drift-diffusion simulation, even though the slope of the current for the intrinsic semiconductor has not fully reached the limit at 10 V (hence the fitting of the power law equation is arbitrarily fitted to the current at 10 V). It seems that despite the influence of diffusion currents seen at lower voltages is reasonably profound, the analytical equation based on drift currents only, still yield good results for intrinsic semiconductors. In the case of injection limitation, the slope of the current is seen to tend to lower values above 1 V, making a fit with the Mott-Gurney law even less justifiable. Finally, figure d) is showing a schematic of the electron only device, showing the injection barrier heights between the metals and the conduction band of the semiconductor. The barrier heights are exaggerated deliberately.

### 6.2.2 Built-in potentials

If the work functions of the contact metals are not equal, built-in potentials will arise. The built-in potential is then given as the difference between the metal work functions,  $\psi$ , which is similar to saying that the built-in potential is given by the difference between the injection barriers

$$qV_{bi} = \psi_{ext} - \psi_{in} = \phi_{ext} - \phi_{in}. \quad (27)$$

Built-in potentials will give rise to diffusion limited currents in one bias direction and injection limiting currents in the other bias direction. For this reason, we will call devices with built-in potentials for asymmetric devices and devices with no built-in potentials for symmetric devices, owing to the asymmetry and symmetry around the voltage origin.

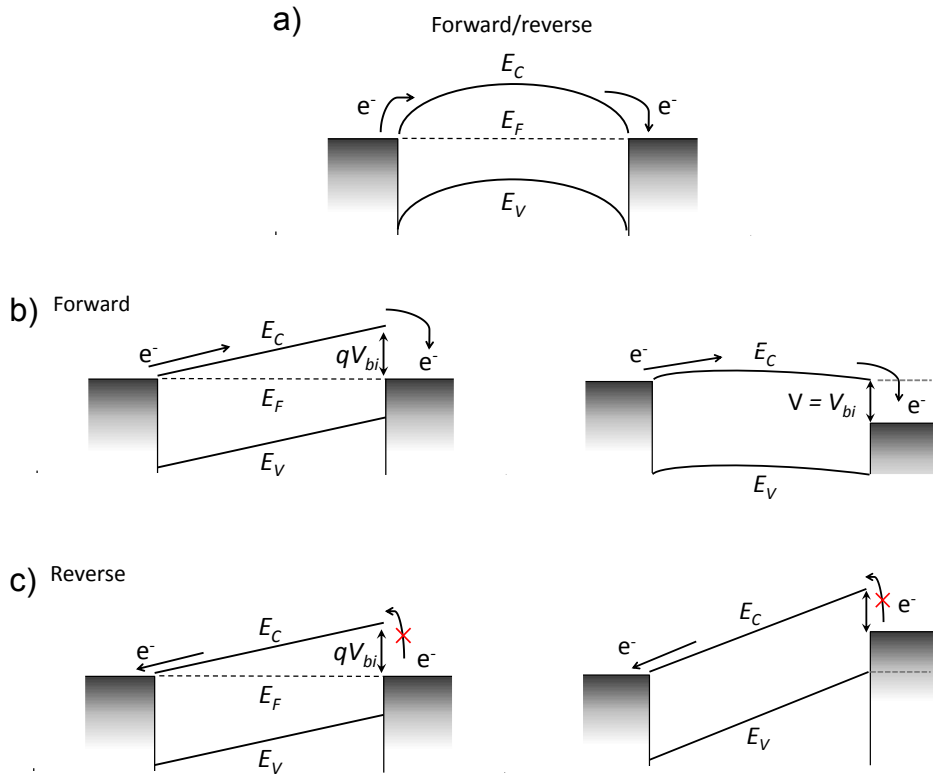


Figure 23: Schematics of the energy level diagram for a) a symmetric electron device, and for the forward b) and reverse c) for an asymmetric electron only device with a built-in potential given by the difference between the metal work functions.

Figure 23a) is showing a schematic of the energy levels for a symmetric device, similar to what was shown in figure 22d), but with Ohmic contacts. Independent of bias voltage polarity, the current output will be the same. Figure 23b) is showing the energy levels of an asymmetric device with a built-in potential of  $qV_{bi}$ . In forward bias, injection is not limited, but the charges

will have to diffuse against the electric field generated by the tilted conduction band before the charge can be collected at the other electrode. As the voltage is increased to roughly  $V = V_{bi}$ , the diffusion barrier is overcome, and the device acts almost as in the case with no built-in potential. Figure 23c) is showing the reverse bias situation of an asymmetric device. Injection is limited by the injection barrier, but as the charge has reached the conduction band, it can easily flow to the counter electrode. As the bias voltage is applied to higher values, charges continue to be injected limited.

The  $J$ - $V$  curves and slope curves of an intrinsic semiconductor with Ohmic contacts and injection limitation was shown in the previous section. Similar curves for an intrinsic semiconductor with a built-in potential of 0.5 eV was calculated. A large difference between the forward and reverse bias currents is observed, which is due to one current direction being heavily limited by the diffusion barrier caused by the large built-in potential and the other current direction being heavily limited by an injection barrier of 0.5 eV.

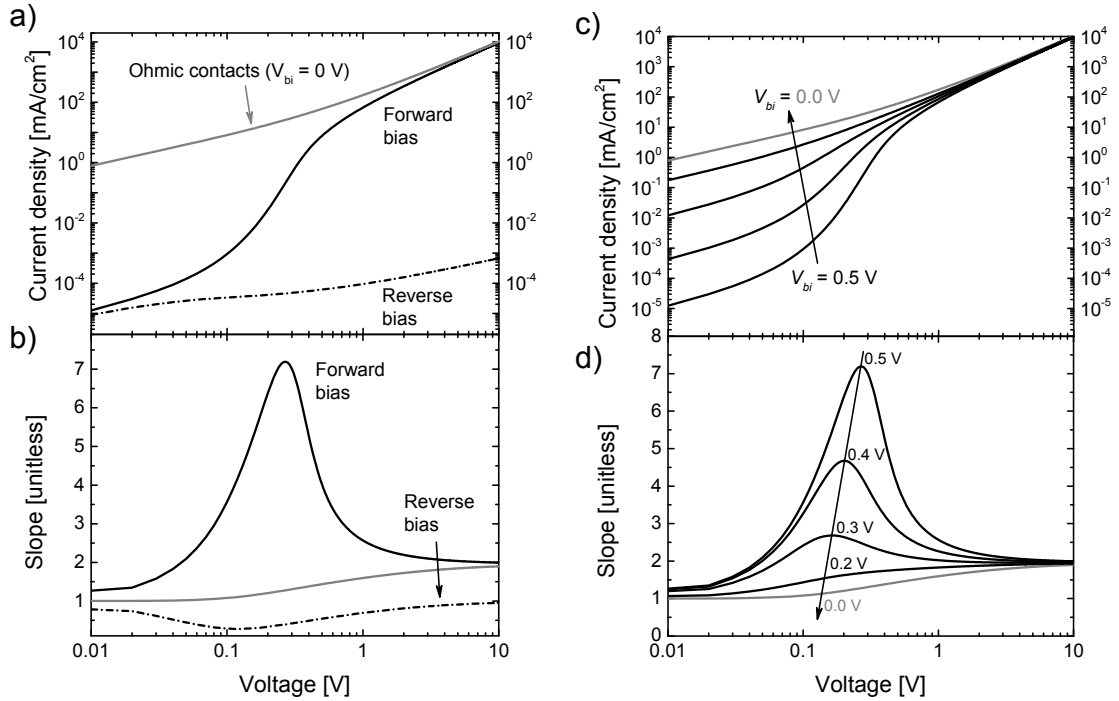


Figure 24: Drift-diffusion simulation: a) Comparison of current density-voltage curves for an intrinsic semiconductor with a built-in potential arising from a differences in work functions of 0.5 eV in forward bias (solid black line), and in reverse bias (dot dashed black line), and an intrinsic semiconductor with Ohmic contacts (solid grey line). b) Slope-voltage curves. c)  $J$ - $V$  curve in forward bias as the built-in voltage is reduced. d) The lowering of the slope of the current density when the built-in voltage is reduced (note that the maximum of the slope shifts to lower voltages).

In figure 24a) the current density is shown for a device with a large built-in potential (which

is compared to a device with zero built-in potential). It is seen that the forward bias current, which is the current which is not injection limited but rather limited by the diffusion barrier set by the built-in potential, is very low up until a point where the diffusion barrier is overcome, as was shown in figure 23b). In the limit of high voltage, the current density approaches that of the intrinsic semiconductor with Ohmic contacts. In the reverse bias situation, which is the case of a large injection limitation, the current is seen to be very low, even at very large voltages, which is due to the very large injection limitation. However, as soon as a charge carrier is injected into the conduction band of the semiconductor, the extra electric field generated by the contacts acts to transport the charge carrier quickly to the opposing contact, giving rise to a peculiar current response.

In figure 24b) the slopes of the  $J$ - $V$  curves are calculated. For the forward bias current it is seen that the slope of the current reaches a very high value ( $n > 7$ ) around the point of overcoming the built-in potential. At higher voltages the slope of the current approaches that of the intrinsic semiconductor with zero built-in potential. The slope of the reverse bias current is seen to be below that of the semiconductor with zero built-in potential for all voltages.

As the built-in potential is decreased from 0.5 V towards 0 V, the current density will approach that of the Ohmic injection case (figure 24c), and the slope of the current will likewise tend towards the ideal case (figure 24d). Furthermore, the peak of the slope of the current will shift towards lower voltages as less voltage is required to overcome the diffusion barrier. Similarly, for the slope of the reverse bias current, the slope will increase towards the case for zero built-in potential.

As will be shown in the next section, knowing the value for the built-in potential is quite important, as the  $J$ - $V$  curves due to the diffusion barrier is similar to the case of deep lying traps. Underestimation of the built-in potential can then give a wrong estimate of the deep trap density of the position of the deep trap level [113, 114].

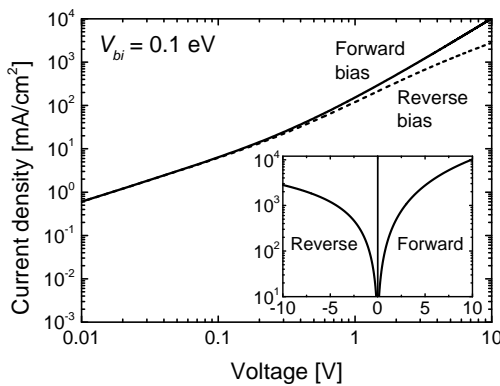


Figure 25: Drift-diffusion simulation of an electron only device with a small built-in voltage of 0.1 V. The graph is showing the current-density on a log-log scale for such a device, with the inset showing the same result on a log-linear scale.

Since the forward and reverse bias current in the presence of a built-in potential are different in both current magnitude and slopes, it is potentially possible to determine the value for the built-in potential by comparing the forward and reserve bias current densities. In figure 24 the forward and reverse bias current was shown for a reasonably large built-in voltage ( $V_{bi} = 0.5$  V). However, even for very low built-in voltages the difference between forward and reverse bias currents can differ by orders of magnitudes.

In figure 25 the difference between forward and reverse bias current for a 100 nm device with a built-in potential of 0.1 eV is shown. The forward and reverse bias currents are quite distinguishable on a log-log scale, but the difference is even more apparent on a log-linear scale (as shown in the inset). For this reason, it is possible to estimate the value for the built-in voltage by comparing the forward and reverse bias current densities. In the case of zero built-in voltage, or at least negligible values, the difference between the forward and reverse bias will likewise be negligible. It is possible to estimate the built-in voltage prior to any measurements simply by considering the work functions of the contact materials used, however, the exact values of these work functions can be difficult to estimate since interface phenomenon between metals and semiconductors can occur and the exact value for the work function can be influenced by crystal direction of the metal as long with any oxidization occurring after contact deposition. The latter case is especially important in the case of a low work function materials such as Ca which quickly oxidises when in contact with oxygen and water. It is therefore important to consider both the forward and reverse bias currents to estimate the built-in potential prior to fitting by the numerical solver [114].

### 6.2.3 Deep Gaussian traps

Impurities or dangling bonds within the semiconductor can give rise to deep states within the band gap, which will act as traps. Traps hinder the flow of charges giving rise to a diffusion barrier which will be observable in the current density-voltage profiles. A trap level can be modelled through a Gaussian distribution of trap states, relative to either the conduction or valence band depending of the type of trap. In the case of the electron traps, which will be considered here, the trap states are relative to the conduction band edge,  $E_C$  (figure 26 d).

Figure 26 is showing the consequences by adding trap states to a 100 electron only device. a) is showing the  $J$ - $V$  curves as the trap density is increased,  $N_T$ , with the trap level positioned in the middle of the band gap ( $E_T = 0.85$  eV with respect to the conduction band edge). It is seen that at low voltages, the current will be heavily hindered, and a small increase in the trap density will give rise to a profound decrease in the current. b) is showing the slopes of the  $J$ - $V$  curves in a), and the profound changes from adding traps is apparent. The current density and slope of an intrinsic device is shown for reference. c) is comparing the case of adding traps to the diffusion barrier introduced from a built-in potential. The similarity of the curves highlights the importance of knowing the built-in potential (if present), as the  $J$ - $V$  could wrongly be interpreted as showing trap states [113]. d) is showing a schematic of the density of

states as a function of energy with a Gaussian trap level at mid gap. Shifting of the trap level towards the conduction band will lower the effect of the trap as the charge carriers can more easily escape.

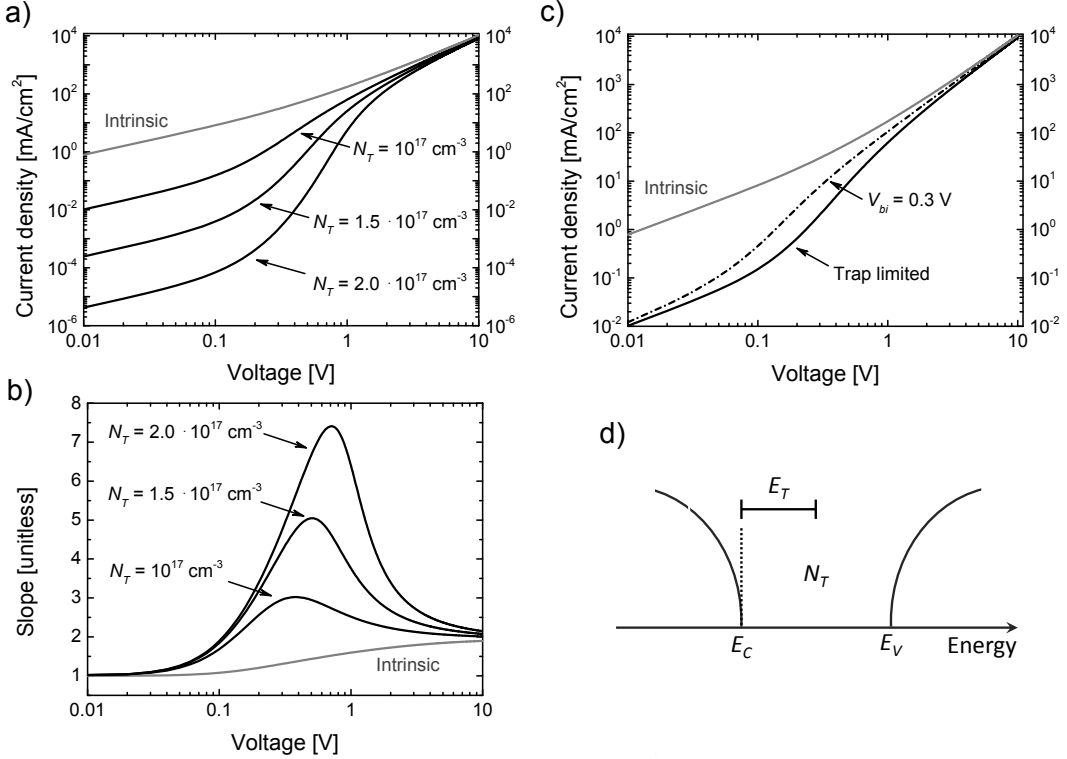


Figure 26: Drift-diffusion simulations. Effect of deep traps; a) simulated  $J$ - $V$  curves of a semiconductor with a trap concentration of  $N_T$  at mid gap, b) simulated  $n$ - $V$  of a), c) comparison of the effect of traps with the effect of a built-in potential, and d) schematic of the density of states as a function of energy. The case of an intrinsic device is inserted for reference.

In the simulation it is seen that the effect on the current density from adding deep trap states is a great lowering, whereas the slope of the current increases significantly from the intrinsic case between 0.1 and 1 V. It is seen that the effect is very similar to the case of the built-in potential, however with the subtle difference that the forward and reverse bias current in the case of traps will be identical (due to the symmetry of the work functions). The traps are distributed uniformly throughout the sample, so the device is said to be symmetric around the voltage origin. In the case of a built-in potential, it was shown that the forward and reverse bias current will differ by orders of magnitude. This highlights the importance of considering both the forward and reverse bias current when doing SCLC measurements, as this will give insight into the origin of diffusion barriers if present.

#### 6.2.4 Shallow exponential traps

Exponential tail states have been shown to be present in a variety of semiconductors. The tail states are also observable in the absorption spectrum for a semiconductor at the onset of absorption. Exponential tail states act as trap sites if the tails are deeper than the thermal energy of the system. The depth of the tails are governed by the characteristic energy,  $E_{ch}$  (figure 27c).

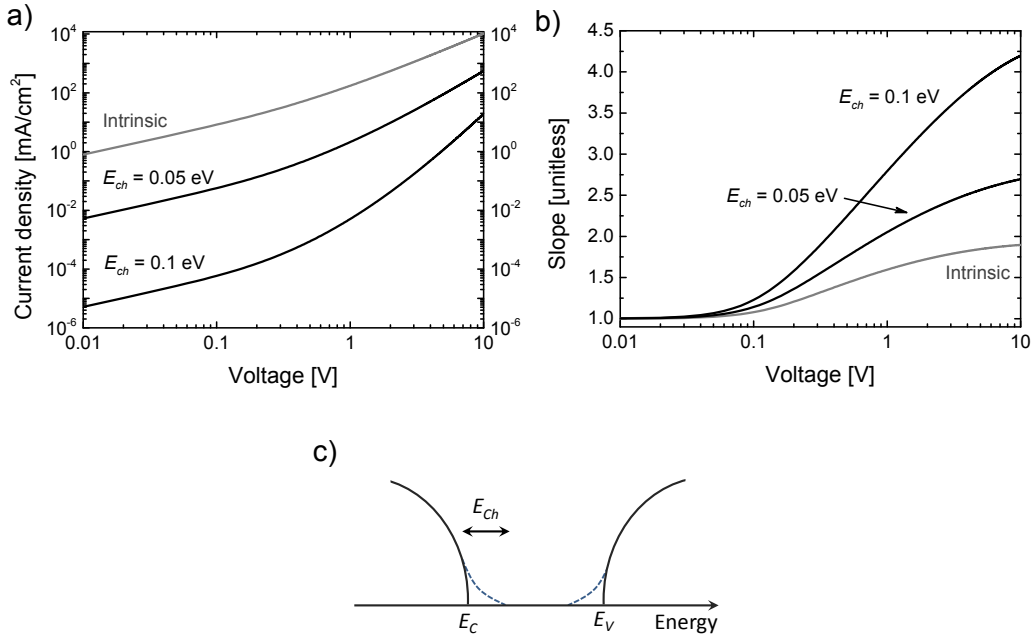


Figure 27: Drift-diffusion simulation of electron only device with exponential tail states in the band gap. a)  $J-V$  with varying characteristic energies, from intrinsic to 0.1 eV. b)  $n-V$ . c) Schematic of the density of states showing the exponential tails extending into the band gap from the carrier bands.

Figure 27 is showing the results of numerical simulations on electron only devices with exponential tail states of varying characteristic energies but a constant concentration of  $10^{19} \text{ cm}^{-3}$ . The characteristic energies were varied in multiples of the thermal energy (2 and 4 times), and the effect on the current density is seen in figure 27a). The current is seen to be reduced significantly due to the electrons being trapped. Figure 27b) is showing the slopes of the current densities in a). It is seen that the slope increases significantly compared to the intrinsic case. A schematic of the density of states with the exponential tails extending into the band gap from the carrier bands in seen in figure 27c).

Contrary to the case of a deep trap level (modelled by a Gaussian distribution), the current is seen not to recover to the intrinsic case when exponential tails are present. Since charge carriers will prefer to occupy and transport through the lowest energy state in the system, the charge carriers will have to escape the tails through thermal emission, greatly inhibiting transport. It

is for that reason common to refer to the estimated mobility as an effective mobility, when using analytical methods. If the tail parameters are known, it is however possible to obtain the true mobility by numerical fitting.

### 6.2.5 Doping

In previous sections it has been shown how the current density and the slope of the current density will change when going from Ohmic injection to injection limitation, from symmetric contacts to built-in potentials, and in the presence of deep and shallow traps. The effect of injection limitation is to lower the current density along with its slope. Built-in potentials and deep traps will lower the current density at low voltages as well as raise the slope significantly at low voltages. The effect of shallow traps is to increase the slope and to decrease the current density. This section will discuss the effect of introduction of doping either in the form of acceptor or donor type dopants.

As has been discussed in a previous section, the effect of adding acceptor type dopants in a semiconductor is to increase the concentration of holes in the device, shifting the Fermi level towards the valence band, and the effect of adding donor type dopants will increase the electron concentration, shifting the Fermi energy towards the conduction band. Considering the case of electrons (since this study will focus on electron transport), adding donor type dopants to the material will then increase the electron conductivity. As the doping concentration becomes increasingly larger, the semiconductor will start to behave more and more as a conductor, with the current density increasing and the slope of the semiconductor decreasing towards  $n = 1$ .

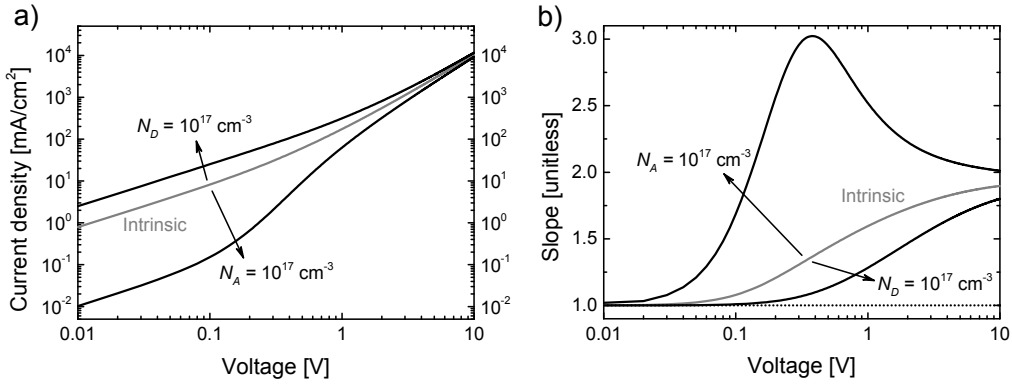


Figure 28: Drift-diffusion simulation of a)  $J$ - $V$  curves of electron-only device with either a large concentration of donor- or acceptor-type dopants. b) Calculated  $n$ - $V$  curves.

In figure 28 the  $J$ - $V$  curves of an intrinsic semiconductor being doped with donor type dopants or acceptor type dopants is shown. It is seen that the current increases significantly when

the donor concentration reaches reasonably high values. Referring back to figure 4, where the Fermi level as a function of doping concentration was calculated, it is apparent that the doping concentration in the semiconductor needs to be significant for an effect on the current density to be seen. With a doping concentration of  $10^{17} \text{ cm}^{-3}$ , the Fermi level is very close to the conduction band, and the material is said to be n-type. A completely analogous effect would be observed for a hole only device with acceptor type dopants introduced to similar concentrations (given that the effective masses for electrons and holes are the same, which is assumed in this case). It is seen that acceptor like dopants act as trap sites for electrons giving rise to a diffusion barrier similar to that observed for deep Gaussian trap states.

Figure 28b) is showing the slope of the current density as dopants are introduced. As the concentration increases the current density was seen to increase, and it can be seen that the slope of the current is tending towards 1 in a drastic fashion. If we consider the effect of adding doping to the semiconductor is to make it act more and more like a metal, up until the point where the semiconductor is degenerate (in which case it does act like a metal), it is expected that the current will increase along with a drop of the slope towards 1. However, at high voltages, an increase in the slope is observed when even with a donor concentration of  $10^{17} \text{ cm}^{-3}$ , indicating that the device is still space-charge-limited when a large amount of charge carriers are introduced at such a voltage. When a large concentration of acceptors is introduced, the slope likewise increases, a trend very similar to the deep trap case.

### 6.2.6 Thickness dependence

Since diffusion barriers are generated due to electric fields, and applying a bias voltage is required to overcome such fields, it is quite apparent that the thickness of the device will have a large influence on all the parameters introduced above. The effect of increasing the thickness will be presented in this section without too much detail. The electric field is given by the voltage divided by the thickness of the sample, meaning that a small voltage in a thin device will give rise to a similar electric field as a large voltage in a thick device. 1 V applied to a sandwich device of 100 nm will give rise to an electric field of  $F = 10 \cdot 10^6 \text{ V/m}$ , which is similar to the field applied using 100 V to a 10 micron device. Especially in the case of traps, which act to trap charges, giving rise to an opposing electric field, will the influence of thickness be very apparent. In the case of built-in potentials, the influence will be less apparent as the diffusion barrier is overcome when a voltage similar to built-in voltage is applied. Since the thickness dependence will differ from types of traps, performing SCLC on a series of devices with different thicknesses will give insight into the nature of the diffusion barriers.

We have seen in the previous sections that the slope function is more interesting to consider in space-charge-limited current measurements, and for that reason, the thickness dependence will be discussed on the basis on slope functions only. The current density will primarily depend on the thickness through  $J \propto 1/L^3$ .

Figure 29 is showing the thickness dependence of the previously mentioned phenomena com-

monly arising in imperfect semiconductor devices, namely injection barriers, deep traps, exponential tails and the effect of doping. The thickness was varied from 25 nm to 150 nm in all cases, in steps of 25 nm. It is seen that the slope will depend heavily on the thickness of the device in all cases. Since such large variations are observed, it is proposed that a thickness series is performed when doing SCLC measurements.

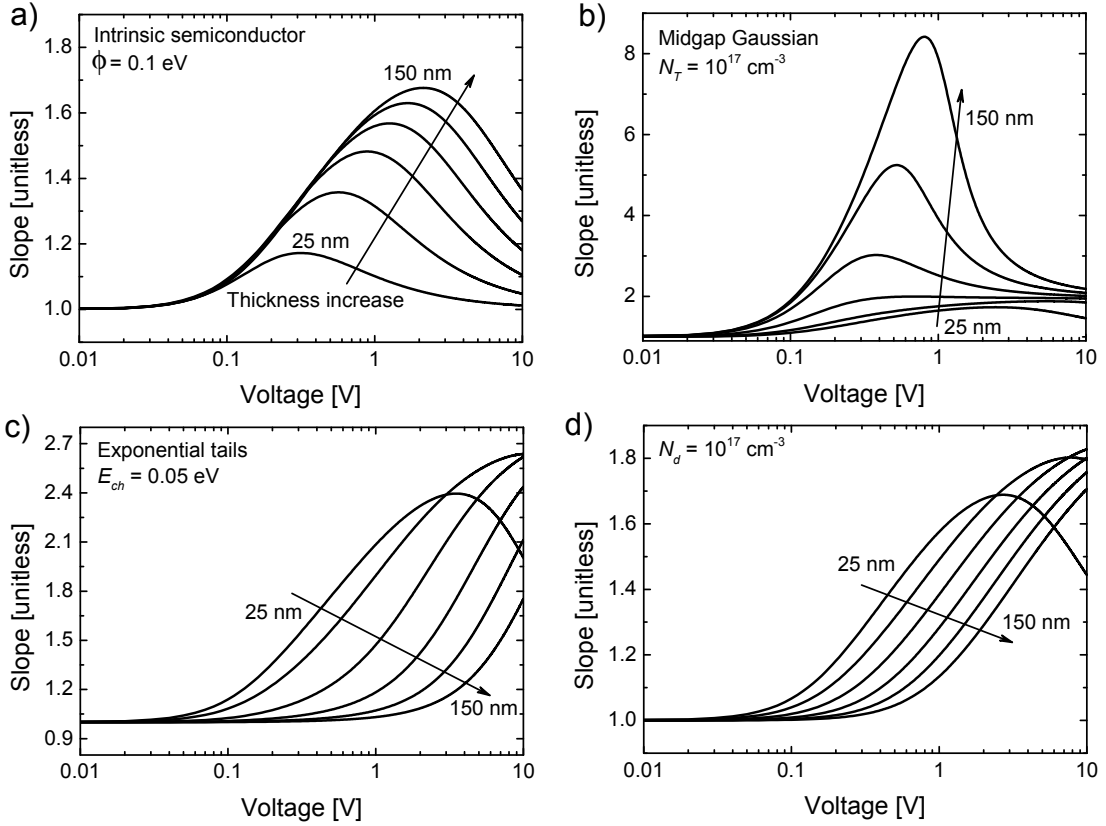


Figure 29: Thickness dependence of the previously discussed parameters; a) intrinsic semiconductor with injection barriers of 0.1 eV, b) deep traps, c) exponential tails, and d) shallow doping. The thickness was varied from 25 nm to 150 nm in all cases, in steps of 25 nm.

In a) it is seen that by increasing the thickness of the device, the slope will change dramatically, with an increase of the maximum of around 1.2 to 1.7. in b) the effect of changing the thickness when a large concentration of deep traps are present is seen to have an incredible large effect. The diffusion barrier generated by deep traps is governed by the electric field arising from trapped charge, and with that electric field increasing with increased thickness, the effect of the traps increases. In c) the effect on exponential tail states is seen to increase the slope and move the maximum to higher voltages, similar to what was observed for deep traps, but different in the sense that the slope does not recover back to the intrinsic case at high voltages. In d) the effect in the case of a large concentration of donors is shown. An increase in thickness can be

seen to move the maximum slope towards higher voltages along with an increase the maximum. It should here be noted that the effect of including a very low shunt resistance (meaning an inclusion of a large number of pinholes in the film) could lead to effects similar to the case of doping, namely an increase in the current and a drop in the slope due to the device becoming increasingly Ohmic. However, since the thickness dependence will differ in the two cases, the effect of shunts can be ruled out as soon as thickness data of the films are obtained. Even though an image of the cross section of the thin films could not be obtained, the films were still investigated during the SEM calibration, and no clear evidence of non-uniformity or pinholes was present.

### 6.3 SCLC experimental results

To the date of writing it has not been possible to obtain good cross section SEM images of the single carrier devices. The recipe followed for fabrication of the  $\text{Sb}_2\text{S}_3$  layer has been reported to yield thicknesses of around 100 nm. For that reason, during the numerical fitting, all thicknesses will be set to 100 nm.

#### 6.3.1 Measurements on $\text{Sb}_2\text{S}_3$

Space-charge-limited currents were drawn through devices with ITO/TiO<sub>2</sub>/CdS/ $\text{Sb}_2\text{S}_3$ /Ca/Al architecture. The interlayers, the  $\text{Sb}_2\text{S}_3$  layer, and the Ca/Al contact were deposited as explained in a previous section. The  $\text{Sb}_2\text{S}_3$  layer was decomposed and annealed at 300°C for 10 min in a glove box with inert atmosphere. The resulting current density-voltage profiles of 8 devices from two different samples are shown on a linear scale in figure 30a). The data was plotted on a linear scale instead of a log-log scale in order to better distinguish between the current density-voltage curves for the different devices. A linear fit to the device giving the least current at low voltages is also shown as a dashed line. The linear fit was included to highlight the deviation of the SCLC curves from linear dependence.

Figure 30b) is showing the slope of the current density clearly showing deviation from linear behaviour. The slope of the current is seen to follow unity at low voltages, increasing to a low value of around 1.1 at around 2 V of applied bias, which was independent of bias polarity. The deviation from unity is an indication of space-charge-limitation. From figure 30a) it was also shown that no significant difference in the magnitude of the current is observed between the forward and the reverse bias, which is clearly seen for a single device in figure 30c) (inset is showing corresponding slopes). It was previously shown in the section of modelled devices, that the presence of even a minute built-in potential would give rise to a difference in the current density of almost an order of magnitude at high voltages (figure 25). This is indicating that no built-in potentials are present in the device, e.g., the device is symmetric. Furthermore, in the presence of a built-in potential, the direction of diffusion limitation would have given rise to a

higher slope of the current and a lower value for the current at low voltages, and the direction of injection limitation would have shown linear conduction at higher voltages (which was shown in figure 24). A small difference between the forward and the reverse current slope is however observed in c). This minute difference could however be caused by the polarity of the injection, as one curve was obtained by injection from -5 V to 0, and the other from 0 to 5 V. Finally, figure 30d) is showing a schematic of the energy levels for a symmetric device.

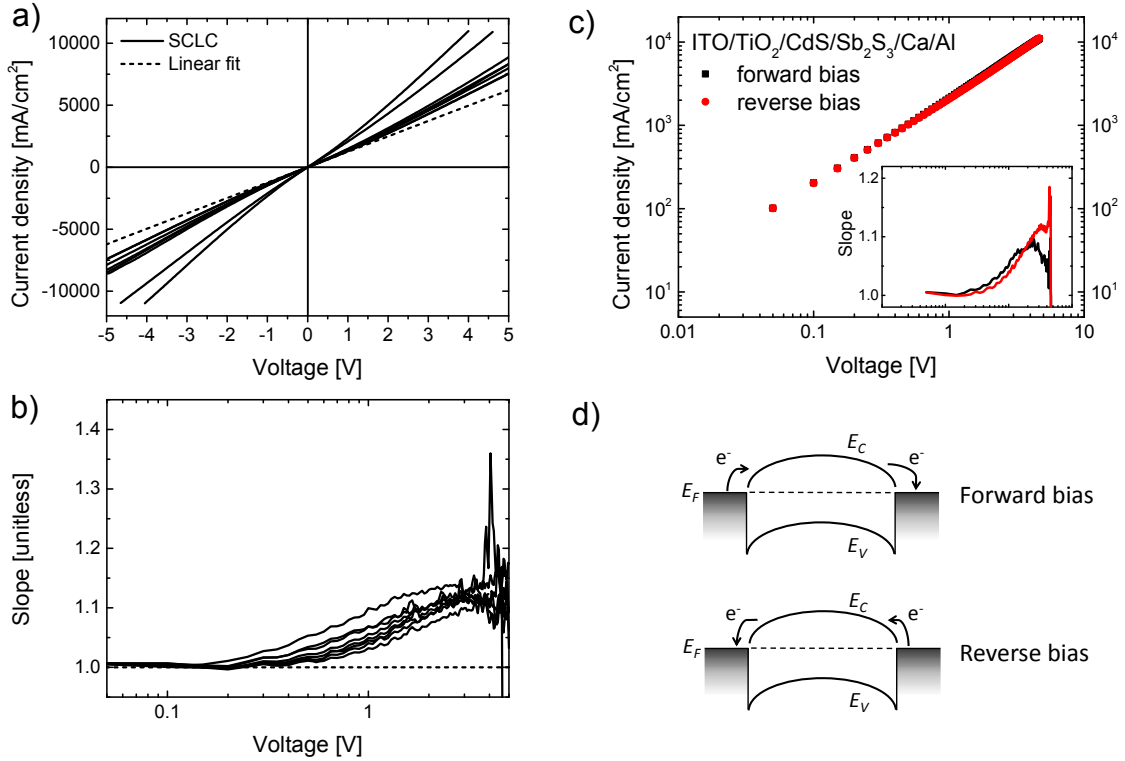


Figure 30: a) Current density-voltage curves of 8 electron ITO/TiO<sub>2</sub>/CdS/Sb<sub>2</sub>S<sub>3</sub>/Ca/Al devices (solid lines). A linear fit to the lowest current device is inserted (dashed line). b) Slope-voltage curves. c) Log-log plot of a single electron only device, showing forward (black) and reverse bias current (red), with the slope shown in the inset. d) Schematic showing band diagrams for symmetric electron only device (in this case with ohmic contacts).

### 6.3.2 Contact choice

Due to the symmetry of the curves and the reproducibility of the devices ITO/TiO<sub>2</sub>/CdS and Ca/Al are both considered being good electron injection and extraction contacts for Sb<sub>2</sub>S<sub>3</sub>. CdS is then assumed to be sufficiently n-type such that any injection barrier would be minute if even present, and the thickness of the dense layer is assumed to be sufficient. Similarly, calcium is shown to act as a good electron injection contact. However, in order to test the need for Ca in

the back contact, electron only devices were fabricated using only Al as a contact (figure 31a). Similar results were obtained from SCLC measurements, with high current densities and slopes of the current reaching around 1.1 at approximately 2 V (inset). This indicates that calcium is not needed as the electron injection contact, and the unstable metal can be omitted for these types of devices in the future. Most of the measured devices did however use the Ca/Al back contact, and so, the majority of the results will be shown with that contact.

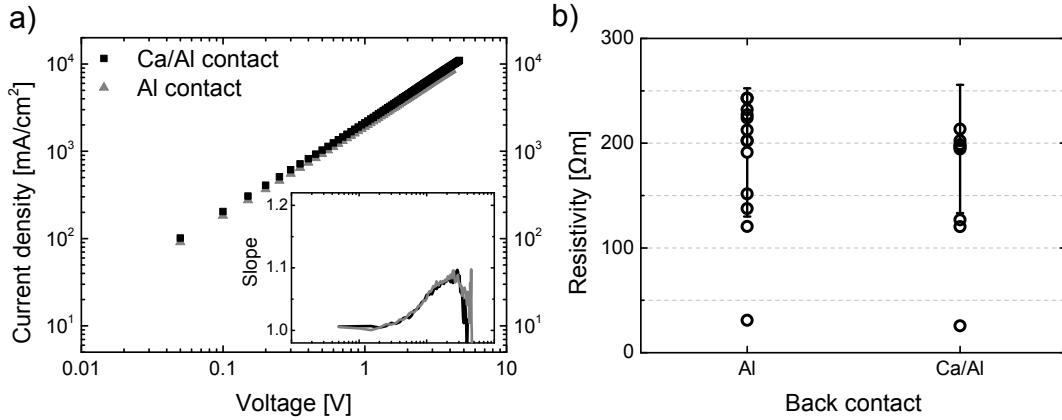


Figure 31: a) SCLC data obtained using either Ca/Al or only Al as a back contact. Similar current density-voltage profiles and slopes profiles were obtained. b) Resistivity of sandwich structures of ITO/TiO<sub>2</sub>/Al and ITO/TiO<sub>2</sub>/Ca/Al. The total thickness of the device with Al is estimated to be 240 nm, and the thickness of the device with Ca/Al is estimated to be 270 nm.

The electrical resistivity of the contacts was measured from devices with ITO/TiO<sub>2</sub>/Al and ITO/TiO<sub>2</sub>/Ca/Al architectures 31b). The resistivity is given in units of Ωcm with an estimated device area of 0.045 cm<sup>2</sup> in both cases, and a thickness of the total device of 250 and 270 nm respectively: (ITO (70 nm), TiO<sub>2</sub> (20 nm), Ca (30 nm) and Al (150 nm)).

Since the thicknesses were not directly measured, the values for the resistivities are estimates, however, by assuming a thickness of 30 nm for the Ca layer, it can be seen from comparing the values, that the difference between using an Al or a Ca/Al contact is not important for device performance, which was also apparent from figure 31a).

In order to ensure that what is really being probed is the Sb<sub>2</sub>S<sub>3</sub> layer (CdS could act as a bottleneck material if the dense layer is not significantly n-type), devices with ITO/TiO<sub>2</sub>/CdS/Ca/Al were measured and compared to devices containing Sb<sub>2</sub>S<sub>3</sub>. The current density as a function of voltage on a linear scale is shown in figure 32. It is clearly seen that the ITO/TiO<sub>2</sub>/CdS/Ca/Al device is showing linear conduction through the origin, e.g., the slope of the current is unity for all voltages, which is evidence of Ohmic conduction. It can for that reason be assumed that the 20 nm dense layer of CdS is sufficiently n-type, and the conduction band edge and Fermi level position is in a good position for the layer to act as an efficient electron injection layer.

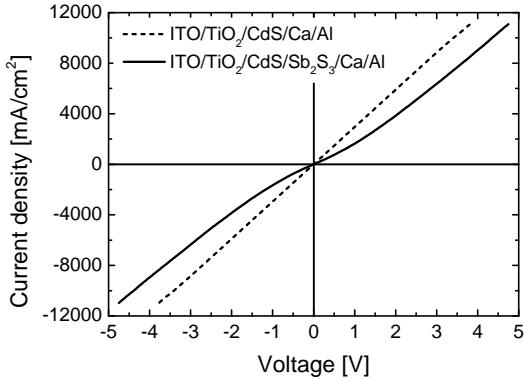


Figure 32: Linear plot of space-charge-limited current as a function of voltage for an ITO/TiO<sub>2</sub>/CdS/Sb<sub>2</sub>S<sub>3</sub>/Ca/Al electron only device compared to similar device not containing Sb<sub>2</sub>S<sub>3</sub>. The black line represent the space-charge-limited current of the Sb<sub>2</sub>S<sub>3</sub> device, and the dashed line is showing Ohmic conduction for the device without Sb<sub>2</sub>S<sub>3</sub>.

### 6.3.3 Numerical fitting

A series of SCLC data was shown in figure 30a), where both the forward and reverse bias current density was shown. It is apparent from the dashed line showing a linear tendency and from figure 30b), that the power law dependency for the current density is not linear at higher voltages, which is an indication of space-charge limitation. Comparing the forward and reverse bias current densities (figure 30c) it is seen that the built-in potential is zero, indicating that the injection and extraction barrier heights are of a similar magnitude ( $\phi_{in} = \phi_{ext}$ ). From device modelling it was shown that trap states tend to decrease the current density and increase the slope of the current density significantly at low voltages beyond what is seen for intrinsic semiconductors. Built-in potentials, the presence of which are already ruled out, will have a similar effect on the current and the slope. Since an increase of the slope from the intrinsic case is clearly not seen, it must be assumed that the presence of traps can not be seen from the data, even though it is very likely that traps are present, in which case the density might be small. The magnitude of the current density is high (compared to the modelled case of an intrinsic semiconductor with a mobility of  $\mu_e = 10^4 \text{ cm}^2/\text{Vs}$ ), which could indicate either that the mobility is higher, or that donor type dopants are present. It was shown that the presence of donor type dopants in an electron only device will increase the current and lower the slope towards linear behaviour. Finally, it was shown that injection limitation will lower the current due and lower the slope. Since the thickness of the devices could not be precisely measured (due to the lack of success with cross section SEM), the thickness was assumed to be 100 nm, in accordance with previous studies using the same device architecture, recipe and laboratory facilities. By allowing the drift-diffusion model to vary these three parameters, namely the electron mobility, the barrier heights and the donor concentration, good fits to the presented

data is possible.

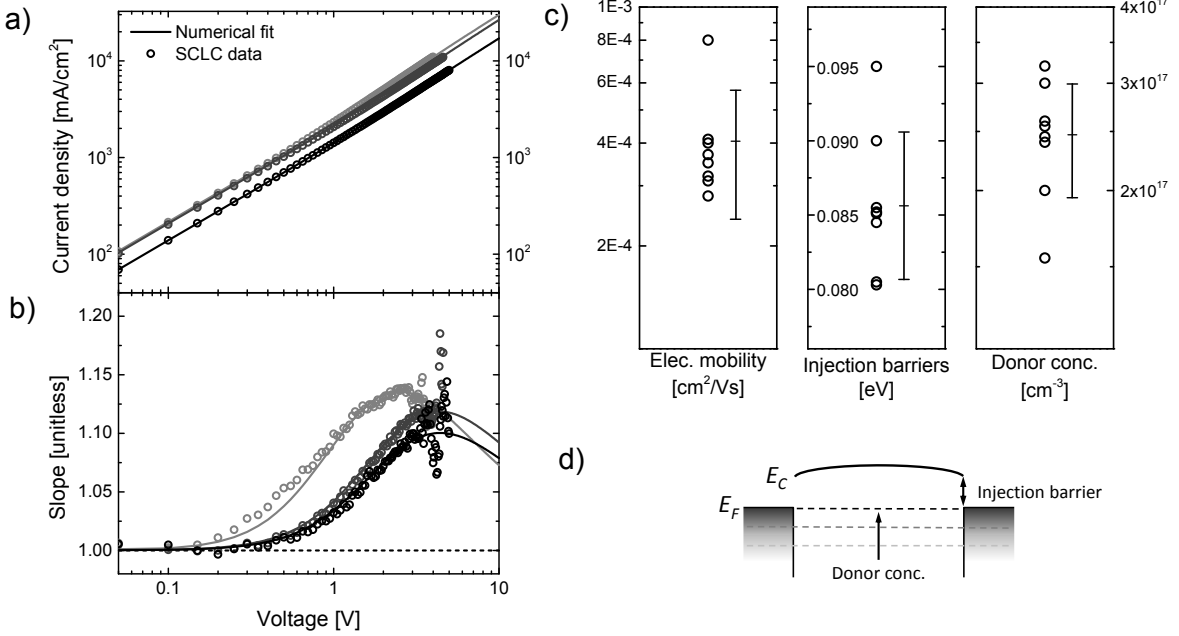


Figure 33: Numerical fits to three arbitrarily chosen sets of SCLC data. a) The mobilities was estimated by fitting to the current density-voltage curves, and b) the donor concentrations and barrier heights were estimated by the slopes of the current densities. c) Resulting values for the fitting parameters. The values are represented by black circles where the average values and the standard deviation is represented by the error bars. d) Schematic of energy levels.

Figure 33a) and b) is showing the numerical fits to three arbitrarily chosen data sets in the series of measurements shown in figure 30. Figure 33a) is showing the fit to the current densities for the three devices and figure 33b) is showing the fits to the slopes of current densities. The fitting procedure was as follows: since the value for the mobility only has the effect as to change the magnitude of the current density, the only two parameters allowed to fit to the curves, initially, was the injection heights and the donor concentration. It was previously shown that the slope function will be affected differently by these two parameters, where the maximum of the function will tend to the left on the voltage axis as the barrier heights are increased, and tend to the right when the donor concentration is increased. Increasing either parameters tends to lower the slope. For this reason, it was possible to obtain a good fit for the slope, where after the mobility was varied in order to obtain the right magnitude for the current density. Good fits were seen in all three cases (as was the case for all data).

The obtained device parameters are shown in figure 33c). The obtained values for each  $J$ - $V$  curve is seen as black circles, where the average value and the standard deviation is shown next to the obtained parameter values. The average value for the electron mobility was found to be  $4.05 \cdot 10^{-4}$  cm<sup>2</sup>/Vs, with average barrier heights of 0.086 eV, and a reasonably large donor

concentration of  $2.47 \cdot 10^{17} \text{ cm}^{-3}$ . From these values it is seen that the material is showing a low mobility compared to bulk materials which could be expected from a disordered material, that good injection from the chosen contacts can be obtained and that the material is highly n-type. The observed mobility is however large compared to the mobilities observed in other disordered systems, indicating that this material is showing good promise for solution processed electrical applications. The low barrier heights, which would be termed as Ohmic, indicates that the injection from the ITO/TiO<sub>2</sub>/CdS and Ca/Al contacts is good. Such contacts could then be used for field-effect transistor devices or light emitting diode devices. Since injection from a contact is more difficult than extraction, such contacts are also suitable for solar cell applications. With the material being highly n-type, a combination of a suitable p-type material could yield a p-n junction, and with the good electron mobility, efficient devices could be envisioned. The large standard deviation of the device parameters is a clear indication that better control of the film is needed in order to achieve more efficient and more reproducible devices. Several solar cells using this material decomposed from a xanthate precursor have been reported, however with limited efficiencies. Even though all films were decomposed in a glove box, the solutions were deposited in ambient atmosphere, allowing the sample to be exposed to both water, oxygen and other contaminants. It is to this day unknown whether ambient atmosphere is detrimental or beneficial for the devices. Better control of device fabrication might be paramount for device performance, whether that is controlled humidity levels, full fabrication in inert atmosphere or nano-scale control of the crystals.

#### 6.3.4 Annealing dependence on mobility and doping

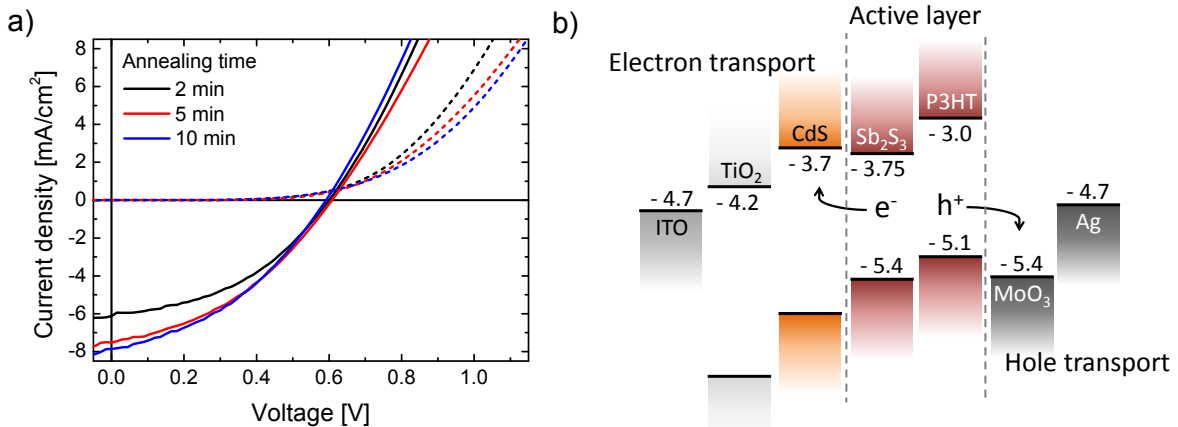


Figure 34: a)  $J$ - $V$  curves of champion devices of bi-layer solar cells with ITO/TiO<sub>2</sub>/CdS/Sb<sub>2</sub>S<sub>3</sub>/P3HT/MoO<sub>3</sub>/Ag device structure, where the Sb<sub>2</sub>S<sub>3</sub> was annealed at different times (2, 5, 10 min). b) Device architecture of the studied bi-layer solar cells.

Bilayer solar cells made by using an interface of Sb<sub>2</sub>S<sub>3</sub> and P3HT were fabricated, using

ITO/TiO<sub>2</sub>/CdS as the front contact and MoO<sub>3</sub>/Ag as the back contact. The layers were deposited according to the recipes discussed in previous sections. In order to achieve efficient devices, the thin film of P3HT was deposited following the recipe of Flannan *et al.* In the work by Flannan *et al.*, it was shown that the annealing time of the Sb<sub>2</sub>S<sub>3</sub> layers was detrimental for the open-circuit voltage. It should be noted that the batch of antimony xanthate used in this study is different than previously used. The xanthate was however made following the same recipe, but device parameters might vary compared to previously published results for this reason.

Figure 34a) is showing *J-V* curves of Sb<sub>2</sub>S<sub>3</sub>/P3HT champion bilayer solar cells in the dark (dashed lines) and under one sun illumination (solid lines). A small decrease in the open-circuit voltage is observed as the annealing time is increased from 2 to 10 min. It is however seen that the short circuit current density increases with annealing time from around  $-6 \text{ mA/cm}^2$  to around  $-8 \text{ mA/cm}^2$ . The device architecture of the solar studied solar cells is shown in figure 34b).

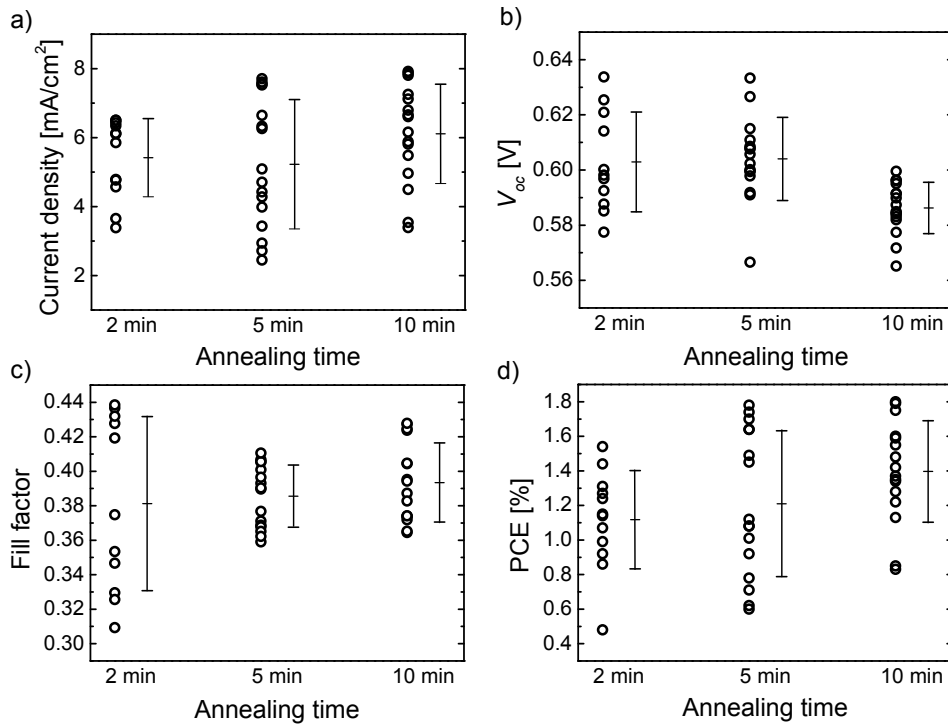


Figure 35: Measured device parameters for P3HT/Sb<sub>2</sub>S<sub>3</sub> bilayer solar cells under 1 sun illumination: a) the short circuit current density, b) open circuit voltage, c) the fill factor, and d) the power conversion efficiency. All parameters are shown for 2, 5 and 10 min. annealing time.

In figure 35 the device parameters for the bilayer cells are shown as a function of annealing time. Similarly to what was observed for the champion devices, the short circuit current density, the fill factor and the power conversion efficiency increases with increased annealing time. A drop

in the open circuit voltage is seen as the device is annealed for 10 min. It should be noted that the average value for the open circuit voltage increased slightly at 5 min annealing time compared to 2 min, but the effect is minute. A commonly accepted theory for the value of the open circuit voltage for hybrid devices is not known to the author. The open circuit voltage in a p-n junction is governed by the difference in Fermi levels of the n- and p-type material [2]. In a polymer:fullerene bulk heterojunction solar cell, the open circuit voltage is governed by the difference between the LUMO of the acceptor and the HOMO of the donor corrected by an offset due to recombination and the presence of a charge transfer state at the interface [116]. Three mechanisms for the observed reduction in the open circuit voltage as a function of annealing time is proposed, namely an increase in crystallinity, a decrease in doping concentration of the acceptor ( $\text{Sb}_2\text{S}_3$ ) or a reduced lifetime of the exciton due to recombination. It was already shown from UV-vis and XRD in a previous section that the annealing time did not have a significant effect on the crystallinity (once the crystalline material is formed, changing the properties of these might require very high temperatures). However, an increase in the mobility, which could be measured by SCLC, as the annealing time is increased could indicate a very small increase in crystallinity. In order to try and determine the cause for the reduction in the open-circuit voltage, SCLC measurements on  $\text{Sb}_2\text{S}_3$  electron-only devices were performed where the  $\text{Sb}_2\text{S}_3$  was decomposed at 300°C at three different annealing times (2, 5 and 10 min) similar to the case of the solar cells.

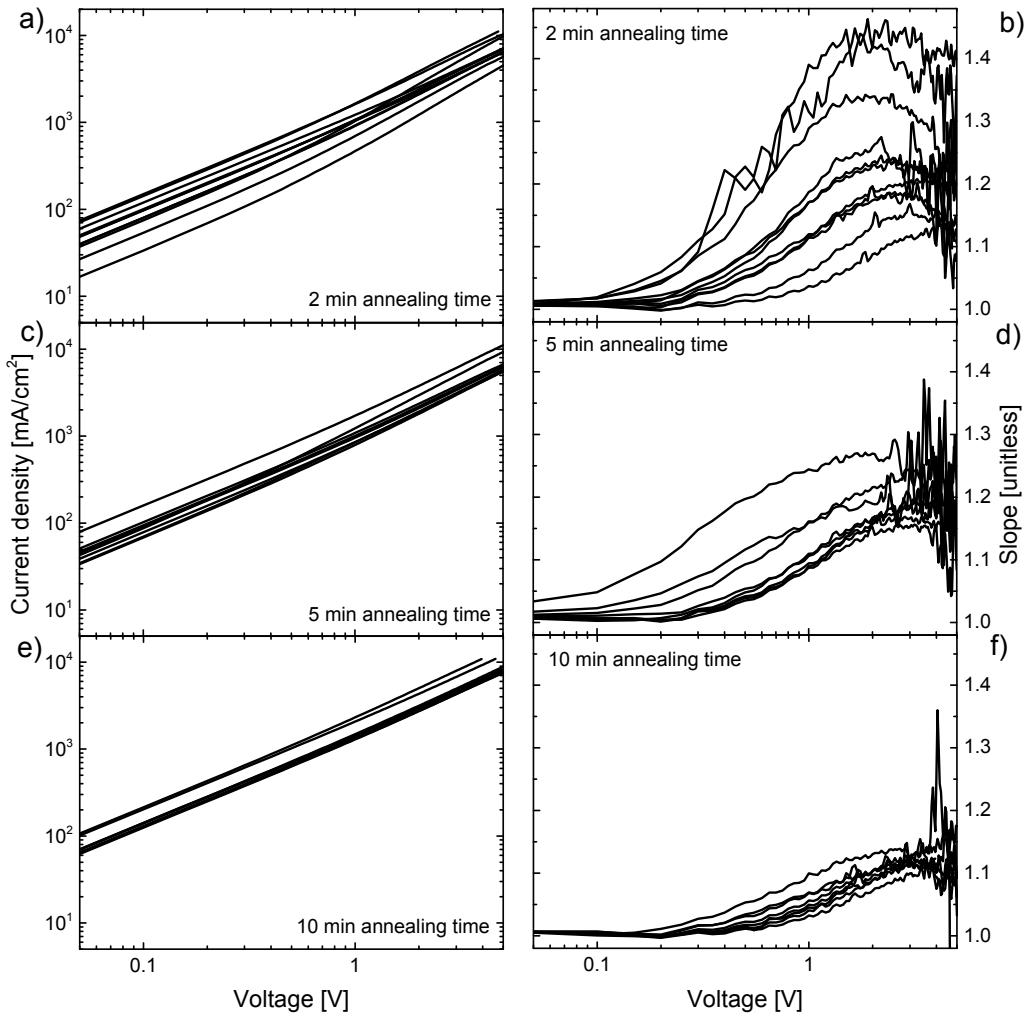


Figure 36: The effect of annealing time on SCLC current densities for  $\text{SB}_2\text{S}_3$  electron-only devices; a) 2 min, c) 5 min and e) 10 min annealing time, and on the slope; b) 2 min, d) 5 min and f) 10 min. All devices were fabricated in inert atmosphere, measured the same way and measured on the same day in a random order.

Figure 36 is showing the current density and the slope of the current density as a function of the voltage with increasing annealing time for a large number of devices. At 2 min annealing time the current is less reproducible, with a large spread in the magnitudes of the current with a generally lower value. Similarly, a very large spread of the value of the slope is seen, with the maximum reaching almost 1.45. As the annealing time is increased to 5 min, the spread of the current and the slope is lowered, with the lowest spread at 10 min of annealing time.

Figure 37 is showing the numerical fits to arbitrarily chosen data from the full range shown in figure 36 (all device data was fitted, but is not shown). Good fits were realised to both the current density-voltage profiles and the slope-voltage profiles. By fitting of the slope with the numerical solver, allowing only the barrier heights and the donor concentration to vary, good

fit to all the data was obtained. By subsequently allowing the mobility to vary, good fits to the current densities were obtained. The fitted parameters are shown in figure 38. It is seen that the electron mobility does not seem to vary significantly with increased annealing time, indicating that no profound increase in the crystallinity of the material is achieved, which was already expected from UV-vis and XRD measurements. Furthermore, the reasonably similar value for the mobility is also a good indication that the density and/or the nature of traps (if present) does not change with annealing time. It is seen that the injection barrier is lowered with increased annealing time along with an increase in the doping concentration. As the doping concentration is increased, the Fermi level will be shifted slightly towards the conduction band. This could help to facilitate charge injection, by lowering the injection barrier to the semiconductor from the metal.

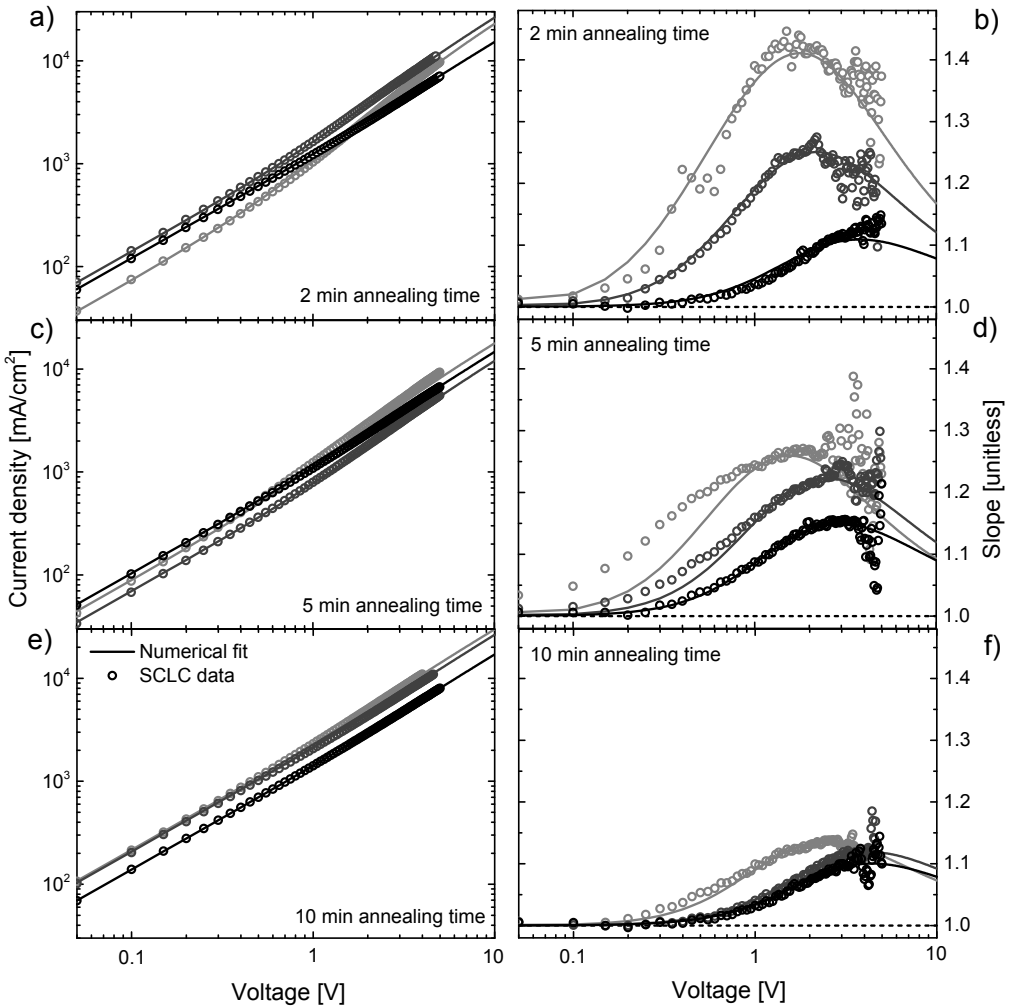


Figure 37: Numerical fits to arbitrarily chosen SCLC data for devices with  $\text{Sb}_2\text{S}_3$  annealed at different temperatures: a)  $J$ - $V$  (2 min), b)  $n$ - $V$  (2 min), c)  $J$ - $V$  (5 min), d)  $n$ - $V$  (5 min), e)  $J$ - $V$  (10 min) and f)  $n$ - $V$  (10 min). The thickness was assumed to be 100 nm in all cases.

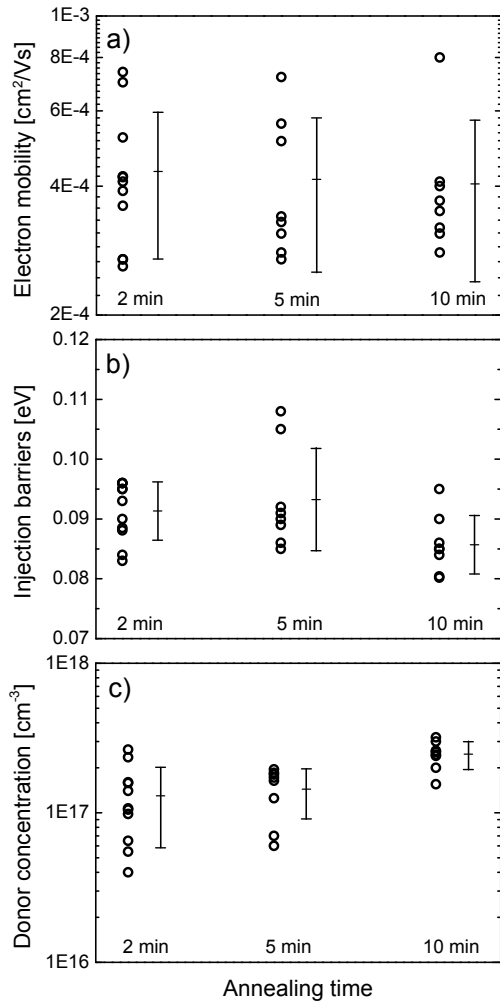


Figure 38: Numerical fitting results: a) Electron mobility, b) injection barriers and c) donor concentration. All values were obtained from fitting to data seen in figure 36.

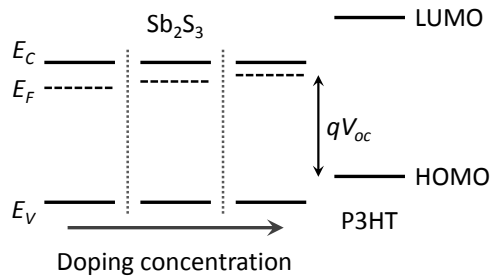


Figure 39: Schematic of proposed effect of increased doping concentration in  $\text{Sb}_2\text{S}_3$  for a hybrid device with a P3HT donor.

If it is assumed that the open circuit voltage in a hybrid device is governed by both the Fermi level of the inorganic acceptor and the HOMO level of the organic donor, then we could expect

an increase in the open circuit voltage as the doping concentration of the acceptor is increased (figure 39). This is however not observed for the hybrid devices shown in this study. An alternative explanation could be that the lifetime of the excitons at the interface is reduced due to an increase of recombination centres (trap states). An increase in recombination would give rise to a lower open circuit voltage in organic solar cells, so if the open circuit voltage is governed primarily by the organic donor, this could be an explanation. It should here be noted that the evidence of trap states are not apparent from the SCLC data, but this could be due to a very low concentration.

It is apparent from comparing the results for the solar cells presented in this study and the results for the single carrier devices fabricated under similar conditions, that no conclusion can be made regarding the effect of the annealing time. Measurements probing exciton lifetimes and measurements further investigating the doping in the polycrystalline  $\text{Sb}_2\text{S}_3$  must be made. The effect of annealing time on the SCLC measurements is however quite apparent, and the values for the doping concentration are seen to increase as the annealing time is increased from 2 to 10 minutes. A further investigation into the materials science, especially by using a combination of XPS, UPS and Kelvin Probe to determine the origin of the doping and the energy levels of the device would yield important information. If the doping concentration is seen to be controlled partly simply by the annealing time, this could be a step closer to achieving an all-solution processed all-inorganic solar cell which could be fabricated at low temperatures without the use of hazardous solvents and toxic device materials.

## 7 Conclusion

In conclusion, space-charge-limited current (SCLC) measurements were realised on thin films of solution processed Antimony sulphide deposited from a precursor. The electron mobility was determined to be  $4.05 \cdot 10^{-4} \text{ cm}^2/\text{Vs}$ , indicating that this material processing route can yield poly-crystalline thin films with high electron mobilities. It was shown that ITO/TiO<sub>2</sub>/CdS and Ca/Al showed good Ohmic contact to Antimony sulphide, and that no built-in potential arose the device is observed as a consequence of using such contacts.

Drift-diffusion simulations showed that the effect of adding donor type doping to an electron only device had a tendency to increase the current density, making the device act increasingly like a conductor. It was shown that the inclusion of traps had the opposite effect, adding diffusion barriers to oppose charge flow. It was however also mentioned that the inclusion of a low sheet resistance can give rise to changes in the *J-V* curves similar to what is observed for doping, emphasizing that control of film quality during processing is highly important. Thickness dependent SCLC can help to determine the nature of the current-voltage curves. A novel approach using a numerical solver was used to determine the nature and concentration of ionized dopants, showing that the solution-processed Antimony sulphide thin film is highly n-type. The slope of the current density-voltage profile on a log-log scale was used for fitting when the donor concentration was allowed to vary. The charge carrier mobility was allowed to vary to fit to the current density-voltage curves. The donor concentration was determined to be  $2.47 \cdot 10^{17} \text{ cm}^{-3}$ .

Hybrid solar cells of P3HT/Sb<sub>2</sub>S<sub>3</sub> were compared to SCLC data obtained for Sb<sub>2</sub>S<sub>3</sub> electron only devices where the annealing time of the inorganic phase was varied from 2 to 10 min for type of devices. An increase in the donor concentration was observed from the SCLC measurements along with a decrease in the open-circuit voltage in the solar cells. Comparing these results to the optical analysis of the thin films, no direct link between the increase in the doping concentration and the reduction in open circuit voltage can be made. It was however observed that the doping concentration increased slightly with annealing time, allowing for a way to tune the Fermi level in the semiconductor by simply varying the annealing time.

## 8 Outlook and future work

From the drift-diffusion modelling it was shown that the thickness of the device will influence both the current and slope of the current to a large extent. All the presented work assumed a constant thickness for all the devices, but if a more precise estimate for the thickness can be obtained either through cross section imaging using scanning electron microscopy or using ellipsometry are more precise estimate of both the charge carrier mobilities and doping concentrations can be made.

Comparing the obtained results with complementary charge carrier mobility techniques such as time of flight and mobilities obtained from field effect transistor devices is important. Future work on this has been planned out and will commence within the next following weeks. It was shown that the thick devices, which would be employed for time of flight measurements were very porous. Optimizing the structure of such films is important to obtain reliable results which can be compared to the thinner denser films. Performing space-charge-limited current measurements on hole only devices is also important, as the donor concentration should give rise to deep trap states for holes, and such could be probed.

Complementary techniques to obtain information about the doping in the films must also be used. Capacitance techniques have shown to yield reliable results for doping in thin films. Employing this technique side by side with SCLC would be both novel and yield interesting results. XPS could potentially yield information about the origin on doping in the films by looking into the chemical stoichiometry.

Techniques to determine the energy levels of the device, more precisely the position of the conduction band edge and Fermi level as a function of processing, could be utilized to help determine the degree of doping in the film. Techniques such as UPS and Kelvin Probe measurements could prove useful.

Techniques to understand what is determining the open circuit voltage in the presented hybrid bi-layer devices must be employed in order to understand why the open circuit voltage drops with annealing temperature and how this is related to the Fermi level in the inorganic phase. The possibility of the degree of crystallinity was investigated in this work, but could not yield conclusive results. The annealing time effect on carrier lifetimes (recombination) could potentially yield useful information. Techniques such as photoluminescent spectroscopy and electroluminescent spectroscopy could prove useful.

## References

- [1] Lidia Lakusiak and Andrzej Jakubowski. History of semiconductors. *Journal of Telecommunications and Information Technology*, 1:3–9, 2010.
- [2] J. Nelson. *The Physics of Solar Cells*. Imperial College Press, 1st edition, 2003.
- [3] W. Smith. Effect of light on selenium during the passage of an electric current. *Nature*, 7:303–303, 1873.
- [4] D. Chapin, C. Fuller, and G. Pearson. A new silicon p-n junction photocell for converting solar radiation into electrical power. *Journal of Applied Physics*, 25:676–677, 1954.
- [5] N. W. Ashcroft and N. D. Mermin. *Solid State Physics*. Brooks/Cole, 1st edition, 1976.
- [6] B. O'Regan and M. Grätzel. A low-cost, high-efficiency solar cell based on dye-sensitized colloidal  $\text{TiO}_2$  films. *Nature*, 353:737–740, 1991.
- [7] M. Grätzel. Dye-sensitized solar cells. *Journal of Photochemistry and Photobiology C: Photochemistry Reviews*, 4:145–153, 2003.
- [8] A. Yella, H.-W. Lee, H. N. Tsao, C. Yi, A. K. Chandiran, M. Nazeeruddin, E. W.-G. Diau, C.-Y. Yeh, S. M. Zakeeruddin, and M. Grätzel. Porphyrin-sensitized solar cells with cobalt (ii/iii)-based redox electrolyte exceed 12 percent efficiency. *Science*, 334:629–635, 2011.
- [9] C. Chiang, C. Fincher Jr., Y. Park, A. J. Heeger, H. Shirakawa, S. C. Louis, E. J. nad Gau, and A. G. MacDiarmid. Electrical Conductivity in Doped Polyacetylene. *Phys. Rev. Lett.*, 37:1098–1101, 1977.
- [10] W. P. Su, J. R. Schrieffer, and A. J. Heeger. Solitons in Polyacetylene. *Physical Review Letters*, 42:1698–1701, 1979.
- [11] [http://www.nobelprize.org/nobel\\_prizes/chemistry/laureates/2000/](http://www.nobelprize.org/nobel_prizes/chemistry/laureates/2000/). Accessed: 2014-08-27.
- [12] A. Szent-Gyorgyi. Internal Photo-Electric Effect and Band Spectra in Proteins. *Nature*, 157:875, 1946.
- [13] D. D. Eley. Phthalocyanines as Semiconductors. *Nature*, 162:819, 1948.
- [14] D. J. Carswell, J. Ferguson, and L. E. Lyons. Photo- and Semi-conductance in Molecular Single Crystals. *Nature*, 173:736, 1954.
- [15] R. G. Kepler. Charge Carrier Production and Mobility of Anthracene. *Physicsl Review*, 119:1226–1229, 1960.

- [16] B. A. Bolto, R. McNeill, and D. E. Weiss. Electronic Conduction in Polymers: III. Electronic Properties of Polypyrrole. *Australian Journal of Chemistry*, 16:1090–1103, 1963.
- [17] C. W. Tang. Two-Layer Organic Photovoltaic Cell. *Applied Physics Letters*, 48:183, 1986.
- [18] J. J. M. Halls, K. Pichler, R. H. Friend, S. C. Moratti, and A. B. Holmes. Exciton Diffusion and Dissociation in a Poly(p-phenylenevinylene)/C<sub>60</sub> Heterojunction Photovoltaic Cell. *Applied Physics Letters*, 68:3120, 1996.
- [19] N. S. Sariciftci, L. Smilowitz, A. J. Heeger, and F. Wudl. Photoinduced Electron Transfer from a Conducting Polymer to a Buckminsterfullerene. *Science*, 258:1474–1476, 1992.
- [20] N. S. Sariciftci, D. Braun, C. Zhang, V. I. Srdanov, A. J. Heeger, G. Stucky, and F. Wudl. Semiconducting polymer-buckminsterfullerene heterojunctions: Diodes, photodiodes, and photovoltaic cells. *Applied Physics Letters*, 62:585, 1993.
- [21] J. C. Hummelen, B. W. Knight, F. LePeq, and F. Wudl. Preparation and Characterization of Fulleroid and Methanofullerene Derivatives. *Journal of Organic Chemistry*, 60:532–538, 1995.
- [22] G. Yu, J. Gao, J. C. Hummelen, F. Wudl, and A. J. Heeger. Polymer Photovoltaic Cells: Enhanced Efficiencies via a Network of Internal Donor-Acceptor Heterojunctions. *Science*, 270:1789–1791, 1995.
- [23] J. J. M. Halls, C. A. Walsh, N. C. Greenham, E. A. Marseglia, R. H. Friend, S. C. Moratti, and A. B. Holmes. Efficient Photodiodes from Interpenetrating Polymer Networks. *Nature*, 376:498–500, 1995.
- [24] G. Yu, J. C. Hummelen, and A. J. Heeger. Charge Separation and Photovoltaic Conversion in Polymer Composites with Internal Donor/Acceptor Heterojunctions. *Journal of Applied Physics*, 78:4510, 1995.
- [25] Y. Kim, S. A. Choulis, J. Nelson, D. D. C. Bradley, S. Cook, and J. R. Durrant. Device Annealing Effect in Organic Solar Cells with Blends of Regioregular Poly(3-Hexylthiophene) and Soluble Fullerene. *Applied Physics Letters*, 86:063502(3), 2005.
- [26] G. Li, V. Shrotriya, Y. Yao, and Y. Yang. Investigation of Annealing Effects and Film Thickness Dependence of Polymer Solar Cells based on Poly(3-Hexylthiophene). *Journal of Applied Physics*, 98:043704(5), 2005.
- [27] G. Li, V. Shrotriya, J. Huang, Y. Yao, T. Moriarty, K. Emery, and Y. Yang. High-Efficiency Solution Processable Polymer Photovoltaic Cells by Self-Organization of Polymer Blends. *Nature Materials*, 4:864–868, 2005.
- [28] Y. Kim, S. Cook, S. M. Tuladhar, S. A. Choulis, J. Nelson, J. R. Durrant, D. D. C. Bradley, M. Giles, I. McCulloch, C.-S. Ha, and M. Ree. A Strong Regioregularity Effect in Self-

- Organizing Conjugated Polymer Films and High-Efficiency Polythiophene:Fullerene Solar Cells. *Nature Materials*, 5:197–203, 2006.
- [29] H. Kim, S. Nam, J. Jeong, S. Lee, J. Seo, H. Han, and Y. Kim. Organic Solar Cells Based on Conjugated Polymers: History and Recent Advances. *Korean J. Chem. Eng.*, 31:1095–1104, 2014.
- [30] J. Peet, J. Y. Kim, N. E. Coates, W. L. Ma, D. Moses, A. J. Heeger, and G. C. Bazan. Efficiency Enhancement in Low-Bandgap Polymer Solar Cells by Processing with Alkane Dithiols. *Nature Materials*, 6:497–500, 2007.
- [31] Y. Liang, Z. Xu, J. Xia, S.-T. Tsai, Y. Wu, G. Li, C. Ray, and L. Yu. For the Bright Future - Bulk Heterojunction Polymer Solar Cells with Power Conversion Efficiency of 7.4%. *Advanced Energy Materials*, 22:E135–E138, 2010.
- [32] J. S. Moon, J. Jo, and A. J. Heeger. Nanomorphology of PCDTBT:PC70BM Bulk Heterojunction Solar Cells. *Advanced Energy Materials*, 2:304–308, 2012.
- [33] G. Li, C.-W. Chu, V. Shrotriya, J. Huang, and Y. Yang. Efficient Inverted Polymer Solar Cells. *Applied Physics Letters*, 88:253503(3), 2006.
- [34] J. Y. Kim, K. Lee, N. E. Coates, D. Moses, T.-Q. Nguyen, M. Dante, and A. J. Heeger. Efficient Tandem Polymer Solar Cells Fabricated by All-Solution Processing. *Science*, 317:222–225, 2007.
- [35] J. You, L. Dou, K. Yoshimura, T. Kato, K. Ohya, T. Moriarty, K. Emery, C.-C. Chen, J. Gao, G. Li, and Y. Yang. A Polymer Tandem Solar Cell with 10.6% Power Conversion Efficiency. *Nature Communications*, 4:1–10, 2013.
- [36] [http://www.heliatek.com/wp-content/uploads/2012/09/120427\\_PI\\_Heliatek-world-record-10\\_7-percent-efficiency.pdf](http://www.heliatek.com/wp-content/uploads/2012/09/120427_PI_Heliatek-world-record-10_7-percent-efficiency.pdf). Accessed: 2014-08-27.
- [37] [http://www.mitsubishichem-hd.co.jp/english/csr/feature/pickup\\_01.html](http://www.mitsubishichem-hd.co.jp/english/csr/feature/pickup_01.html). Accessed: 2014-08-27.
- [38] M. M. Lee, J. Teuscher, T. Miyasaka, T. N. Murakami, and H. J. Snaith. Efficient Hybrid Solar Cells Based on Meso-Superstructured Organometal Halide Perovskites. *Science*, 338:643–647, 2012.
- [39] H.-S. Kim, C.-R. Lee, J.-H. Im, K.-B. Lee, T. Moehl, A. Marchiaro, S.-J. Moon, R. Humphry-Baker, J.-H. Yum, J. E. Moser, M. Gratzel, and N.-G. Park. Lead Iodide Perovskite Sensitized All-Solid-State Submicron Thin Film Mesoscopic Solar Cell with Efficiency Exceeding 9%. *Scientific Reports*, 2:1–7, 2012.
- [40] M. Liu, M. B. Johnston, and H. J. Snaith. Efficient Planar Heterojunction Perovskite Solar Cells by Vapour Deposition. *Nature*, 501:395–398, 2013.

- [41] D. B. Mitzi. Solution-Processed Inorganic Semiconductors. *Jour. Mater. Chem.*, 14:2355–2365, 2004.
- [42] N. C. Greenham, X. Peng, and A. P. Alivisatos. Charge Separation and Transport in Conjugated-Polymer/Semiconductor-Nanocrystal Composites Studied by Photoluminescence Quenching and Photoconductivity. *Physicls Review B*, 54:628–637, 1996.
- [43] R. Plass, S. Pelet, J. Krueger, and M. Gratzel. Quantum Dot Sensitization of Organic-Inorganic Hybrid Solar Cells. *J. Phys. Chem. B*, 106:7578–7580, 2002.
- [44] A. J. Nozik. Quantum Dot Solar Cells. *Physica E: Low-dimensional Systems and Nanostructures*, 14:115–120, 2002.
- [45] S. A. McDonald, G. Konstantatos, S. Zhang, P. W. Cyr, E. J. D. Klem, L. Levina, and E. H. Sargent. Solution-processed PbS Quantum Dot Infrared Photodetectors and Photovoltaics. *Nature Materials*, 4:138–142, 2005.
- [46] A. I. Ekimov and A. A. Onushchenko. Quantum Size Effect in Three-Dimensional Microscopic Semiconductor Crystals. *ZhETF Pisma Redaktsiiu*, 34:363, 1981.
- [47] R. Rossetti, S. Nakahara, and L. E. Brus. Quantum Size Effects in the Redox Potentials, Resonance Raman Spectra, and Electronic Spectra of CdS Crystallites in Aqueous Solution. *The Journal of Chemical Physics*, 79:1086–1088, 1983.
- [48] L. E. Brus. Electron-Electron and Electron-Hole Interactions in Small Semiconductor Crystallites: The Size Dependence of the Lowest Excited Electronic State. *The Journal of Chemical Physics*, 80:4403–4409, 1984.
- [49] A. P. Alivisatos. Semiconductor Clusters, Nanocrystals, and Quantum Dots. *Science*, 271:933–937, 1996.
- [50] X. Peng, L. Manna, W. Yang, J. Wickham, E. Scher, A. Kadavanich, and A. P. Alivisatos. Shape Control of CdSe Nanocrystals. *Nature*, 404:59–61, 2000.
- [51] L. Manna, E. Scher, and A. P. Alivisatos. Synthesis of Soluble and Processable Rod-, Arrow-, Teardrop-, and Tetrapod-Shaped CdSe Nanocrystals. *J. Am. Chem. Soc.*, 122:12700–12706, 2000.
- [52] W. U. Huynh, J. J. Dittmer, and A. P. Alivisatos. Hybrid Nanorod-Polymer Solar Cells. *Science*, 295:2425–2427, 2002.
- [53] L. Manna, D. J. Milliron, A. Meisel, E. C. Scher, and A. P. Alivisatos. Controlled Growth of Tetrapod-Branched Inorganic Nanocrystals. *Nature Materials*, 2:382–385, 2003.
- [54] I. Gur, N. A. Fromer, M. L. Geier, and A. P. Alivisatos. Air-Stable All-Inorganic Nanocrystal Solar Cells Processed from Solution. *Science*, 310:462–465, 2005.

- [55] A. K. Rath, M. Bernechea, L. Martinez, F. P. Garcia de Arquer, J. Osmond, and G. Konstantatos. Solution-Processed Inorganic Bulk Nano-Heterojunctions and Their Application to Solar Cells. *Nature Photonics*, 6:529–534, 2012.
- [56] D. B. Mitzi, L. L. Koshbar, C. E. Murray, M. Copel, and A. Afzali. High-Mobility Ultrathin Semiconducting Films Prepared by Spin Coating. *Nature*, 428:299–303, 2004.
- [57] D. B. Mitzi, M. Copel, and C. E. Murray. High-Mobility p-Type Transistor Based on a Spin-Coated Metal Telluride Semiconductor. *Adv. Mater.*, 18:2448–2452, 2006.
- [58] D. J. Milliron, D. B. Mitzi, M. Copel, and C. E. Murray. High-Mobility p-Type Transistor Based on a Spin-Coated Metal Telluride Semiconductor. *Chem. Mater.*, 18:587–590, 2006.
- [59] D. B. Mitzi, M. Yuan, W. Liu, A. J. Kellock, S. J. Chey, V. Deline, and A. G. Schrott. A High-Efficiency Solution-Deposited Thin-Film Photovoltaic Device. *Adv. Mater.*, 20:3657–3662, 2008.
- [60] T. K. Todorov, O. Gunawan, T. Gokmen, and D. B. Mitzi. Solution-Processed Cu(In,Ga)(S,Se)2 Absorber Yielding a 15.2% Efficient Solar Cell. *Prog. Photovolt: Res. Appl.*, 21:82–87, 2013.
- [61] Z. A. Peng and X. Peng. Formation of High-Quality CdTe, CdSe, and CdS Nanocrystals using CdO as a Precursor. *Journal of the American Chemical Society*, 123:183–184, 2001.
- [62] H. C. Leventis, S. P. King, A. Sudlow, M. S. Hill, K. C. Holley, and S. A. Haque. Nanostuctured Hybrid Polymer-Inorganic Solar Cell Active Layers Formed by Controllable In Situ Growth of Semiconducting Sulfide Networks. *Nano Letters*, 10:1253–1258, 2010.
- [63] P. S. Nair, T. Radhakrishnan, N. Revaprasadu, G. Kolawole, and P. O'brien. Cadmium Ethylxanthate: A novel Single-Source Precursor for the Preparation of CdS Nanoparticles. *Journal of Materials Chemistry*, 12:2722–2725, 2002.
- [64] N. Pradhan and S. Efrima. Single-Precursor, One-Pot Versatile Synthesis under Near Ambient Conditions of Tunable, Single and Dual Band Fluorescing Metal Sulfide Nanoparticles. *Journal of the American Chemical Society*, 125:2050–2051, 2003.
- [65] N. Pradhan, B. Katz, and S. Efrima. Synthesis of High-Quality Metal Sulfide Nanoparticles from Alkyl Xanthate Single Precursors in Alkylamine Solvents. *The Journal of Physical Chemistry B*, 107:13843–13854, 2003.
- [66] P. A. van Hal, M. M. Wienk, J. M. Kroon, W. J. H. Verhees, L. H. Slooff, W. J. H. van Gennip, P. Jonkheijm, and R. A. J. Janssen. Photoinduced Electron Transfer and Photovoltaic Response of a MDMO-PPV:TiO<sub>2</sub> Bulk-Heterojunction. *Advanced Materials*, 15:118–121, 2003.

- [67] W. J. E. Beek, M. M. Wienk, and R. A. J. Janssen. Efficient Hybrid Solar Cells from Zinc Oxide Nanoparticles and a Conjugated Polymer. *Advanced Materials*, 16:1009–1013, 2004.
- [68] Y. Zhou, M. Eck, and M. Kruger. Bulk-Heterojunction Hybrid Solar Cells bases on Colloidal Nanocrystals and Conjugated Polymers. *Energy and Environmental Science*, 3:1851–1864, 2010.
- [69] S. Efrima and N. Pradhan. Xanthates and Related Compounds as Versatile Agents in Colloid Science. *Comptes Rendus Chimie*, 6:1035–1045, 2003.
- [70] S. Dowland, T. Lutz, A. Ward, S. P. King, A. Sudlow, M. S. Hill, K. C. Molloy, and S. A. Haque. Direct Growth of Metal Sulfide Nanoparticle Networks in Solid-State Polymer Films for Hybrid Inorganic-Organic Solar Cells. *Advanced Materials*, 23:2739–2744, 2011.
- [71] L. X. Reynolds, T. Lutz, S. Dowland, A. MacLachlan, S. King, and S. A. Haque. Charge Photogeneration in Hybrid Solar Cells: A Comparison Between Quantum Dots and in situ grown CdS. *Nanoscale*, 4:1561–1564, 2012.
- [72] N. Bansal, F. T. F. O’Mahony, T. Lutz, and S. A. Haque. Solution Processed Polymer-Inorganic Semiconductor Solar Cells Employing Sb<sub>2</sub>S<sub>3</sub> as a Light Harvesting and Electron Transporting Material. *Advanced Energy Materials*, 3:986–990, 2013.
- [73] N. Bansal, L. X. Reynolds, A. MacLachlan, T. Lutz, R. S. Ashraf, W. Zhang, C. B. Nielsen, I. McCulloch, D. G. Rebois, T. Kirchartz, M. S. Hill, K. C. Molloy, J. Nelson, and S. A. Haque. Influence of Crystallinity and Energetics on Charge Separation in Polymer-Inorganic Nanocomposite Films for Solar Cells. *Scientific Reports*, 3:1531(8), 2013.
- [74] N. Tigau. Structural Characterization and Optical Properties of Annealed Sb<sub>2</sub>S<sub>3</sub> Thin Films. *Rom. Journ. Phys.*, 53:209–215, 2006.
- [75] S. Ibuki and S. Yoshimatsu. Photoconductivity of Stibnite (Sb<sub>2</sub>S<sub>3</sub>). *Journal of the Physical Society of Japan*, 10:549–554, 1955.
- [76] R. H. Bube. Photoelectronic Analysis of High Resistivity Crystals: (a) GaAs, (b) Sb<sub>2</sub>S<sub>3</sub>. *Journal of Applied Physics*, 31:315–322, 1960.
- [77] E. Cardenas, A. Arato, E. Perez-Tijerina, T. K. Das Roy, G. A. Castillo, and B. Krishnan. Carbon-Doped Sb<sub>2</sub>S<sub>3</sub> Thin Films: Structural, Optical and Electrical Properties. *Solar Energy Materials and Solar Cells*, 93:33–36, 2009.
- [78] C. Kittel. *Introduction to Solid State Physics*. Wiley, 8th edition, 2005.
- [79] H. Ibach and H. Lüth. *Solid-State Physics*. Springer, 4th edition, 2009.

- [80] Felix Bloch. Quantum Mechanics of Electrons in Crystal Lattices. *Z. Phys.*, 52:555–600, 1928.
- [81] C. R. Crowell. The Richardson constant for Thermionic Emission in Schottky Barrer Diodes. *Solid-State Electronics*, 8:395–399, 1965.
- [82] N. F. Mott and R. S. Allgater. Localized States in Disordered Lattices. *Phys. Stat. Sol.*, 21:343–356, 1967.
- [83] M. H. Cohen, H. Fritzsche, and S. R. Ovshinsky. Simple Band Model for Amorphous Semiconducting Alloys. *Physicsl Review Letters*, 20:1065–1068, 1969.
- [84] N. Mott. The Mobility Edge since 1967. *J. Phys. C: Solid State Phys.*, 20:3075–3102, 1987.
- [85] D. Monroe. Hopping in Exponential Band Tails. *Physicsl Review Letters*, 54:146–149, 1985.
- [86] W. Shockley and W. T. Read Jr. Statistics of the Recombination of Holes and Electrons. *Physicsl Review*, 87:835–842, 1952.
- [87] R. N. Hall. Electron-Hole Recombination in Germanium. *Physicsl Review*, 87:387–387, 1952.
- [88] M. J. Powell and S. C. Deane. Improved Defect-Pool Model for Charged Defects in Amorphous Silicon. *Physicsl Review B*, 48:10815–10827, 1993.
- [89] N. F. Mott and R. W. Gurney. *Electronic Processes in Ionic Crystals*. Oxford University Press: New York, NY, 1'st edition, 1940.
- [90] M. A. Lampert and P. Mark. *Current Injection in Solids*. Academic Press, 1st edition, 1970.
- [91] C. D. Child. Discharge from Hot CaO. *Physical Review*, 32:492–511, 1911.
- [92] W. Shockley and R. C. Prim. Space-Charge-Limited Emission in Semiconductors. *Physical Review*, 90:753–758, 1953.
- [93] G. C. Dacey. Space-Charge Limited Hole Current in Germanium. *Physical Review*, 90:759–764, 1953.
- [94] R. W. Smith and A. Rose. Space-Charge-Limited Currents in Single Crystals of Cadmium Sulfide. *Physical Review*, 97:1531–1537, 1955.
- [95] R. W. Smith. Properties of Ohmic Contacts to Cadmium Sulfide Single Crystals. *Physical Review*, 97:1525–1530, 1955.
- [96] A. Rose. Space-Charge-Limited Currents in Solids. *Physical Review*, 97:1538–1544, 1955.

- [97] M. Lampert. Simplified Theory of Space-Charge-Limited Currents in an Insulator with Traps. *Physical Review*, 103:1648–1656, 1956.
- [98] F. Urbach. The Long-Wavelength Edge of Photographic Sensitivity of the Electronic Absorption of Solids. *Physical Review*, 92:1324–1324, 1953.
- [99] P. Mark and W. Helfrich. Space-Charge-Limited Currents in Organic Crystals. *Journal of Applied Physics*, 33:205–215, 1962.
- [100] J. Frenkel. On Pre-Breakdown Phenomena in Insulators and Electronic Semi-Conductors. *Physical Review*, 54:647–648, 1938.
- [101] P. Murgatroyd. Theory of Space-Charge-Limited Current Enhanced by Frenkel Effect. *J. Phys. D: Appl. Phys.*, 3:151–156, 1970.
- [102] C. Waldauf, M. Morana, P. Denk, P. Schilinsky, K. Coakley, S. A. Choulis, and C. J. Brabec. Highly Efficient Inverted Organic Photovoltaics using Solution Based Titanium Oxide as Electron Selective Contact. *Applied Physics Letters*, 89:233517(3), 2006.
- [103] K. J. Reynolds, J. A. Barker, N. C. Greenham, R. H. Friend, and G. L. Frey. Inorganic Solution-Processed Hole-Injecting and Electron-Blocking Layers in Polymer Light-Emitting Diodes. *Journal of Applied Physics*, 92:7556–7563, 2002.
- [104] C.-W. Chu, S.-H. Li, C.-W. Chen, V. Shrotriya, and Y. Yang. High-Performance Organic Thin-Film Transistors with Metal Oxide/Metal Bilayer Electrode. *Applied Physics Letters*, 87:193508(3), 2005.
- [105] M. Kröger, S. Hamwi, J. Meyer, T. Riedl, W. Kowalsky, and A. Kahn. Role of the Deep-Lying Electronic States of MoO<sub>3</sub> in the Enhancement of Hole-injection in Organic Thin Films. *Applied Physics Letters*, 95:123301(3), 2009.
- [106] T. Matsushima, Y. Kinoshita, and H. Murata. Formation of Ohmic Hole Injection by Inserting an Ultrathin Layer of Molybdenum Trioxide between Indium Tin Oxide and Organic Hole-Transporting Layers. *Applied Physics Letters*, 91:253501(3), 2007.
- [107] K. S. Yook and J. Y. Lee. Low Driving Voltage in Organic Light-Emitting Diodes using MoO<sub>3</sub> as an Interlayer in Hole Transport Layer. *Synthetic Metals*, 159:69–71, 2009.
- [108] M. von Ardenne. Die Grenzen fur das Auflösungsvermögen des Elektronenmikroskops. *Zeitschrift für Physik*, 108:338–352, 1938.
- [109] M. von Ardenne. Das Elektronen-Rastermikroskop. *Zeitschrift für Physik*, 109:553–572, 1938.
- [110] D. McMullan. Scanning Electron Microscopy 1928-1965. *Scanning*, 17:175–185, 1995.
- [111] M. Zeman. Optical and Electrical Modeling of Thin-Film Silicon Solar Cells. *J. Mater. Res.*, 23:529–534, 2008.

- [112] M. Kryszewski and A. Szymanski. Space Charge Limited Currents in Polymers. *Journal of Polymer Science: Macromolecular Reviews*, 4:245–320, 1970.
- [113] T. Kirchartz. Influence of Diffusion on Space-Charge-Limited Current Measurements in Organic Semiconductors. *Beilstein Journal of Nanotechnology*, 4:180–188, 2013.
- [114] MSc thesis: On Diffusion-Barriers in Space-Charge-Limited Current Measurements of Polymer Single-Carrier-Devices. [http://www.nbi.ku.dk/english/Calendar/activities\\_13/jason\\_rohr\\_masterthesis/](http://www.nbi.ku.dk/english/Calendar/activities_13/jason_rohr_masterthesis/).
- [115] J. Fischer, W. Trees, H. Kleeman, J. Widmer, K. Leo, and M. Riede. Exploiting Diffusion Currents at Ohmic Contacts for Trap Characterization in Organic Semiconductors. *Organic Electronics*, 15:2428–2432, 2014.
- [116] M. C. Scharber, D. Mühlbacher, M. Koppe, P. Denk, C. Waldauf, A. J. Heeger, and C. J. Brabec. Design Rules for Donors in Bulk-Heterojunction Solar Cells - Towards 10% Energy-Conversion Efficiency. *Advanced Materials*, 18:789–794, 2006.